FUEL CELLS AND REVERSE FUEL CELLS:

NANOSTRUCTURED PATTERNED ELECTRODES AND MEMBRANES

A Dissertation

by

YIFEI YANG

Submitted to the Graduate and Professional School of
Texas A&M University
in partial fulfillment of the requirements for the degree of

DOCTOR OF PHILOSOPHY

Chair of Committee,	Yossef A. Elabd
Committee Members,	Jodie L. Lutkenhaus
	Micah. J. Green
	Emily Pentzer
Head of Department,	Arul Jayaraman

May 2022

Major Subject: Chemical Engineering

ABSTRACT

Proton exchange membrane (PEM) fuel cells and PEM reverse fuel cell dehumidifiers (or PEM electrolytic dehumidifiers) are zero emission, high efficiency electrochemical energy devices. However, the high cost associated with their material components, *e.g.*, platinum (Pt) electrocatalysts, perfluorinated PEMs, hinders wide scale commercialization. In this work, fundamental mechanisms and strategies were explored in ultra-low Pt PEM fuel cells and low-cost PEM electrolytic dehumidifiers. For ultra-low Pt PEM fuel cells, a series of organized hexagonally patterned electrodes (diameters of 40, 80, 160, and 360 µm) were fabricated *via* template-assisted electrospinning/electrospraying (E/E), and the 80 µm pattern resulted in 42% Pt utilization enhancement compared to its random analog (without template-assisted). For low-cost PEM electrolytic dehumidifiers, *i.e.*, to reduce the cost of conventional perfluorinated Nafion membrane, a series of commercial sulfonated pentablock terpolymer membranes (*i.e.*, NEXAR® with ion exchange capacities (IECs) of 1.0 and 2.6 meq g^{-1}) were evaluated in a PEM electrolytic dehumidifier. Water vapor transmission rates (WVTRs) and energy efficiency were measured at various humidity gradients and potential directions for membrane electrode assemblies (MEAs). NEXAR® (at 1.0 meq g^{-1} IEC) showed the highest energy efficiency, serving as a cost-effective alternative to Nafion. Additionally, a fundamental investigation in electrospun sulfonated pentablock terpolymers and poly(ionic liquid)s was explored for future application to advanced low-cost electrodes in electrochemical energy devices. Overall, this work demonstrates nanoscale engineering of polymer electrolytes as electrodes and membranes in both PEM fuel cells and PEM reverse fuel cells that results in lower cost for high performance zero emission electrochemical energy devices.

DEDICATION

It’s never too late to be whoever you want to be. I hope you live a life you’re proud of, and if you find that you’re not, I hope you have the strength to start over.

— F. Scott Fitzgerald

ACKNOWLEDGMENTS

First and foremost, I would like to thank my dear advisor, Professor Yossef A. Elabd, who believes in me more than I do, for your profound expertise, patient guidance, constant optimism, and endless encouragement throughout my research journey. I also thank the members of my dissertation committee, Dr. Jodie L. Lutkenhaus, Dr. Micha J. Green, Dr. Mohammad Naraghi, and Dr. Emily Pentzer, for their time to review my work and provide suggestions throughout the course of this study. I would also like to thank all of the past and present members of the Elabd research group (Dr. Tzu-Ling Chen, Mahesh Agrawal, Dohyun Kim, Arthur Kleiderer), specifically Dr. Monica Hwang and Dr. Rui Sun for their extensive training and mentoring on the MEA fabrication, polymer synthesis, and dissertation writing. Thank Dr. Patrick M. Lathrop and Kevin Nixon for the sunshine-like optimism they spread in research and everyday life.

I would also like to thank Dr. Vijay Mhetar and Roger Tocchetto for offering me the summer internship in Kraton Polymers (Houston), so that I could enjoy the weekly chemistry class offered by Dr. Carl Willis, and inspiring discussions on block copolymers with Dr. Richard Blackwell (B.J.), Dr. John Flood and Dr. Jiaqi Yan.

I appreciate Texas A&M University for providing numerous research supports. I would like to thank Heidi Clarke, Ethan Morse, and Mr. Larry A Rehn for training me in photolithography in Aggiefab nanofabrication facility. Thanks to Mr. Tom Stephens for training me on the SEM, and Mr. Rick Littleton for training me on the TEM microtome in Miscopy Imaging Center (MIC). Thanks Dr. Yordanos Bisrat for her help in cross-sectional SEM, and Dr. Sisi Xiang for her great instructions on Focus-ion-beam (FIB) training and TEM imaging from Material Characterization Facility (MCF). Thanks Dr. David Truong for his help with small-angle X-ray scattering (SAXS) experiments from soft matter facility. Thank Matthew Crawford from Fuel Cell Store for invaluable information on the electrolysis MEA fabrication.

Lots and Lots of thanks also go to my dear non-blood sisters, Wen Zhu and Qiong Su for their meticulous care and selfless support, to my American parents Karen and Richard Davison for their amazing kindness, to my reading buddy Hallie Horn and Shelby Pattillo, they have made my life in College Station incomparable. Thank Guanyang Liu for the precious insights into my work and life. Thanks Mr. Doug White, Dr. Patricia Goodson, Dr. Licia He, Dr. Ergun Akleman, and Dr. Weizhong Qian who supported me to pursue my dream. A cute thanks to my lovely cat Ginger for his silent companionship. Finally, thanks to my mother Chunhong Bi and my father Liang Yang for the love, freedom and faith they gave me. Very deep gratitude for Professor Zijiang Zhao, who armored me with love and courage to explore the wilderness fearlessly.

CONTRIBUTORS AND FUNDING SOURCES

Contributors

This work was supervised by a thesis (or) dissertation committee consisting of Professor Yossef A. Elabd, Professor Micha J. Green, and Professor Jodie L. Lutkenhaus of the Department of Chemical Engineering and Professor Emily Pentzer of the Department of chemistry.

The electrospinning apparatus in Chapter 2, 4, and 5 was developed by Monica Hwang (Elabd Research Group). The NEXAR® polymers for Chapter 3 and Chapter 4 were provided by Kraton Corporation.

All other work conducted for the dissertation was completed by the author/student (Y.Y.) independently.

Funding Sources

This work was also made possible in part by the National Science Foundation under Grant Number CMMI-1661822 and Kraton Corporation. Its contents are solely the responsibility of the authors and do not necessarily represent the official views of the National Science Foundation.

NOMENCLATURE

^{1}H NMR	Proton Nuclear Magnetic Resonance
BEV	Battery Electric Vehicle
BF_4	Tetrafluoroborate
BIm	Butylimidazolium
CL	Catalyst Layer
CV	Cyclic Voltammetry
DLS	Dynamic Light Scattering
DSC	Differential scanning calorimetry
E/E	Electrospinning/Electrospraying
EIS	Electrochemical Impedance Spectroscopy
FCV	Fuel Cell Vehicle
GDL	Gas Diffusion Layer
HER	Hydrogen Evolution Reaction
HOR	Hydrogen Oxidation Reaction
ICEV	Internal Combustion Engine Vehicle
IEC	Ion Exchange Capacities
Ir	Iridium
Li	Lithium
Li^+	Lithium-ion
MEA	Membrane Electrode Assembly

OER	Oxygen Evolution Reaction
ORR	Oxygen Reduction Reaction
PEM	Proton Exchange Membrane
PEMFC	Proton exchange membrane fuel cells
PIL	Poly (ionic liquid)
Pt	Platinum
SAXS	Small Angle X-ray Scattering
SEM	Scanning Electron Microscopy
SPE	Solid-state Polymer Electrolyte
T_d	Degradation Temperature
T_g	Glass Transition Temperature
TGA	Thermal Gravimetric Analysis
Ti	Titanium
TPB	Triple Phase Boundary
VBC	Vinylbenzyl Chloride
WVTR	Water Vapor Transmission Rate

TABLE OF CONTENTS

Page

LIST OF FIGURES

Page

LIST OF TABLES

Page

CHAPTER 1.

INTRODUCTION

1.1. Overview

The excessive global greenhouse gas (GHG, 36.4 Gt CO_{2eq}) emission from transportation and building services (*i.e.*, 28% and 20% of total energy consumption in the USA in 2020,[1-3] respectively) is a growing concern and requires zero GHG emission energy conversion devices to displace current technology. In the transportation sector, battery electric vehicles (BEVs) have drastically increased from 2015 to 2021 (from 1.1 to 6.4 million units), replacing traditional internal combustion engine vehicles (ICEVs). However, shortcomings remain for BEVs, including limited driving ranges (*ca.* 500 km[4]) and slow charging rates (*ca.* 6–8 h for fully charging). Fuel cell electric vehicles (FCEVs) provide an alternative zero GHG emission to BEVs for select applications, such as heavy-duty vehicles (*e.g.*, buses and semi-trucks) due to the high gravimetric energy density of hydrogen (33.6 kWh/kg_{H2} *vs.* 12–14 kWh/kg_{diesel}), long driving ranges (*ca.* 1000 km[5]) and the fast refueling (*ca.* 3–5 min).[6, 7] Among the multiple types of fuel cells, proton exchange membrane fuel cells (PEMFCs) are promising candidates for the automobile industry, as well as, additional applications in portable and stationary energy due to its distinguishing features of low operating temperature (50–100 °C), lightweight, and high power density.

In regards to building services, operating PEMFCs in reverse as an electrolytic dehumidifier can effectively mitigate the primary energy consumption (*ca.* 1000 kWh per dehumidifier unit, 9% of the average household energy consumption[8]) in space cooling of buildings and indoor humidity control and displace conventional air-conditioning (AC) systems utilizing condensation refrigerants.[9] Dehumidification in conventional AC has the disadvantages of intensive energy consumption (25% of the total energy consumption per AC[10]), insufficient dehumidification capacity, and wet surfaces corrosion. Chemical dehumidification by liquid or solid desiccants is typically space-demanding and suffers from high energy costs due to desiccants regeneration at high temperatures (170–200°C). In contrast, a reverse fuel cell dehumidifier is space-flexible and environmentally friendly. It can statically operate at low potentials (*ca.* 3–20 V) at room temperature or coupled with evaporative cooling to achieve energy-efficient AC. The following sections provide a review of PEMFCs and proton exchange membrane (PEM) electrolytic dehumidifiers, along with the recent advances in their materials, specifically their electrodes and membranes. The overall goal is to address the cost issue of precious metal catalysts and fluorinated membranes and ultimately achieve cost-effective, commercially available PEMFCs and PEM-based electrolytic dehumidifiers to reduce global energy consumption and GHG emissions.

1.2. Proton Exchange Membrane Fuel Cell (PEMFC)

The first fuel cell was invented in 1839 by Sir William Robert Grove, and the first actual application was in the Gemini space mission in 1962 by General Electric.[11] In the early 1970s, Dupont invented a perfluorinated sulfonic acid membrane with the tradename Nafion®, which had a significant impact on fuel cell development as it became the benchmark PEM in PEMFCs. In the 1990s, several breakthrough findings from the Los

Alamos National Laboratory resulted in significant reductions in platinum catalyst loading in a PEMFC, while still maintaining high power density.[12] These advancements resulted in significant academic and industrial research and development in PEMFCs since this time. Reducing cost and improving the PEMFC durability is still a primary focus of research development today.

A typical PEMFC, as shown in Figure 1.1, consists of five major symmetric components (assembled between two gas flow channels): a PEM in the middle, two electrodes, and two gas diffusion layers (GDLs). A PEMFC converts chemical energy stored in fuels (*i.e.,* converting hydrogen and oxygen directly into electrical energy with zero carbon dioxide emission with water as the sole byproduct).[13] At the anode side, hydrogen fuels are catalytically spilt into protons and electrons, *i.e.,* hydrogen oxidation reaction (HOR), as shown in Equation 1.1. The newly formed protons are transported through the PEM to the cathode side. The electrons travel externally through the load circuit and create the current output. Meanwhile, oxygen fuel supplied at the cathode reacts with the transported protons, completing the other half-cell reaction, *i.e.,* oxygen reduction reaction (ORR), as shown in Equation 1.2.

Anode (HOR): $2H_2 \rightarrow 4H^+ + 4e^-$ Equation 1.1

Cathode (ORR): $O_2 + 4H^+ + 4e^- \rightarrow 2H_2O$ Equation 1.2

Overall: $2H_2 + O_2 \rightarrow 2H_2O$ Equation 1.3

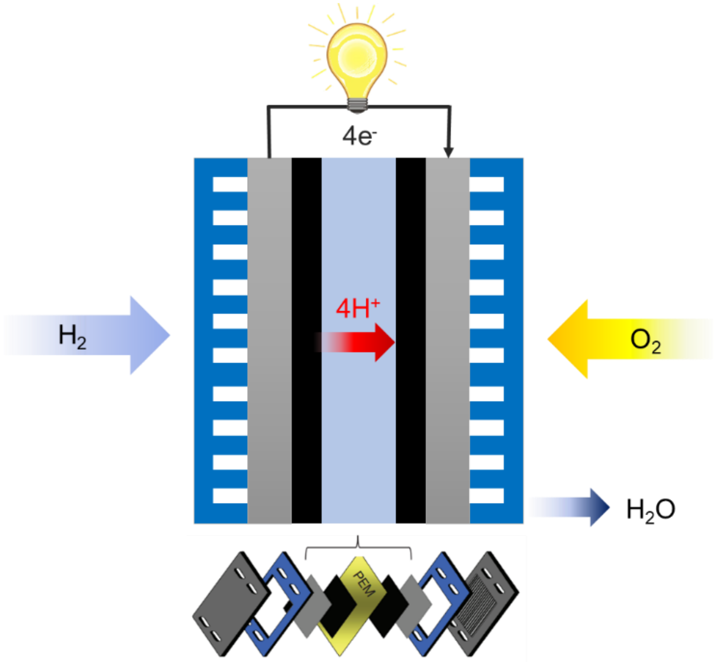

Figure 1.1 Schematic of a proton exchange membrane fuel cell (PEMFC).

1.2.1. Electrode Structure

The conventional electrode structure is a porous network composed of agglomerated catalyst particles (agglomerates of platinum (Pt) catalyst nanoparticles (*ca.* 2 nm) supported on carbon nanoparticles (*ca.* 25–50 nm) impregnated with proton-conducting ionomer, illustrated in Figure 1.2. The carbon-supported Pt catalyst allows electrons to transport through the catalyst layer, the proton conductive ionomer surrounding the catalyst acts as the bridge for the protons to move through the catalyst layer and reach the Pt sites. The porosity allows oxygen to diffuse through the catalyst layer to reach these Pt sites, *i.e.*, triple phase boundaries (TPBs), where all indispensable reaction species (electron, proton, and oxygen) intersect and ORR occurs.[12, 14-16]Although PEMFCs are now commercially available, the high loadings of expensive Pt catalyst (a crucial component required to achieve high power densities) have hindered extensive market applications.[17, 18] Specifically, high cathode Pt loading (typically 0.4–0.5 mg_{Pt} cm^{-2}) is required to overcome the inherent sluggish ORR kinetics on the cathode.[19] Therefore, reducing the Pt loading without sacrificing fuel cell performance (*i.e.*, Pt utilization enhancement) has attracted considerable interest for many decades.

To enhance Pt utilization through optimizing TPBs, particularly under ultra-low Pt loading conditions, a balance between void and solid volume in the electrode requires careful design. Conventional electrode fabrication techniques typically include depositing (*e.g.*, paint-brushing or air-spraying) a well-dispersed catalyst ink solution (mixture of Pt/C catalyst, Nafion ionomer, and water/alcohol solvents) onto a gas diffusion layer, which usually results in an evaporation-formed random porous network. The internal structure of the porous network typically can be adjusted by catalyst ink preparation (*e.g.*, Nafion to Pt/C ratio,[20-22] hydrophobic additives,[23-25] ink dispersing media,[26-28] and dispersion technique[29, 30]). Since conventional ink-based electrode fabrication provides minimum subject control over the internal architecture, the design and fabrication of a well-defined electrode construction are of great interest to achieve adjustable TPBs with competitive cost as an alternative to maximize Pt utilization.

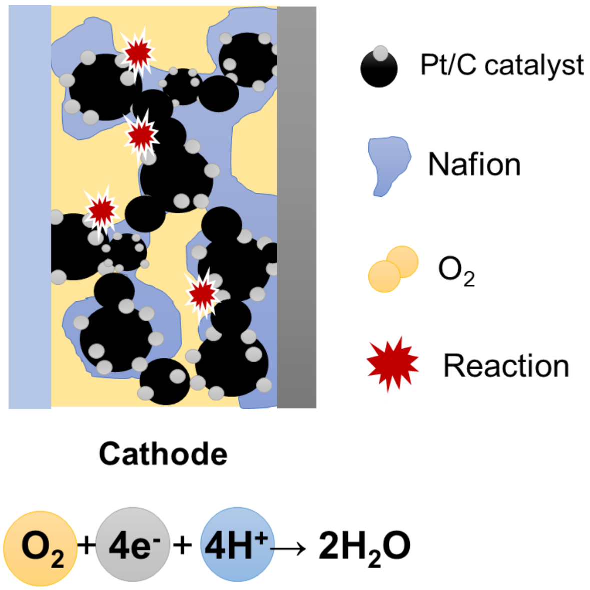

Figure 1.2 Illustration of triple phase boundaries (TPBs; red icon) existing at the Pt/C catalyst, Nafion ionomer, and oxygen interface.

1.2.2. Electrode Patterning Approach

Increasing attention has been focused on artificially designed electrode interface or internal structures in addition to conventional design and optimization of catalyst ink.[31, 32] As an emerging approach for advanced electrode design, tailoring microstructure through patterning can rearrange the proton-electron-porosity percolating networks, and enable enhanced fuel cell performance.[31, 33] Constructing patterned electrodes with periodic structures to optimize TPBs has been investigated with both two-dimensional (2D) and three-dimensional (3D) patterns, as shown in Figure 1.3. 2D geometrically patterned electrodes are usually catalyst ink-based and fabricated by inkjet printing [34-37] or by spraying the ink through flat micro-stencil masks.[38-40] In contrast, 3D patterned electrodes consist of larger z-direction depth, which could provide more void space and interconnected macropores, resulting in enhanced TPB connections compared to their 2D counterparts. Common approaches to extend 2D to 3D patterned electrodes include imprinting commercial Nafion membranes with patterned molds[41-43] or lithography etching,[44] employing liquid precursors to build patterned membranes by micromolding techniques,[42, 45-48] and casting catalyst ink slurries into elastomeric molds.[49] Although feasible, patterned interfaces prepared by these methods are less durable due to the collapse of the Nafion surface in the subsequent hot-pressing bonding procedure for membrane electrode assemblies (MEAs; anode/PEM/cathode layered composite) at the glass transition temperature of Nafion (T_g) (*ca.* 135 °C). More durable intricate alternative 3D patterning methods usually require a sacrificial template, which either Pt or Nafion ionomer will be deposited on to form a 3D framework. After removing the initial sacrificial template, the other species will be deposited on the outer surface of the framework from the previous step. For instance, an inverse oval patterned Pt electrode was constructed through self-assembled polystyrene beads, showing enhanced mass transfer and performance owing to the morphological advantages.[50] Patterned Nafion arrays constructed *via* anodic aluminum oxide (AAO) templates also demonstrated power density and lifetime improvements.[51] Even though these methods hold promise in improving power performance, the cathode Pt loading remains relatively high (0.2–0.4 mg_{Pt} cm^{-2}), higher than the 2020 DOE total Pt loading target (0.125 mg_{Pt} cm^{-2}).[52] Therefore, a simple and scalable 3D patterned electrode fabrication technology with ultra-low Pt loading is still highly desirable.

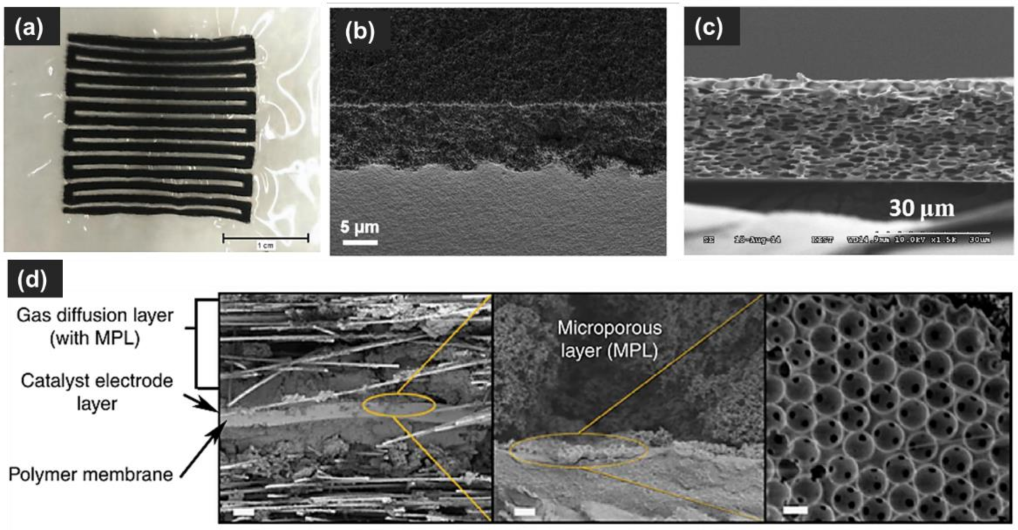

Figure 1.3 Patterned electrodes adapted from references. (a) An inkjet-printed serpentine catalyst layer on Nafion membrane,[36] (b) cross-section of deposited catalyst layer on the patterned Nafion membrane,[43] (c) cross-section of a porous Nafion membrane,[53] and (d) porous Pt electrodes fabricated through an inverse-opal structure.[50]

1.3. Proton Exchange Membrane Electrolytic Dehumidifier

Proton exchange membrane (PEM) electrolytic dehumidifiers possess the advantages of compact system design, low operating temperature and voltage, and high dehumidification capacities. Compared to the conventional bulky liquid/solid desiccant absorption/adsorption equipment and energy-intensive vacuum-based dehumidification techniques, a PEM electrolytic dehumidifier could directly drive the moisture from one side to another under low electric fields without cooling agents or adsorbents, serving as a perfect candidate for addressing problems caused by high humidity in a limited enclosed space, such as corrosion or degradation issue in electronics, precision manufacturing, medication or artwork preservation industry.[54-56]

The working principles for a PEM electrolytic dehumidifier are reverse of a PEMFC, therefore it could also be considered as a reverse fuel cell. As illustrated in Figure 1.4, a PEM dehumidifier consists of a multi-layer sandwiched structure similar to a PEMFC, *i.e.*, a PEM as the solid electrolyte in the middle and two supported catalyst layers on each side as the anode and cathode. Different from a PEMFC utilizing carbon-based gas diffusion layers on both anode and cathode, the anode of a PEM dehumidifier requires anti-corrosive material (*e.g.*, Ti mesh or foam) to mitigate carbon support corrosion.[57]

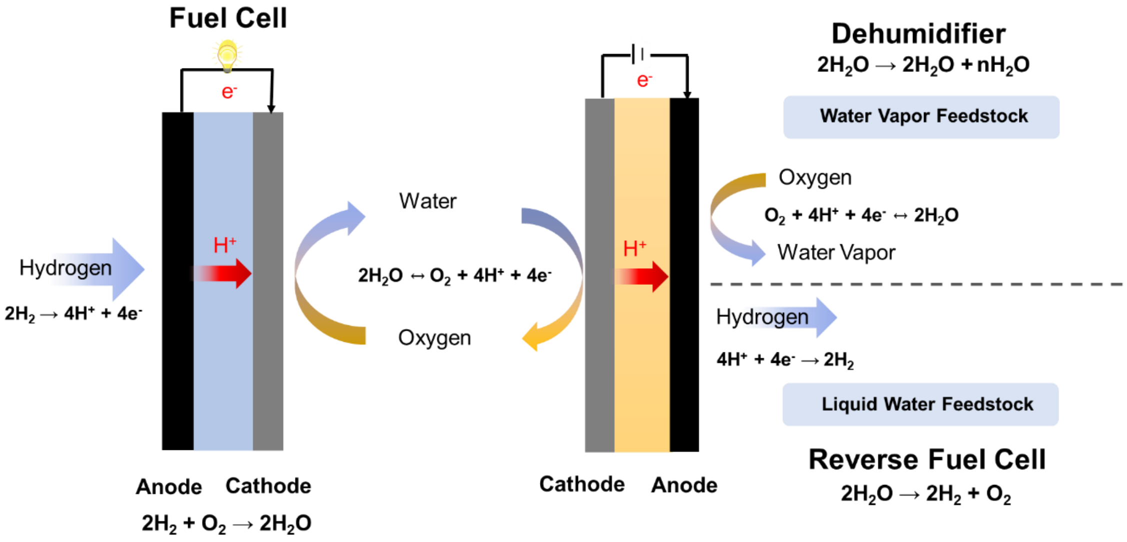

Figure 1.4 Principle and structure comparison between a PEM electrolytic dehumidifier (reverse fuel cell) and a PEMFC.

When an external potential is applied, the oxygen evolution reaction (OER, *i.e.*, Equation 1.4) occurs at the anode resulting from water vapor decomposition in the air. On the cathode, both ORR (*i.e.*, Equation 1.5) and hydrogen evolution reaction (HER, *i.e.*, Equation 1.6) are eligible to occur depending on the status of catalysts, reactants, and electric field intensity. Therefore, the overall reaction could be either net water transportation from anode to cathode (Equation 1.7) or a combination of water electrolysis (Equation 1.8). In a traditional water electrolyzer[58] with either liquid or water vapor (with inert carrier gas) as the feedstock, no oxygen is delivered on the cathode to prevent cell efficiency deterioration. However, during dehumidification with humid air feedstock, thermodynamically favored ORR (-1.23 V *vs.* SHE)[59] is unavoidable and competes with HER (0 V *vs.* SHE) for proton consumption. At the same time, the water generation also complicated water management and could result in back diffusion, which will decrease the cell efficiency.

Anode (OER): $2H_2O \rightarrow 4e^- + 4H^+ + O_2$ Equation 1.4

Cathode (1, ORR): $O_2 + 4H^+ + 4e^- \rightarrow 2H_2O$ Equation 1.5

Cathode (2, HER): $2H^+ + 2e^- \rightarrow 2H_2$ Equation 1.6

Overall (1): $2H_2O \rightarrow 2H_2O$ Equation 1.7

Overall (2): $2H_2O \rightarrow 2H_2 + O_2$ Equation 1.8

As demonstrated in Figure 1.5, the water transport mechanism in the PEM dominated by two primary mechanisms: electro-osmotic diffusion and concentration gradient driven diffusion.[60] With applied external potential, water molecules in the vicinity of the anode decompose into protons and oxygen molecules. The protons are driven toward the cathode by the electric field, together with a certain number of water molecules *via* hydrogen bonding and electro-osmosis drag effect[61] due to the formation of proton and water molecules aggregation species. The protons are then combined with oxygen molecules at the cathode to reproduce water.[9] As a result, the water content at the anode gradually decreases, and the dehumidification occurs.

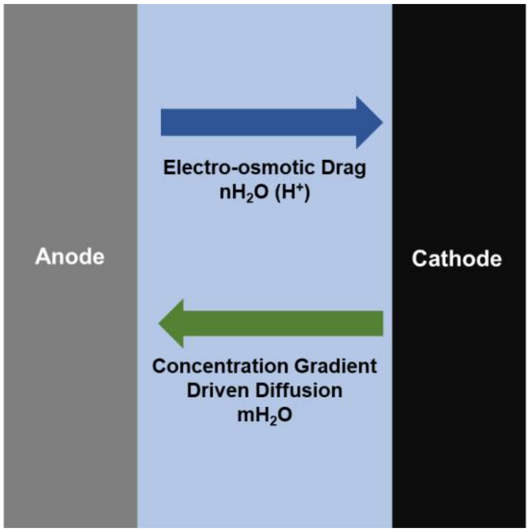

Figure 1.5 Water transport schematic across the PEM in an electrolytic dehumidifier.

The dehumidifying capability (*i.e.*, $\Delta m/\Delta t$, g s^{-1}) can be expressed as the Equation 1.9:[62]

$$\frac{\Delta m}{\Delta t} \cong \frac{9(1+2\alpha)}{eN_A}\langle I\rangle_{[t_1,t_2]} - \frac{DS}{L}\langle \rho_{s,c} - \rho_{s,a}\rangle_{[t_1,t_2]} \qquad \text{Equation 1.9}$$

In Equation 1.9, $\rho_{s,c}$ and $\rho_{s,a}$ are the water densities (g cm^{-3}) at anode and cathode, respectively; D (cm^2 s^{-1}) is the diffusion coefficient of water inside PEM, S (cm^2) and L (cm) are the area and thickness of PEM, α is the electro-osmotic drag coefficient, and I

is the average current density (A cm^{-2}) from operating time t_1 to t_2. As seen from Equation 1.9, the dehumidifying capacities are determined through the water transport difference among electrolytic current, the electro-osmosis drag, and the concentration gradient driven diffusion.

While theoretical water transportation and management inside a PEM reverse fuel cell are relatively well-understood, device-level practices are still limited on water electrolyzers with liquid water as the feedstock and targets of hydrogen generation. In order to promote the performance of air-feed dehumidifiers performance, simulations and systematic experimental investigations are necessary to properly guide both materials (*e.g.,* PEM and electrode) and operational factors (*e.g.,* applied potential, RH, air convection) design, which will be reviewed in the following section.

1.3.1. Numerical and Experimental Research Advances

As a recently proposed technology, PEM-based electrolytic dehumidification with gaseous water vapor feedstock under low temperature has not been extensively explored with only a few studies (< 20 publications) reported to date.

Numerical models have been developed for the prediction of humidity and current evolution with time. Early studies in 2009 by Sakuma *et al.*[62] experimentally validated the electrolytic dehumidification by a commercial Nafion membrane at normal temperatures (20–40 ℃) *via* a two-layer model, which can predict the dynamic membrane characteristics, including water content and dehumidifier electrical resistance. The following work by Sakuma *et al.*[63] in 2010 modified the model with a leakage area to define an attainable steady-state humidity, which is preferable for practical applications. In 2017, Qi *et al.*[64] developed a 2D steady-state model combining mass and heat transfer to simulate the PEM properties (*e.g.,* thickness, water content, conductivity) influence on the dehumidification rate. Based on Qi *et al*.'s work, Zhang *et al*.[65] optimized the anode-side exchange current density and heat transfer coefficient by a multi-parameter fitting method to minimize the simulation error. From the standpoint of material physical characteristics, Li *et al.*[66] applied a 2D steady-state model solved by finite difference method to elucidate the vital role of anode catalyst layer properties (*e.g.,* thickness, porosity, pore diameter, tortuosity).

Experimental research has focused on predicting voltage-current characteristics (V–I curve, *i.e.*, polarization) to understand electrolytic dehumidifier performance. Unlike the PEM water electrolyzer, which typically operates under a relatively lower voltage (*i.e.,* 1.5–2.2 V), PEM electrolytic dehumidifier requires a higher voltage (*i.e.,* > 3V) to achieve satisfactory dehumidification rates. For instance, in 2011, Sakuma *et al.*[67] conducted a four-electrode boundary voltage measurement and proposed an experimental formula to predict the steady-state current as a function of electrode water content and overpotential, reaching 61.2 mA cm^{-2} (30 °C, 80% RH) at above 1.8 V. Li *et al.*[68] explored V–I -characteristics with *in situ* electrochemical impedance spectroscopy (EIS) and achieved 32–43 mA cm^{-2} (19 °C 95% RH) and proposed proton conductivity reduction of PEM as the main reason for current attenuation at high voltages (> 2.5 V). Greenway *et al.*[69] investigated V–I characteristics in an anode-liquid and cathode vapor feed (a mass transport limited condition, which limits the reaction rate) configurations in a PEM based electrolyzer, reaching a limiting current of 400 mA cm^{-2} (70 °C) at above 1.6 V.

Despite these initial studies, PEM electrolytic dehumidification still suffers from multiple problems as an emerging technology,[9] such as high costs of PEM and noble metal catalyst (*e.g.*, IrO_2, Pt), intensive energy consumption, low system durability,[70] and unclear ORR and HER competing mechanisms. Of all the issues mentioned above, identifying alternative low-cost PEMs that can alleviate energy costs and improve dehumidification efficiency is of significant priority towards the commercialization of PEM electrolytic dehumidifiers.

1.3.2. Proton Conducting Membrane in Electrolysis/Dehumidifier

The PEM in membrane electrolysis dehumidification serves as a separator and a transmission pathway for protons and water molecules. In addition to operating conditions for a vapor feed electrolytic dehumidifier, the intrinsic properties of the PEM (*e.g.*, ion exchange capacity, nanostructure, mechanical strength) also play a critical role in determining the dehumidification performance and energy efficiency.[65] In pioneering work in 2009, Iwahara *et al.*[71] proved the concept of a solid-state electrolytic dehumidifier using a proton-conducting ceramic-based solid electrolyte based on previous work[72, 73] on high-temperature steam electrolyzer, and achieved partial water vapor pressure reduction from 45 Pa to 6.7 Pa at 700 °C. In 2008, Sawada *et al.*[74] synthesized a crosslinked polytetrafluoroethylene (PTFE) PEM and performed water vapor electrolysis at 1.4–2.5 V at low-temperature ranges (50–80 °C). Li *et al.*[75] reported on the performance of the PEM electrolytic dehumidifier and that it is determined by the proton conductivity, electro-osmotic drag coefficient, and back diffusion properties of the PEM, which are all related to the water content of the PEM.

It is noteworthy that the hydration state of the PEM differs between fuel cell and reverse fuel cell dehumidifier. During fuel cell operation, the PEM is exposed to fully humidified O_2 and H_2 in a serpentine flow field, whereas during reverse fuel cell dehumidification, the PEM is fed with static air of varying humidity, which poses higher requirements of the water retention properties for the latter.[76] Theoretical investigation by Qi *et al.* [77] indicated that the water content of the PEM was a key factor affecting water removal. With increasing PEM water content, both the conductivity and electro-osmotic drag coefficient increased significantly, thereby improving moisture transfer inside the PEM. Therefore, studies have focused to further optimize water retention and properties of the commonly used benchmark PEM, *i.e.,* Nafion membrane, to reduce its ohmic losses and achieve better performance.[78] For instance, fabrication of a high water uptake PEM with physically or chemically incorporated SiO_2 nanoparticles by Li *et al.*[75] increased dehumidification rate and energy efficiency by 17% and 22%, respectively. Qi *et al.*[64, 79] studied the influencing factors of PEM-based electrolytic dehumidification, including the airflow rate, air temperature, relative humidity, and applied voltages. The steady-state energy efficiency was $1.5 \times 10^{-2} – 2.0 \times 10^{-2}$ g J^{-1} m^{-2}, with 45–55% total mass transfer including back diffusion, leading to low energy efficiency. Examples of PEM in water vapor electrolyzer or electrolytic dehumidifier, including the anode and cathode feedstock condition and water removal rate (for dehumidifier), are listed in Table 1.1.

Table 1.1 Membranes in electrolyzer/electrolytic dehumidifier

Membrane	System	Performance	Ref.
$SrCeO_3$-based ceramic	Electrochemical dehumificaiton	Desiccate test gas with initial P_{H_2O} of 45 Pa to 6.7 Pa	Iwahara et al.[71]
Crosslinked-PTFE	Water vapor electrolysis	50 mA cm^{-2} at 80 °C, 95% RH, 2.5 V	Sawada et al.[74]
Nafion 117	Electrolytic air dehumidification	$1.065–1.294 \times 10^{-4}$ kg s^{-1} at 22 °C, 92% RH, 3 V	Li et al. [66]
Nafion 212	Electrolytic air dehumidification	$0.25–0.45 \times 10^{-4}$ g s^{-1} at 22 °C, 90% RH, 2–4 V	Li et al. [70]
Nafion 212	Electrolytic air dehumidification	0.005–0.016 g s^{-1} at 19 °C, 95% RH, 1.5–3.8 V	Li et al. [68]
NEXAR®	Liquid water electrolysis	1140 mA at 25 °C, 3V	Filice et al.[80]
Nafion 117	Electrolytic air dehumidification	$0.2–1.5 \times 10^{-4}$ g s^{-1} at 22 °C, 70–90% RH, 3 V	Qi et al. [77]
Nafion 117	Electrolytic air dehumidification	$0.2–0.5 \times 10^{-4}$ g s^{-1} at 22 °C, 70–90% RH, 3 V	Qi et al. [81]
Nafion 115	Water vapor electrolysis	20 mA cm^{-2} at 20 °C, 95% RH, 1.7 V	Spurgeon et al.[58]
Nafion 117	Electrolytic air dehumidification	4.1×10^{-4} g s^{-1} at 30 °C, 60% RH, 3 V	Sakuma et al.[67]
Nafion 212-SiO_2	Electrolytic air dehumidification	$0.1–0.9 \times 10^{-4}$ g s^{-1} at 35 °C, 45% RH, 3 V	Li et al.[75]

Despite the advancements of investigation on the operational factors influence on dehumidification performance, Nafion membranes (*i.e.,* similar IECs with multiple thicknesses) remain the leading state-of-the-art PEM. To date, studies on electrolytic dehumidification with alternative hydrocarbon-based membranes are still scarce, specifically with a variation on different hydration levels (*i.e.*, multiple IECs). Future investigations on low-cost hydrocarbon-based PEM with competitive performance and energy efficiency are highly desired to provide insights into the proper design of electrolytic dehumidification membranes.

1.4. Outline and Summary

In this dissertation, commercially available proton-conducting polyelectrolytes were engineered as nanostructured patterned electrodes and membranes, targeting high energy density, energy-efficient, low-cost PEMFCs and revere fuel cell dehumidifiers.

Chapter 2 utilizes the template-assisted electrospinning/electrospraying (E/E) technique as a novel engineering approach to reorganize triple-phase boundaries (TPBs) and enhance Pt utilization in PEMFC electrodes at ultra-low Pt loadings (*ca.* 0.06 $\mathrm{mg_{Pt}}$ $\mathrm{cm^{-2}}$). The impacts of the hexagonal nanofiber-nanoparticle patterned electrodes with four varying sizes on fuel cell power density, Pt utilization, and electrode resistance were analyzed in comparison with randomly organized conventional E/E electrodes.

Chapter 3 employs a commercially available non-fluorinated sulfonated pentablock terpolymer membrane with varying ion exchange capacities (IECs) in reverse fuel cell/electrolytic dehumidification, in order to identify and evaluate a more cost-effective and energy-efficient alternative to replace the expensive benchmark Nafion membrane. In addition to materials selection, operation conditions, including applied potential directions and humidification levels were also examined, with the goal of providing additional insights into the water vapor transmission rate (WVTR) and water removal efficiency.

In order to expand the application of the proton-conductive non-fluorinated sulfonated pentablock terpolymers in chapter 3, these materials were evaluated as nanostructured electrodes in chapter 4. Specifically, the materials electrospinning behavior in binary solvent mixtures was explored. Chapter 4 focuses on investigating solvents influence on the solution microstructures, as well as the resulting macro properties, *i.e.,* viscosity, shear-thinning behavior, and conductivity, to provide insights of fundamental factors into improving solution electrospinability.

To further broaden the application of ionic polymers as nanofibrous solid electrolytes in water-free lithium (Li) batteries, chapter 5 investigated the electrospinning behavior and properties of a styrene-based polymerized ionic liquid (PIL) (*i.e.*, butyl imidazolium cation with lithium tetrafluoroborate anion). The influence of Li salt concentration on PIL electrospinability and resulting thermal and electrochemical properties of the Li-doped nanofibers were characterized and compared with its solution-casted film analog. The hypothesis is that nanofibrous membranes could potentially improve the interfacial contact with Li metal electrodes during cell operation.

Chapter 6 concludes with a summary of the major contributions of this dissertation towards applying ionic polymers as nanostructured membranes or electrodes in zero GHG emission electrochemical energy devices and proposes directions for further investigation.

CHAPTER 2.

3D PATTERNED ELECTRODES FOR ULTRA-LOW PLATINUM FUEL CELLS[*]

2.1. Introduction

Can the advantages of 3D patterned structure be applied to ultra-low Pt loading electrodes? In our previous study, a simultaneous electrospinning/electrospraying (E/E) technique was developed to produce unique nanofiber-nanoparticle electrodes for ultra-low Pt loading (*ca.* < 0.1 mg_{Pt} cm^{-2}) fuel cells.[82] Unlike conventional ink-based electrodes, the interaction of nanofibers and nanoparticles increases the number and connectivity of TPBs inside the electrodes, which generated high power outputs even at ultra-low cathode Pt loading (0.022 mg_{Pt} cm^{-2}). However, previously developed E/E electrodes were randomly assembled due to the nature of whipping electrospinning jets. Therefore, it would be of great interest to develop E/E electrodes containing patterned fiber mats to improve water management and further enhance fuel cell performance at ultra-low Pt loadings. Although patterned fiber mats have been utilized for tissue engineering,[83] to the best of our knowledge, it has not yet been investigated for patterned nanofiber-nanoparticle electrodes in fuel cells.

In this work, we demonstrate a novel template-assisted E/E technique as a strategy for creating organized patterned nanofiber-nanoparticle electrodes at ultra-low Pt

---

[*] Reprinted with permission from "3D patterned electrodes for ultra-low platinum fuel cells." by Yang, Y., R. Sun and Y. A. Elabd (2022). International Journal of Hydrogen Energy 47(14): 8993-9003. Copyright 2022 by Elsevier.

loadings. More specifically, photolithographed patterned templates were utilized to direct the deposition of electrospun nanofibers and electrosprayed nanoparticles during the E/E process to generate 3D patterned electrodes. Four different hexagonally patterned electrode sizes were fabricated in this study (pattern diameters of 40, 80, 160, and 360 µm). The influence of patterned E/E electrode, as well as the pattern size on fuel cell performance were investigated. The patterned electrodes were fabricated into MEAs as cathodes and the subsequent performances were evaluated in a fuel cell. The electrochemical surface area, cell resistance and power densities of the patterned electrodes were also compared with the random electrodes prepared by E/E.

2.2. Experimental Methods

2.2.1. Materials

Isopropanol (IPA; ACS reagent, ≥ 99.5%) and poly (ethylene oxide) (PEO; M_V = 400,000 g mol^{-1}) were purchased from Sigma-Aldrich. Carbon supported 20 wt% Pt catalyst (Pt/C; Vulcan XC-72) was purchased from Premetek. Nafion solution (LQ-1105) and Nafion membrane (NR-212) were purchased from IonPower. Photoresist SU-8 3050 and SU-8 developer were purchased from MicroChem. Silicon wafer (n-type, 5’’) was purchased from UniversityWafer. Gas diffusion layer (GDL; Sigracet 25BC) was purchased from Fuel Cells Etc. All materials were used as received. Deionized (DI) water with a resistivity of 16 MΩ cm was used as appropriate. Ultra-high purity grade nitrogen was purchased from Brazos Valley Welding Supply. Ultra-high purity oxygen and ultrazero grade air were purchased from Airgas. Ultra-high purity hydrogen was purchased from Praxair. All gases were used for fuel cell experiments.

2.2.2. Fabrication of Patterned Templates

The SU-8 3050 photoresists were applied on silicon wafers by spin coating (BID-TEK SP-100 Spin Coater) followed by a soft-baking procedure to achieve 60 µm thick coating. Hexagonal micro-patterns were fabricated *via* photolithographic (EVG 610 Double-sided Mask Aligner) using customized photomasks (quartz-chrome substrate, PortalPhotomask) and then washed by SU-8 developers. The depth of the pattern was controlled by spin-coating speed and UV-exposing time. After photolithography, double conductive layers (Al-120 nm and Au-30 nm) were deposited on top using an electron beam evaporator (Lesker PVD 75 E-Beam Evaporator). The patterned surface was divided into four 2 cm by 2 cm square zones. Each zone was patterned with one characteristic hexagonal internal diameter 40 µm, 80 µm, 160 µm, and 360 µm, respectively. The width and height of the hexagonal pores were 20 µm and 60 µm, respectively.

2.2.3. Template-Assisted Electrospinning/Electrospraying (E/E)

A custom-designed E/E apparatus, as illustrated in Figure 2.1(a), has been described in detail in previous work.[84] Patterned templates were fixed on the drum collector, where Nafion nanofibers and Pt/C nanoparticles were electrospun and electrosprayed simultaneously. The anode was fabricated by solely electrospraying, whereas the cathode was fabricated by template-assisted E/E. The anode electrospraying catalyst ink solution used to fabricate E/E electrodes consisted of a mixture of 20 mg of Pt/C catalyst, 400 mg of 5 wt% Nafion solution, 580 mg of isopropanol/DI water (3/1 v/v), with solids weight percent constant at 4 wt% for all E/E experiments. The mixture was sonicated for at least 3 min before electrospraying. For cathode, the catalyst ink composition was similar to the anode catalyst ink solution with the exception of the Nafion solution. The electrospinning polymer solution used to fabricate cathode electrodes was a 10 wt% 20/1 Nafion/PEO polymer solution, *e.g.*, 5 mg of PEO, 100 mg of dried Nafion flakes, and 945 mg of 3/1 v/v isopropanol/water. The polymer solution was stirred at ambient temperature for at least 12 hours to ensure the complete dissolution of Nafion and PEO. The catalyst ink and the polymer solution were used in the electrospraying and electrospinning processes respectively, with the Pt loading controlled by the E/E duration. The needle tip to collector distances, applied voltages, and solution flow rates were 15 and 9 cm, 7 and 15 kV, 0.3 and 0.8 mL h^{-1} for the electrospinning and electrospraying processes, respectively.

2.2.4. Membrane Electrode Assembly (MEA) Fabrication

After electrodes were fabricated *via* template-assisted E/E, the electrodes were transferred from the patterned templates to Nafion membranes. This was accomplished by gently pressing a bare Nafion membrane onto a patterned electrode and then gently peeling away the Nafion membrane together with the transferred patterned electrode, as shown in Figure 2.1(b). Nafion membranes with transferred patterned electrodes were then combined with GDLs to fabricate membrane electrode assemblies (MEAs) by sandwiching the Nafion membrane/patterned cathode between a bare GDL (cathode substrate) and an electrosprayed GDL (anode), and hot pressed (3851-0, Carver) for 5 min at 275 °F (135 °C) and 600–800 psi (4.1–5.5 MPa), as shown in Figure 2.1(c). At least three MEAs at each of five different cathode pattern sizes (D = random, 40, 80, 160, 360 µm) were fabricated for a total of fifteen E/E MEAs in this study.

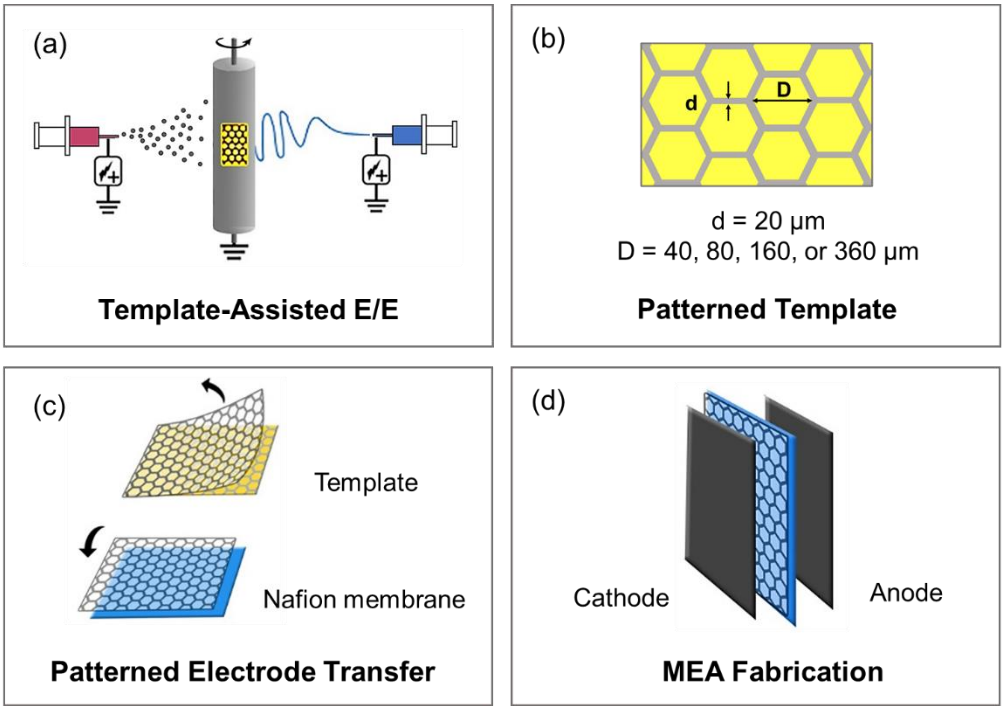

Figure 2.1 Experimental schematic: (a) template-assisted E/E apparatus, (b) patterned template diameter sizes, (c) patterned electrode transfer from patterned template to Nafion membrane, and (d) MEA fabrication.

2.2.5. Electrode Characterization

The morphology of the patterned electrodes was characterized by an optical microscope (Eclipse Ti-E Inverted Microscope, Nikon Instruments) and scanning electron microscopy (SEM; FEI Quanta 600 FE-SEM). For cross-sectional area characterization, Nafion supported electrodes were soaked in liquid nitrogen for 15 minutes, and then cut with a doctoral blade immediately. All samples were sputter-coated (Cressington 208 HR) with 6 nm Platinum/Iridium before SEM analysis. To analyze the nanofiber and nanoparticle size distribution, 50 counts for each sample were randomly sampled and analyzed using ImageJ software.

The Pt loading was measured with thermal gravimetric analysis (TGA; Q50, TA Instrument). A small portion of the electrode (*ca*. 4 – 6 mg) was heated from 25°C to 900 °C at 10 °C min^{-1} in the air at 60 mL min^{-1}. The Pt loading was determined by dividing the residual weight at 850 °C by the original sample area (all other components degrade below 800 °C except for Pt). The average Pt loading for each patterned electrode was determined using at least 2 – 4 electrodes.

2.2.6. Fuel Cell Tests and Cyclic Voltammetry (CV)

Each MEA (1.21 cm^2 area) was placed between two serpentine flow field graphite plates (1 cm^2 flow area) separated by two 0.152 mm thick PTFE/fiberglass gaskets (Cat. No. 33, Scribner Associates, Inc.). The entire fuel cell assembly consisted of an MEA, two gaskets, and two flow plates placed between copper current collectors followed by endplates all held together by bolts with 100 lb in (11.3 N m) of applied torque. Fuel cell performance of each MEA was evaluated with a fuel cell test station (850C, Scribner Associates, Inc.). Fuel cell tests were conducted under ambient pressure with saturated (100% RH) anode and cathode flow rates of 0.43 L min^{-1} hydrogen and 1.02 L min^{-1}

oxygen at 80 °C, respectively. Fuel cell performance was recorded after a new MEA was fully activated. The activation process consists of operating the MEA at 0.7 V for 1 h, followed by 0.6 V, 0.4 V, and 0.2 V for 30 min at each voltage, and ending with two cycles of 0.6 V and 0.4 V for 30 min at each voltage. Polarization curves (cell voltage *versus* current density) were collected from the open-circuit voltage (OCV) to 0.2 V at increments of 0.05 V min^{-1} to determine that no further increase in current density at a constant voltage was observed, thus the MEA was at steady state. After the MEA was fully activated and reached a steady state, five polarization curves were collected to determine the average maximum power density. The average error between polarization curves was < 3% for the hydrogen/oxygen experiments.

Cyclic voltammetry (CV) was performed on a fully activated MEA with a potentiostat (Solartron SI 1287A, Corrware Software) at 20 mV s^{-1} from 0.01 V to 1 V versus NHE under ambient pressure. In this two-electrode configuration, the anode serves as both the counter and reference electrodes. The fuel cell anode and cathode were supplied with 0.04 L min^{-1} hydrogen and 0.02 L min^{-1} nitrogen, respectively. Temperatures of the cathode gas, anode gas, and cell were maintained at 30 °C. The Pt catalyst was assumed to have an average site density of 210 μC cm^{-2} [85]. The electrochemical surface area (ECSA) was determined from the hydrogen adsorption area from 0.1 to 0.3 V. Five cycles were taken to determine the average ECSA for each MEA. Linear sweep voltammetry was performed at 2 mV s^{-1} from OCV to 0.8 V versus NHE to determine if the MEA had any defects that resulted from internal shorts or significant hydrogen crossover.

2.2.7. Electrochemical Impedance Spectroscopy

Electrochemical impedance spectroscopy (EIS; Solartron SI 1260A) was performed on a fully activated MEA from 1 MHz to 1 Hz at 0.4 V *versus* NHE under ambient pressure. In this two-electrode configuration, the anode serves as both the counter and reference electrodes. The fuel cell anode and cathode were supplied with 0.43 L min^{-1} hydrogen and 1.02 L min^{-1} oxygen, respectively. Temperatures of the cathode gas, anode gas, and cell were all maintained at 80 °C. The EIS data was analyzed using the classic equivalent circuit models that consisted of a resistor (resistance of the solid electrolyte membrane) in series with a parallel circuit of a constant phase element and a second resistor (resistance of the electrode) that is typically used to describe a porous electrode[86].

2.3. Results and Discussion

2.3.1. Patterned Electrode Morphology

Figure 2.2 shows images of the patterned electrode morphologies fabricated *via* template-assisted E/E. Figure 2.2(a) shows the patterned electrodes supported on a transparent Nafion membrane substrate fabricated by decal transfer (Figure 2.1(c)). The decal transfer was facile due to the higher affinity of the electrode to the flexible Nafion membrane compared to the rigid metal-coated silicon wafer templates. Brightfield optical microscopy images of all electrodes are shown in Figure 2.2(b-f), where each image corresponds to a specific feature size (hexagonal pattern diameter D = 40 µm, 80 µm, 160 µm, 360 µm; random). In contrast to the morphology of the random oriented electrode (shown in Figure 2.2(f)), the organized hexagonal patterned features are clearly demonstrated in Figure 2.2 (b-e). Nafion nanofibers and Pt/C nanoparticles collected on patterned template and form honeycomb structured electrode (darker area in Figure 2.2(b-e)) demonstrating the template-assisted E/E technique has the ability to guide the well-controlled nanofiber-nanoparticle deposition in the range of few tens to few hundreds of microns.

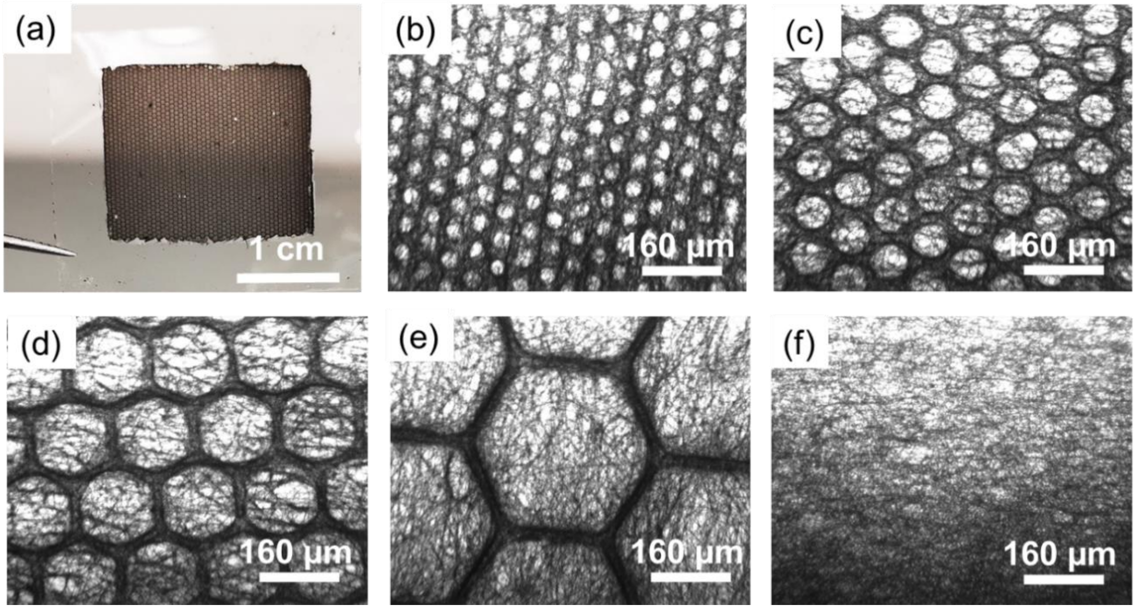

Figure 2.2 Images of patterned electrode morphology. (a) Photo of the patterned electrode transferred onto Nafion membrane substrate, and optical microscope images for E/E electrodes with hexagonal pattern diameters of (b) 40 µm, (c) 80 µm, (d) 160 µm, (e) 360 µm and (f) random morphology.

Figure 2.3 shows the SEM images of the top and cross-sectional views of the E/E patterned electrodes. Individual hexagonal patterned structures with different feature sizes under high magnification were shown in Figure 2.3(a-d). The E/E catalyst layers show a highly porous microscopic morphology with interconnected nanofibers and particle aggregates. More importantly, the hexagonal patterns organize nanofibers and nanoparticles into catalyst-dense walls and catalyst-thin openings, which could act as reservoirs for the collection and removal of produced water during fuel cell operation, specifically at high current density where the water generation rate is more significant. The solid phase electron and proton conduction could be enhanced through the organized nanofiber/nanoparticle bundles, whereas the gas phase mass transport resistance could be mitigated through the catalyst-thin openings, where both effects in combination could promote enhanced TPBs. Moreover, by incorporating rigid catalyst particles into 3D scaffolds, the mechanical strength of the patterned electrodes could be enhanced, which may facilitate the preservation of the organized structure during subsequent processing and fuel cell operation.

Figure 2.3(e-h) demonstrate electrodes with the visible replicated pattern under lower magnification, which confirms that the collector efficiently directs the internal micro-construction of the nanofiber-nanoparticle electrodes. As the pattern diameter increases, the conductive area guiding the nanofiber deposition decreases, which results in less control of forming a well-defined hexagonal patterned fiber mat. Figure 2.3(i-l) displays the freeze-fractured cross-sectional area of the electrodes, representing the depth-direction structure consisting of nanofibers and nanoparticles with a similar average thickness ranging between 10 to 20 µm regardless of the pattern size.

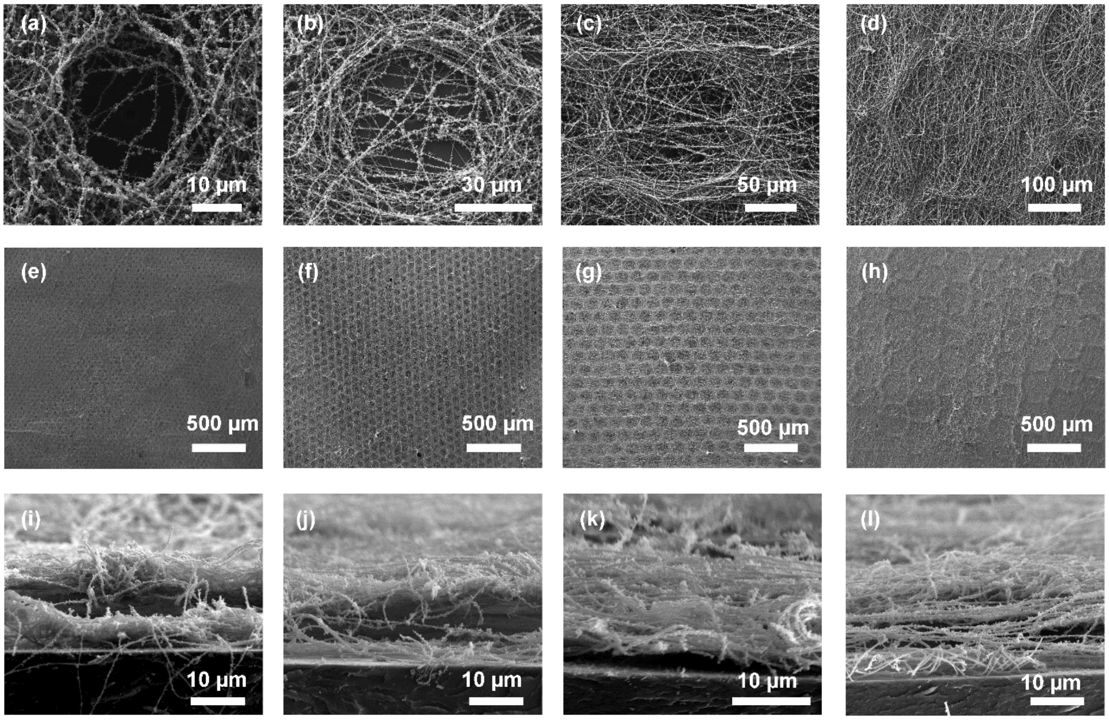

Figure 2.3 SEM images of E/E patterned electrodes with diameters of 40 µm (a,e,i), 80 µm (b,f,j), 160 µm (c,g,k), and 360 µm (d,h,l): **(**a-d) top view of individual hexagonal feature (X 5000 magnification, scale bar = 10 µm), (e-h) top view of patterned electrode surface (X 100 magnification, scale bar = 500 µm) and (i-j) cross-sectional view of patterned electrodes (X 5000 magnification, scale bar = 10 µm).

Figure 2.4(a-b) shows the average Nafion nanofiber and Pt/C catalyst nanoparticle diameters based on quantitative analysis of the SEM images shown in Figure 2.3(a-d). The results show that the average fiber diameters range from 220 ± 35 nm to 272 ± 38 nm and the average particle diameters range from 0.81 ± 0.20 µm to 0.98 ± 0.21 µm, indicating that the fiber and catalyst aggregate sizes are similar for all electrodes regardless of the hexagonal feature sizes. These results suggest that the template-assisted E/E technique can solely adjust micron-scale pattern structure without affecting the nano-scale morphology, validating the sole investigation of the pattern size effect.

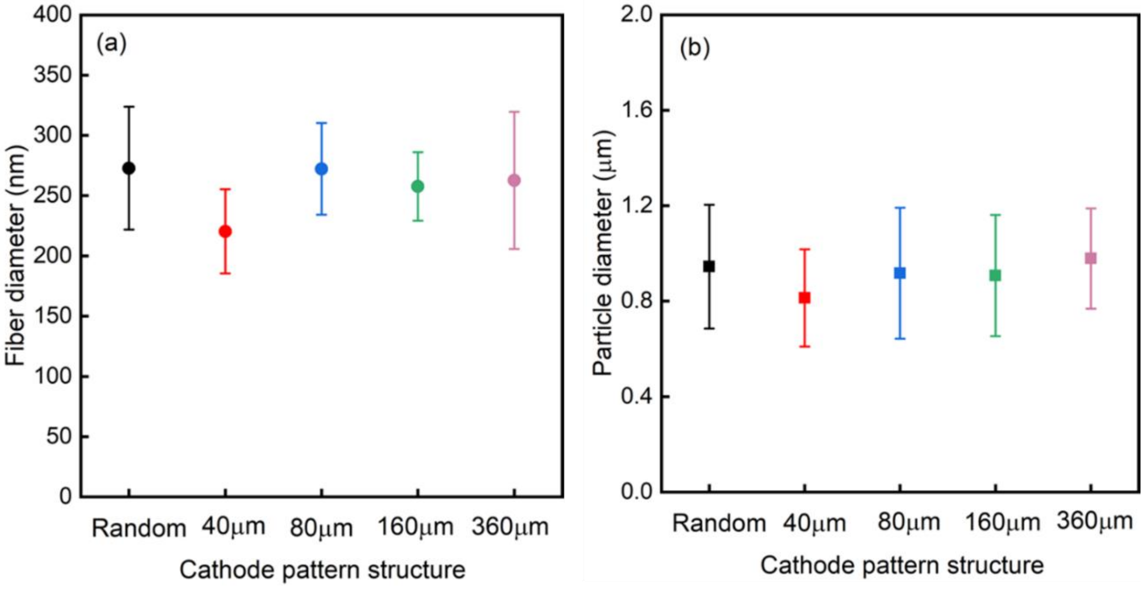

Figure 2.4 (a) Nafion nanofiber diameters and (b) Pt/C catalyst nanoparticle diameters in electrodes as a function of cathode pattern structure.

2.3.2. Fuel Cell Performance and Electrochemical Characterization

Figure 2.5 shows the polarization and power density curves of MEAs with patterned electrodes measured under standard operating conditions (*i.e.*, fully humidified H_2/O_2 at 80 °C under ambient pressure), with cathode Pt loadings of *ca.* 0.05 mg_{Pt} cm^{-2} (see Table 2.1 for detailed results). Patterned E/E electrodes with four pattern diameters achieved peak power densities ranging from 418 mW cm^{-2} (360 µm) to 481 mW cm^{-2} (80 µm). Specifically, the electrode with an 80 µm diameter pattern outperformed the rest of other pattern sizes, exhibiting a maximum power density of 481 mW cm^{-2} and an 18% improvement compared to the random electrode with a power density of 402 mW cm^{-2}. This maximum peak power density is comparable with studies by González *et al.*,[22] Hwang *et al.*,[84] and Cooper *et al.*[87] with ultra-low Pt loading. For electrode with larger pattern sizes (*i.e.*, 160 µm and 360 µm), less of an enhancement over the random electrode was observed likely due to the sparse hexagonal openings (Figure 2.3(c, d)), which may impact mass transport and the TPBs in the electrode.

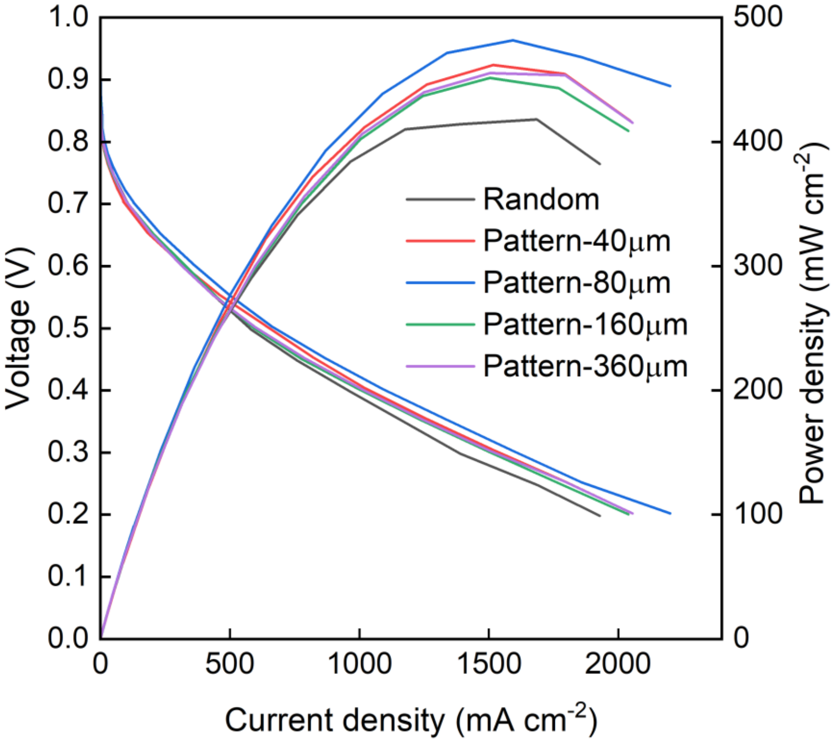

Figure 2.5 Fuel cell polarization and power density curves for MEAs with the random electrode (black) and patterned electrodes at 40 µm (red), 80 µm (blue), 160 µm (green), 360 µm (purple) pattern diameter, measured with 100% RH hydrogen/oxygen at 80 °C under ambient pressure.

To further understand the impact of the patterned morphology on fuel cell performance, *in situ* cyclic voltammetry (CV) was performed to characterize the electrochemical surface area (ECSA). Figure 2.6 shows CVs of MEAs with the random electrode and patterned electrodes at various pattern diameters, 40 µm, 80 µm, 160 µm, and 360 µm. The cathode Pt loading were maintained at a similar level (*ca.* 0.05 mg_{Pt} cm^{-2}) for consistent comparison. During CV measurements, the adsorption and desorption of hydrogen ($H_2 \leftrightarrow 2H^+ + 2e^-$) occur at available Pt sites in the range from 0.1-0.3 V. As demonstrated in Table 2.1, the ECSAs of the 40 µm pattern size (22.6 m^2 g_{Pt}^{-1}) and 80 µm pattern size (33.7 m^2 g_{Pt}^{-1}) electrodes increase compared to the random electrode (20.0 m^2 g_{Pt}^{-1}). At 80 µm pattern size, the ECSA reached the highest value and exhibits a 68% increase compared to the random electrode. This increase can be attributed to the increase in electrode macroporosity, which may allow for more liquid water product during fuel cell operation to be expelled out and alleviate the flooding issue at high current densities; also, more oxygen could penetrate though the electrode and improve access to active Pt catalyst sites. With the further increase of pattern size to 160 µm and 360 µm, the ECSAs decreases from 33.7 m^2 g_{Pt}^{-1} (80 µm) to 29.8 m^2 g_{Pt}^{-1} (160 µm) and 22.8 m^2 g_{Pt}^{-1} (360 µm), respectively, which are still 49% and 14% higher than the random control. Overall, the ECSAs provide direct evidence for higher Pt utilization in patterned electrodes compared to random electrodes under similar cathode Pt loading, and corroborate with the fuel cell power performance results (Figure 2.5).

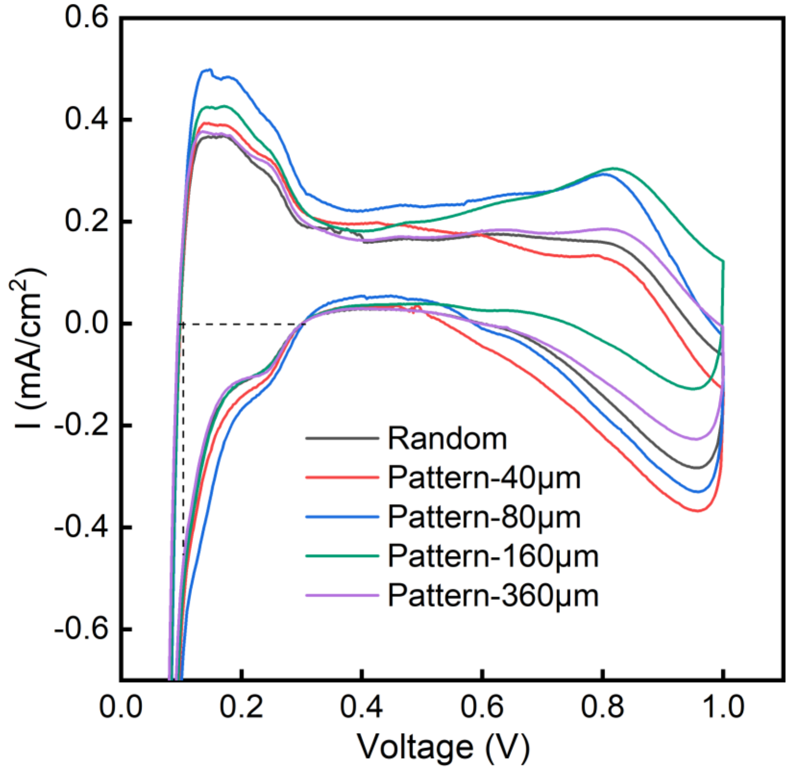

Figure 2.6 Cyclic voltammograms for MEAs with the random electrode (black) and patterned electrodes at 40 μm (red), 80 μm (blue), 160 μm (green), 360 μm (purple) pattern diameters. The ECSA integration area (0.1-0.3V) for hydrogen adsorption peak is indicated by the dashed black lines.

Table 2.1 Fuel cell and electrochemical performances of E/E patterned electrodes

Cathode structure	**Pt loading (mg$_{Pt}$ cm^{-2})**		**Max power density[a] (mW cm^{-2})**	**Pt utilization[a,c] (kW g$_{Pt}^{-1}$)**	**ECSA[b] (m^2 g$_{Pt}^{-1}$)**	**Electrode resistance[a] (mΩ cm^{-2})**
	Anode	**Cathode**				
Random	0.034	0.060	405.1 ± 11.0	5.82 ± 0.16	20.0	320.8
Pattern-40μm	0.027	0.061	451.0 ± 45.9	6.78 ± 0.69	22.6	368.9

Pattern-80µm	0.024	0.056	462.6 ± 69.4	8.26 ± 1.24	33.7	322.4
Pattern-160µm	0.043	0.028	439.1 ± 51.5	5.87 ± 0.69	29.8	353.8
Pattern-360µm	0.026	0.061	418.4 ± 72.6	7.23 ± 1.25	22.8	445.7

[a] Under H_2/O_2 at 80 °C, ambient pressure.
[b] Under H_2/N_2 at 30 °C, ambient pressure.
[c] Normalized by the total Pt loading inside MEA.

Figure 2.7 shows the averaged maximum power densities as a function of the cathode electrode pattern structure. As the pattern size evolves from random to 40 µm pattern, the averaged peak power densities increased from 405 mW cm^{-2} to 451 mW cm^{-2}, then reached the maximum at 462.6 mW cm^{-2} for 80 µm pattern. Further increasing pattern sizes to 160 µm pattern induced a slight power density drop to 439 mW cm^{-2}, and further down to 418.4 mW cm^{-2} for the largest 360 µm pattern. However, one could argue that these power densities differences are not significant in light of the statistical error among repeated experiments shown in the graph. Therefore, a better measure is to normalize the peak power densities, *i.e.*, Pt utilization or normalized peak power densities as shown in Figure 2.7(b). Following a similar trend as Figure 2.5, significant increases in the normalized maximum power density was observed for electrodes with smaller pattern sizes. The normalized maximum power density was 6.78 ± 0.69 kW g_{Pt}^{-1} for electrodes with 40 µm pattern, and then reached a peak value at 8.26 ± 1.24 kW g_{Pt}^{-1} for 80 µm pattern, showing 42% increment compared to the random cathode structure (5.82 ± 0.16 kW g_{Pt}^{-1}). This difference is statistically significant. For the larger pattern sizes of 160 and

360 µm, Pt utilization of 5.87 ± 0.69 and 7.23 ± 1.25 kW g_{Pt}^{-1} were observed, respectively. Overall, the Pt utilization advantages of the patterned electrodes compared to the random electrodes are clearly demonstrated.

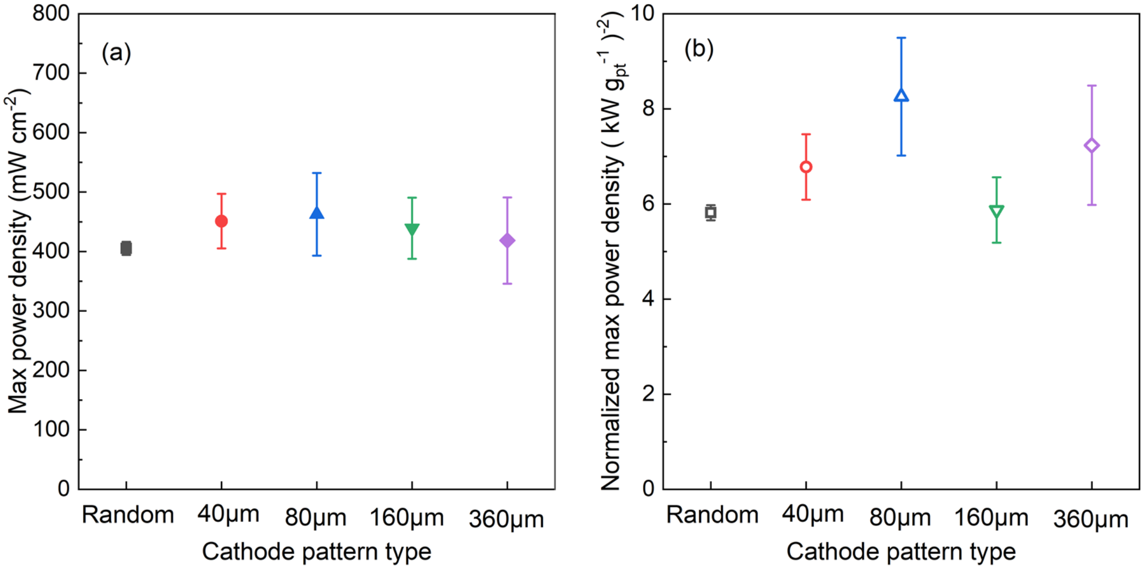

Figure 2.7 (a) Maximum power density (solid symbols) and (b) Pt utilization (hollow symbols) for random (black square) and patterned electrodes with 40 µm (red circle), 80 µm (blue triangle), 160 µm (green inverted triangle), and 360 µm (purple diamond) diameter sizes.

The electrode resistance was measured by the electrochemical impedance spectroscopy (EIS) (Table 2.1). The measurements were conducted under hydrogen/oxygen at ambient pressure at 80 °C at 0.4 V *versus* NHE, a voltage at which the ohmic and transport resistances are dominant. The random electrode showed a resistance of 320.8 mΩ cm^{-2}, similar to the results in a previous study (321.48 mΩ cm^{-2} with 0 wt% Nafion in the electrospraying catalyst ink)[84]. The 80 µm patterned electrode demonstrated the lowest resistance of 322.4 mΩ cm^{-2}, suggesting more triple phase boundary connections with lower proton and mass transfer resistance throughout the hexagonal pattern. The 360 µm patterned electrode showed the highest resistance of 445.7 mΩ cm^{-2} among all patterned electrodes; the larger pattern size may result in less triple phase boundary connections comparatively and lower connectivity of the proton conducting nanofibrous network. The hypothesized water management schematic is illustrated in Figure 2.8. The fuel cell performance (averaged anode and cathode Pt loading, maximum power density, Pt utilization, ECSA, and electrode resistance) of the patterned electrodes and random electrode are listed in Table 2.1.

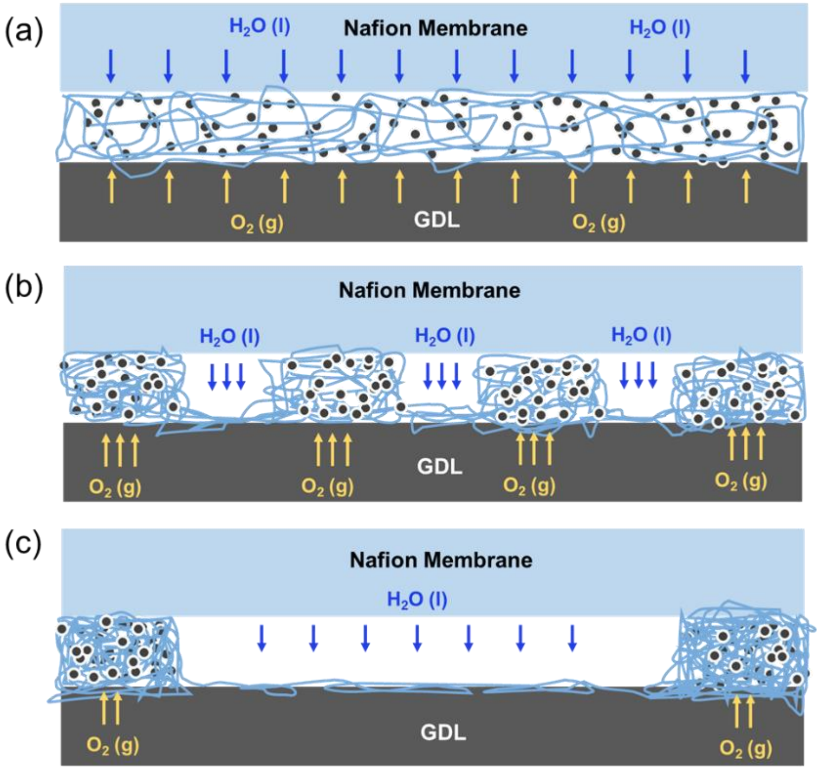

Figure 2.8 Cathode water management schematic (cross-sectional). (a) random morphology, (b) patterned morphology with appropriate size and (c) patterned morphology with overly large size.

2.3.3. Mechanical Properties of Patterned Nanofibers

Mechanical properties can reflect the processability of patterned electrodes and the ability to maintain a robust and integrated configuration during fuel cell operation. The cross-sectional SEM images of the patterned Nafion fiber mats are shown in Figure 2.9(a, b), with a thickness of *ca.* 15 µm. To get more insight into the effect of patterns on the mechanical properties of the fibrous structure, tensile strength measurements were performed on the patterned high purity Nafion (95 wt%) nanofiber constructs produced via template-assisted electrospinning (as shown in Figure 2.9). Young's modulus, ultimate tensile strength and elongation to break properties of the fiber network are listed in Table 2.2. The 40 µm, 80 µm and 160 µm patterned fiber network showed Young's modulus of 9.27 MPa, 9.27 MPa, and 9.06 MPa, respectively, revealing higher stiffness compared to the random control (5.43 MPa) and 360 µm patterned fiber network (5.71 MPa). All patterned fiber network showed similar elongation to break compared to the random control without significant difference. Intuitively, we expected the fiber network mechanical properties to be compromised due to the patterned structure, however, the patterned porous structures appear to have improved stiffness and ultimate tensile strength compared to the random network structure. This result could be attributed to the increased strength through the fiber bundles due to the patterned structure. The patterned fiber network with organized fiber bundles improved the alignment of the fibers in the tensile direction, whereas the random constructs failed to control individual fiber orientation.

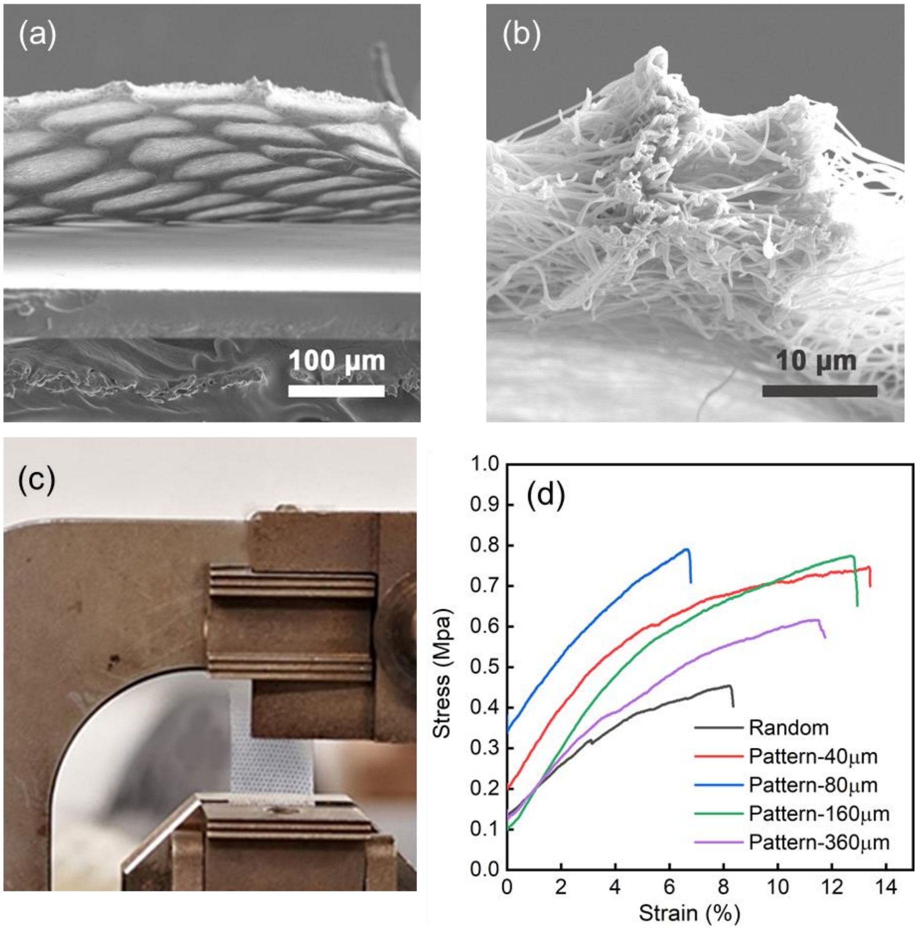

Figure 2.9 (a) SEM image of a perspective view of freeze-fractured patterned fiber networks looking underneath, (b) higher magnification of the circled area in (a) showing the fiber mat thickness, (c) electrospun patterned high purity Nafion fiber networks (95 wt% Nafion) fixed to the dynamic mechanical analyzer (DMA) and (d) stress-strain profiles of Nafion fiber networks with the random (black) and patterned morphology at 40 µm (red), 80 µm (blue), 160 µm (green) and 360 µm (purple) pattern diameter sizes, measured at 25 °C, 47% RH.

Table 2.2 Mechanical properties of high purity Nafion fiber networks.

Cathode structure	Young’s modulus (MPa)	Ultimate tensile strength (MPa)	Elongation to break (%)
Random	5.43	0.455	8.7
Pattern-40μm	9.27	0.747	13.4
Pattern-80μm	9.27	0.790	6.7
Pattern-160μm	9.06	0.774	12.9
Pattern-360μm	5.71	0.616	11.5

2.3.4. Conclusions

In this study, we demonstrated a template-assisted E/E technique for fabricating unique nanofiber-nanoparticle PEMFC electrodes with 3D hexagonal patterned features, ranging from 40 μm to 360 μm in diameter. Owing to the open and interconnected hexagonal architecture, the nanofiber-nanoparticle patterned electrodes show enhancements compared to non-patterned electrodes possibly due to enhanced triple phase boundaries and enhanced porosity and water management. With a ultra-low cathode Pt loading of 0.06 mg_{Pt} cm^{-2}, hexagonal patterned electrodes with 80 μm diameter demonstrated a Pt utilization of 8.26 kW g_{Pt}^{-1}, showing 42% increase when compared to the randomly assembled electrode (5.82 kW g_{Pt}^{-1}). Furthermore, the mechanical strength of the Nafion fiber mats were not compromised by the pattern structure. Patterned electrode fabricated by template-assisted E/E technique show great promise for the future development of low-cost fuel cell vehicles with high power density and ultra-low Pt loading.

CHAPTER 3.

DEHUMIDIFICATION *VIA* POLYMER ELECTROLYTE MEMBRANE ELECTROLYSIS WITH SULFONATED PENTABLOCK TERPOLYMER

3.1. Introduction

In order to displace the conventional Nafion membrane due to its disadvantages (*e.g.*, expensive, toxic gases release above 150 °C, extensive supporting equipment), serval alternative hydrocarbon materials have been proposed. Examples include poly(phenylene sulfone) (sPPS),[88] sulfonated poly(ether ether ketone) (sPEEK),[89] sulfonated poly(sulfone),[90] sulfonated polybenzimidazole (sPBI),[91] *etc*. However, most of these PEMs are targeted for water electrolyzers rather than air humidification.[13] Recently, A commercially available sulfonated pentablock terpolymer, namely NEXAR®, has found wide applications[92-94] due to its unique multi-block architecture. The midblock of NEXAR® contains partially sulfonated polystyrene providing moisture and ion conductivity, while the remaining blocks were designed to provide both wet strength and dry flexibility.[95] In 2019, Filice *et al.*[80] first applied NEXAR® membrane liquid water-splitting and demonstrated NEXAR® membranes possess higher water uptake and can generate higher current densities than the Nafion control. However, no NEXAR® performance has been systematically investigated in an electrolytic dehumidifier with water vapor instead of liquid water as the feedstock.

In this study, NEXAR® membranes with two different ion exchange capacities (IECs of 1.0 and 2.6 meq g^{-1}, *i.e.*, NEXAR-1.0 and NEXAR-2.6) were investigated in a

PEM electrolytic air dehumidifier and compared to the benchmark Nafion 117 membrane (*i.e.*, NAFION-0.9). The impact of the material properties (*i.e.*, polymer chemistry and IECs) and direction of applied potential (*i.e.*, concurrent and countercurrent) were investigated under both high and low relative humidity (RH) cases. Water vapor transmission rate (WVTR) and water removal energy efficiency were analyzed from the viewpoints of materials, potential direction, and humidity. In addition, electrochemical analysis (*i.e.*, current densities, polarization curves, and electrode resistances) were performed and the results were correlated with the dehumidification performance.

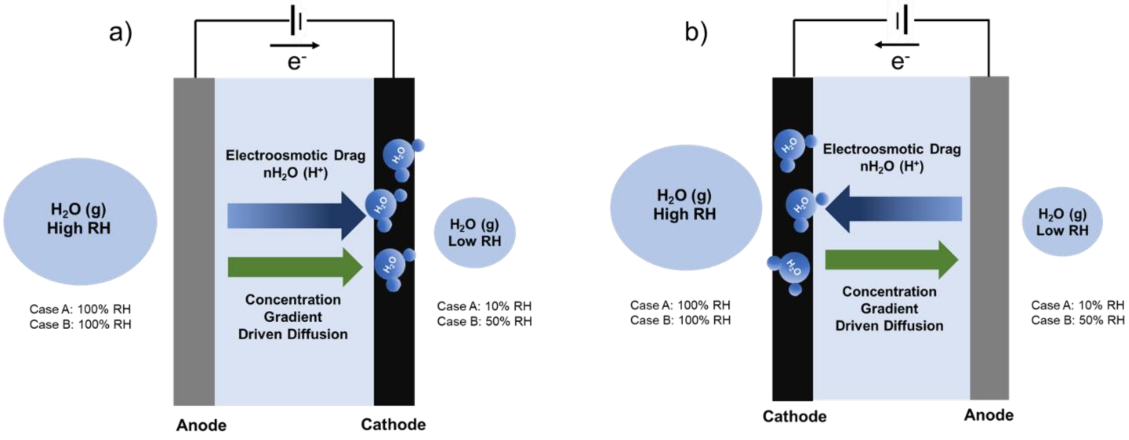

Figure 3.1 PEM electrolysis dehumidification (3V) with diffusion and electroosmotic drag with a) concurrent and b) countercurrent applied potential.

3.2. Experimental Methods

3.2.1. Materials

A sulfonated pentablock terpolymer, also commercially known as NEXAR®, was provided by Kraton Corporation. The chemical structure of NEXAR® is shown in Figure 3.2 and contains a symmetric A-B-C-B-A structure with tert-butyl-styrene (tbS) as the outer A block, hydrogenated isoprene (HI) as the B block, and a selectively sulfonated polystyrene (s-PS) as the middle C block. The unsulfonated pentablock terpolymer precursor has a number-averaged molecular weight (M_n) of *ca.* 68 kg mol^{-1} with M_n of respective blocks equal to *ca.* 14-8.5-23-8.5-14 kg mol^{-1}. In this work, NEXAR® at this molecular weight was received at two different sulfonation levels, corresponding to ion exchange capacities (IEC) of 1.0 and 2.6 meq g^{-1}, respectively. All NEXAR® samples were received as dried films. 1-Propanol (nP; ≥ 99.5%) and tetrahydrofuran (THF; ≥ 99.5%) were purchased from Aldrich and used as received. Ultrapure deionized, reverse osmosis (RO) water (resistivity ~ 16 MΩ cm) was used as appropriate.

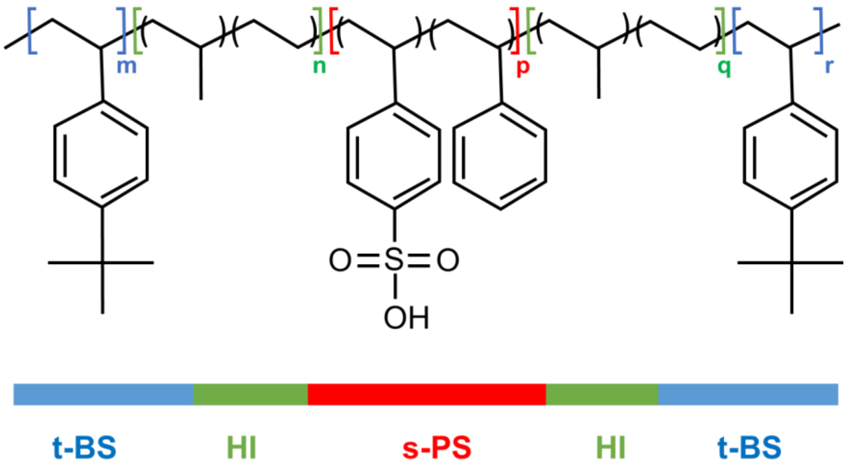

Figure 3.2 Chemical structure of the sulfonated pentablock terpolymer NEXAR®.

Titanium screen (0.002-inch thickness, 62% open area), gas diffusion layer (GDL, Toray Carbon Paper 120, Wet Proofed), Iridium Oxide catalyst (Ir/IrO_x), and Pt/C catalyst (60% Platinum on Vulcan XC 72 carbon) were purchased from Fuel Cell Etc. Nafion dispersion (alcohol based 1000 EW at 5 wt%, Dupont D520) and Nafion membrane (Nafion 117, 1100EW, 0.91 meq g^{-1}, 180 µm dry thickness) were purchased from Ion Power Inc.

3.2.2. NEXAR® Membrane Preparation

NEXAR® membranes were prepared by dissolving NEXAR® as-received films in a THF/1-propanol (5/1 w/w) solvent mixture at 4 wt% polymer in solution and thoroughly mixing for 24 h to produce a transparent and uniform solution. Each solution was poured into a PTFE petri dish (*ca.* 3.07-inch height and 1.96-inch diameter) and was partially covered with aluminum foil to slow the rate of solvent evaporation under ambient conditions for 2–4 days. The resultant membranes were annealed under dynamic vacuum at 50 °C for 24 h to remove residual solvent. The dried membrane thicknesses were *ca.* 170–180 μm (measured with a digital micrometer; Mitutoyo; ± 0.001 mm accuracy) to match the thickness of the Nafion 117 control membrane (*ca.* 180 μm). As prepared membranes were punched into circles with a diameter of 22 mm for membrane electrode assembly (MEA) fabrication.

3.2.3. NEXAR® Membrane Characterization

Water sorption of NEXAR® membranes was measured with dynamic vapor sorption (DVS, TA Instruments Q5000). A dry polymer membrane sample was first loaded into the DVS and preconditioned at 0% RH and 50 °C until equilibrium was established to remove any residual water in the sample; equilibrium was reached when < 0.1 wt% change was observed for at least 30 min. The humidity was then systematically changed from 10% to 90% RH at 10% RH increments at 50 °C, equilibrating at each condition. The polymer water sorption (S) was calculated using the following equation: $S = (W-W_0)/W_0$, where W_0 and W are dry and wet polymer weights measured before and after each DVS experimental condition, respectively.

Proton conductivities of the membranes (*ca.* 3 cm (L) × 1 cm (W)) were measured with electrochemical impedance spectroscopy (EIS; Gamry Interface 5000E) in a four-electrode conductivity cell (BekkTech BT112, Scribner Associates, Inc.) by sweeping frequencies from 1 MHz to 0.1 Hz with an amplitude of 10 mV at 10–90% RH in 10% RH increments at 50 °C, which was controlled by a bench top environmental chamber (ESPEC). The resistance R was determined from a high x-intercept of the semicircle regression of the Nyquist plot. Conductivity was calculated by using the following equation: $\sigma = L/(AR)$, where L is the distance between the reference electrodes (*ca.* 0.43 mm) and A is the cross-sectional area of the sample ($A = Wl$; W stands for sample width and l stands for sample thickness). Samples were allowed to equilibrate for 2 h at 50 °C and each RH followed by three repeated measurements, and averages of the measurements at each condition were reported.

3.2.4. MEA Fabrication

To load catalyst onto the anode side, a Ti screen disk (*ca.* 20 mm diameter) was heat-pressed (80 °C, 1000 psi (3851-0, Carver) for 5 min) against a NEXAR® membrane disk (*ca.* 22 mm diameter) to form a membrane-supported Ti screen assembly. Note that the anode requires anti-corrosive material (*e.g.,* Ti mesh or foam) support instead of carbon support due to the carbon-induced corrosion during the OER. The anode catalyst ink was air-sprayed with an airbrush gun (AEROPRO1, Aeroblend) onto a NEXAR® membrane-supported Ti screen disk (*ca.* 20 mm diameter), as illustrated in Figure 3.3(a). The anode catalyst ink consisted of 40 mg IrO_2 catalyst, 8 mg Nafion ionomer, and 4752 mg IPA/H_2O (3/1 v/v) solvent to form a 1 wt% dispersion (sonicated for 5 min with a tip-sonicator (125 W; Q125, Qsonica; 35% amplitude) to ensure uniform dispersion). This air-spray deposition was repeated multiple times to reach a final loading of *ca.* 1.5 mg_{Ir} cm^{-2}. To avoid catalyst deposition on the membrane edge (*ca.* 1 mm wide) and short-circuiting, a Teflon sheet was punched with a 20 mm diameter hole and used as a mask during the air-spraying process.

On the cathode, catalyst ink was air-sprayed onto a GDL disk (*ca.* 20 mm diameter) to reach a Pt/C loading of *ca.* 1.0 mg_{Pt} cm^{-2}, as illustrated in Figure 3.3(a). The cathode catalyst ink consisted of 20 mg Pt/C (60% Pt loading), 10 mg Nafion ionomer, and 2970 mg IPA/H_2O (3/1 v/v) solvent to form a 1 wt% dispersion (sonicated for 5 min with a tip-sonicator (125 W; Q125, Qsonica; 35% amplitude) to ensure uniform dispersion). Both the anode and cathode substrates were weighed before and after air-spraying to determine the catalyst loading. For MEA fabrication, the anode (with anode leads), membrane, and cathode (with cathode leads) were heat-pressed (with catalyst-coated sides facing membrane) at 80 °C for NEXAR® membranes, and at 135 °C for the control NAFION-0.9 membrane with an optimized pressure of 1000 psi for 5 min to enhance the contact among layers and avoid delamination.

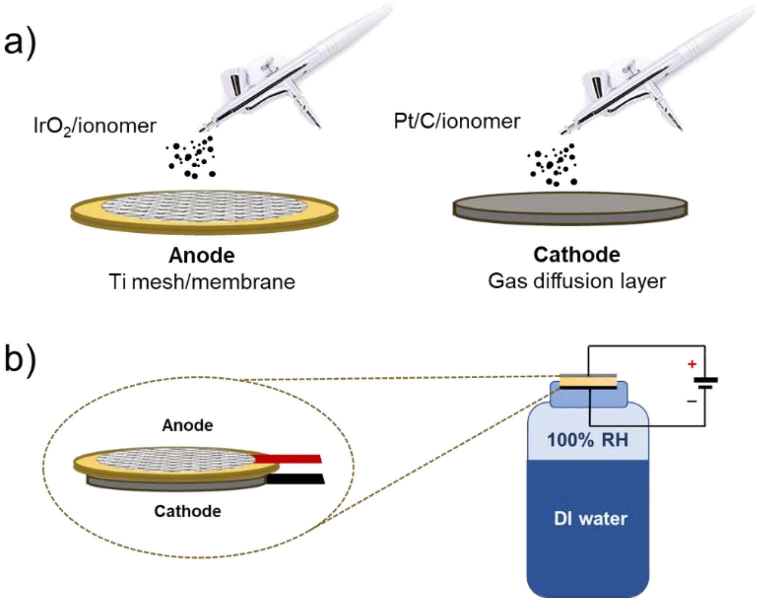

Figure 3.3 MEA fabrication schematic. (a) Air-spraying catalyst ink onto the anode (membrane supported Ti mesh) and the cathode (GDL) respectively, (b) a heat-pressed MEA on top of a testing vial with an applied voltage.

3.2.5. Water Vapor Transmission Rate (WVTR)

WVTR is defined as the steady-state vapor transport rate per unit area and can be calculated using Equation 3.1, where Δm is the weight change of the sample, Δt is the time duration, and A is the water vapor penetrating area ($2.01\ cm^2 = 0.000201\ m^2$). In this study, a positive WVTR value represents a water transmission direction from the inside of the vial (high RH side) to the outside environment (lower RH side), while a negative WVTR value represents a reversed water transmission direction, suggesting the voltage-driven water flux exceeds the concentration driven flux.

$$WVTR\ [g\ m^{-2}\ day^{-1}] = \frac{\Delta m\ [g]}{A\ [m^2] \cdot \Delta t\ [day]} \qquad \text{Equation 3.1}$$

The MEA was sandwiched between an open-top cap and the glass vial (open-top storage vial, 20 ml, Chemglass) illustrated in Figure 3.3(b). The vial cap is screwed tightly with a rubber gasket between MEA and glass vial to ensure an air-tight seal, with the anode and cathode leads extended externally. The MEA loaded testing vial was filled with DI water to create a saturated 100% RH within the vial, then placed inside a bench top environmental chamber (ESPEC) with controlled temperature and RH. The weight changes of each vial were recorded as a function of time to determine the WVTR. Three experiments were conducted for each membrane type and averaged WVTR results were reported.

In this study, two testing conditions (*i.e.*, case A and case B) at constant temperature (50 °C) and varying RH gradients were performed. In case A, the outside environmental was set at 10% RH, with a resulting water concentration gradient of Δ90% RH. In case B, the outside environmental RH was set at 50% with a resulting water concentration gradient of Δ50% RH.

To evaluate the voltage influence on the dehumidification performance, an external voltage was applied to the MEA (with positive electrode always connected to the anode of the MEA) with a potentiostat (Gamry Interface 5000E) and the current was monitored. Theoretically, the minimum theoretical electrolytical potential applied is 1.23 V,[78] however practically it is necessary to apply an overpotential to compensate for the ohmic and concentration polarization, therefore an applied potential of 3 V was selected in this work to reach a satisfactory dehumidification rate.

3.2.6. Electrochemical Characterization

After the MEA was fully humidified and reached steady-state, polarization curves (V–I) were collected from 1.5–3 V *vs.* E_{ref} at 20 mV s^{-1} increments. In a two-electrode configuration, the anode serves as both the counter and reference electrodes. For each sample, five polarization curves were collected to ensure repeatability with an average error less than 3%.

EIS measurements were performed to provide accurate and non-destructive detection of dehumidifying elements resistance evolution as function of frequency.[68] EIS was performed from 1 MHz to 1 Hz at ambient pressure, 50 °C at 0 V, 1 V, 2 V and 3 V *vs.* E_{ref} for the stabilized MEA under a fixed RH gradient for case A and B. The Nyquist plots were analyzed using a common equivalent circuit model that consisted of a resistor (resistance of the solid electrolyte membrane) in series with a parallel circuit of a constant phase element (porous electrode capacitance) and a second resistor (porous electrode resistance), and the ohmic resistance and charge transfer resistance were reported.

3.2.7. Dynamic Dehumidification

The schematic of dynamic dehumidification performed in a closed chamber (LocknLock container, 0.28 dm^3) is illustrated in Figure 3.4. The MEA was installed on a circular opening (24 mm diameter; on the top of the chamber) as the dehumidifying element, then sealed with a rubber gasket for an air-tight seal. The apparatus was placed inside a bench top environmental chamber (ESPEC) with controlled temperature and RH. Two humidity sensors (Digital Humidity Sensor SHTC1, Sensirion, accuracy of 1.5% RH) were installed both inside and outside the sealed chamber, respectively, to record the RH change. Initially, inside and outside RH were equilibrated at 60% RH at 50°C with 0 V applied. The applied voltage was held constant and the current was monitored with a potentiostat (Gamry Interface 5000E, potentiostatic method).

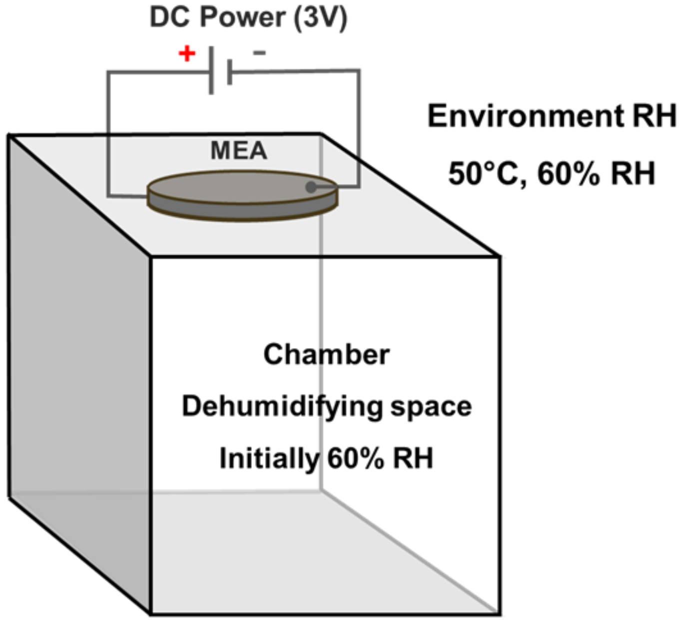

Figure 3.4 Dynamic dehumidification apparatus.

3.3. Results and Discussion

3.3.1. Membrane Properties

Table 3.1 lists the water sorption, hydration number, and conductivity at 50 °C, 90% RH for NAFION-0.9, NEXAR-1.0, and NEXAR-2.6 membranes (*i.e.*, membranes prior to MEA fabrication). The water sorption of both NEXAR® membranes (22.1 and 61.8 wt% for NEXAR-1.0 and NEXAR-2.6, respectively) are higher than that of NAFION-0.9 (15.1 wt%; similar to literature for Nafion 117 at similar conditions [96]); specifically, NEXAR-2.6 is significantly higher than both NEXAR-1.0 and NAFION-0.9. The calculated hydration number (λ, mol H_2O / mol SO_3^-) of both NEXAR® membranes are similar (12.3 and 13.2 mol H_2O / mol SO_3^- for NEXAR-1.0 and NEXAR-2.6 respectively) and slightly higher than that of NAFION-0.9 (7.5 mol H_2O / mol SO_3^-). The conductivity of NEXAR-2.6 (207.4 mS cm^{-1}) is higher than NAFION-0.9 (74.9 mS cm^{-1} , similar to literature for Nafion 117 (80 mS cm^{-1}) at similar conditions [97]), while NEXAR-1.0 (46.9 mS cm^{-1}) is lower than that of NAFION-0.9.

Figure 3.5(a) shows the equilibrium water sorption at 50°C for NEXAR® membranes and NAFION-0.9 membrane at various relative humidities, *i.e.*, water sorption isotherm. At low to medium RH levels (0–40 wt%), water sorption increases linearly with humidity for all membranes. Above 50% RH, the water sorption increases exponentially with humidity, which is commonly observed for sulfonated polymers.[98] Specifically, at 95% RH, NEXAR-2.6 (89.6 wt%) and NEXAR-1.0 (29.0 wt%) show significantly higher water sorption than NAFION-0.9 (15.8 wt%). However, NEXAR-1.0 has similar water sorption compared to NAFION-0.9 at most humidity values (< 70% RH).

Figure 3.5(b) shows the humidity-dependent hydration number (*i.e.*, λ, mol H_2O / mol SO_3^-, obtained by normalizing the water sorption with IEC) at 50 °C. Note that the hydration numbers for both NEXAR membranes are similar at all RH, and similar to NAFION-0.9 below 40% RH. Above 40% RH, NEXAR® membranes possess slightly higher hydration numbers compared to NAFION-0.9. Similar to the water sorption isotherms in Figure 3.5(a), the hydration number trends are linear for $0 < \lambda < 5$. This has been attributed to the formation of the first hydration shell around sulfonic acid moieties in the polymer.[99] The hydration number trend changes in a second regime ($\lambda > 5$), and this has been attributed to membrane swelling.[100-102] The hydration number of both NEXAR® membranes overlap at all RH, indicating similar interaction between water molecules and alkyl sulfonate moieties regardless of sulfonation level.[103] Above 50% RH, the hydration number of NEXAR® membranes is higher than NAFION-0.9, suggesting differences in ion-ion interactions between water-alkyl sulfonic acid (estimated $pK_a = -2.5$ for $-C_6H_4SO_3H$) compared to water-fluoro sulfonic acid (estimated $pK_a = -6$ for $-CF_2CF_2SO_3H$).[98, 104-107]

Table 3.1 Membrane properties

Material	IEC /meq g^{-1}	Dry membrane thickness / µm	Water sorption S^a / wt%	Hydration number λ^a / mol H_2O/mol SO_3^-	Conductivity σ^a / mS cm^{-1}
NAFION-0.9	0.9	175	12.9	7.9	74.9
NEXAR-1.0	1.0	180	22.1	12.3	46.9
NEXAR-2.6	2.6	176	61.8	13.2	207.4

[a] Measured under 50 °C, 90% RH

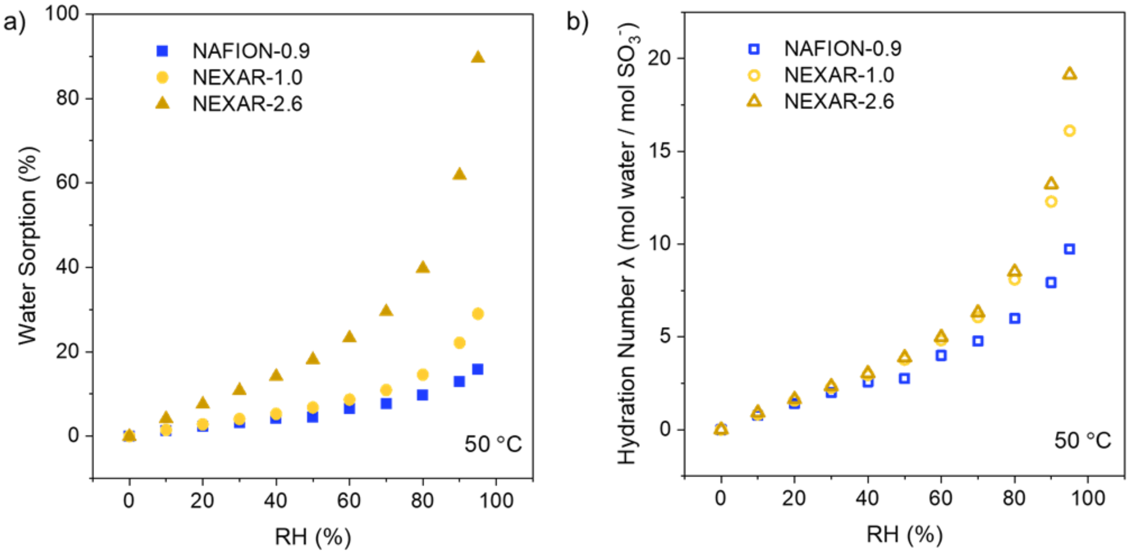

Figure 3.5 (a) Humidity-dependent water sorption and (b) humidity-dependent hydration number (λ) for NAFION-0.9, NEXAR-1.0, and NEXAR-2.6 membranes at 50 °C.

Figure 3.6(a) shows the humidity-dependent proton conductivity at 50 °C for NAFION-0.9, NEXAR-1.0 and NEXAR-2.6. The proton conductivity is approximately an order of magnitude higher at all humidities when comparing NEXAR-2.6 to NEXAR-1.0. When the humidity is low (20% RH), the conductivity of NEXAR-2.6 (3.9 mS cm^{-1}) is comparable to NAFION-0.9 (2.9 mS cm^{-1}); both higher than NEXAR-1.0 (0.5 mS cm^{-1}) at this humidity. At high humidity (90% RH), NEXAR-2.6 has a significatly higher conductivities (207.4 mS cm^{-1}) than both NAFION-0.9 (74.9 mS cm^{-1}) and NEXAR-1.0 (46.9 mS cm^{-1}).

Figure 3.6(b) shows the hydration number dependent proton conductivity at 50 °C, *i.e.*, proton conductivity as a function of normalized water content in the membranes (molecules of water per molecule of sulfonic acid). The conductivity increases exponentially with hydration number from $1 < \lambda < 4$; then increases more gradually at $\lambda > 4$. The similarity in trend when comparing NEXAR® membranes and NAFION-0.9 suggests that NEXAR® membranes follow a similar percolation model for conductivity-water.[108] NAFION-0.9 shows comparable conductivity with NEXAR-2.6 at the same hydration number although NAFION-0.9 has a lower IEC, which could be attributed to the superacidity of the perfluoroalkyl sulfonic acid compared to aryl-tethered akyl sulfonic acid and a more favorable morphology for proton conduction.[109, 110]

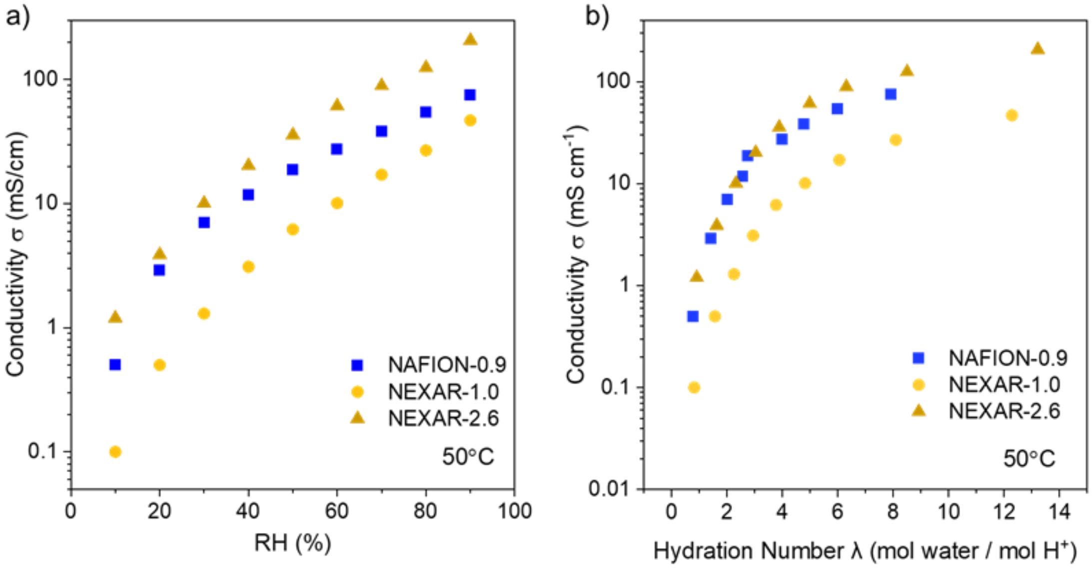

Figure 3.6 Proton conductivity *vs.* (a) relative humidity, and (b) hydration number, λ (mol H_2O / mol SO_3^-), for NAFION-0.9, NEXAR-1.0, and NEXAR-2.6 membranes at 50 °C.

3.3.2. Membrane WVTR

Figure 3.7(a) compares the WVTRs for membranes in case A (50 °C, 10–100% RH, Δ90% RH) and case B (50 °C, 50–100% RH, Δ50% RH). Note that the WVTR data in Figure 3.7 and previous figures were conducted on bare membranes (without electrodes), where experiments later in the manuscript will include electrodes on membranes referred to as membrane electrode assemblies. In case A, NAFION-0.9 and NEXAR-2.6 possess similar WVTRs (*ca.* 7500 g m^{-2} day^{-1}), which are 31% higher than NEXAR-1.0 (5106 g m^{-2} day^{-1}). The differences among WVTRs show a similar trend to the data in Figure 3.6(b), where NAFION-0.9 and NEXAR-2.6 possess similar conductivity at the same hydration number. In contrast, all three types of membranes show a lower and comparable WVTR (4100 g m^{-2} day^{-1}) in case B.

Figure 3.7(b) illustrates a one-dimensional (1-D) water concentration profile across a membrane to show the reduction in the water concentration gradient across the membrane when the external RH gradient is reduced from case A to case B. The driving force for water transport is the external humidity gradient, and the transport resistances are composed of three major parts, *i.e.*, two boundary layer resistances (l/k_f and l/k_d) and the membrane diffusion resistance (l/DK). Boundary layer resistances exist in the stagnant gas film near both surfaces of the membrane, while diffusion resistance dominates the water transport inside the membrane. The discontinuity at the gas-solid interface is due to the solubility difference between water in air compared to water inside the membrane. For a specific type of membrane, the average water content in case A is lower than case B due to a lower dry side humidity (10% RH in case A and 50% RH in case B), therefore the resulting diffusion coefficient D (*i.e.*, positively proportional to the membrane water content [111]) is also lower, suggesting the membrane resistance l/DK is higher in case A. Therefore, the intrinsic membrane properties play a more significant role in case A rather than in case B, thus the difference among samples is more pronounced in the former condition. In other words, the results in Figure 3.7 suggest that case A is membrane resistance dominant, and that case B is boundary layer resistant dominant. Therefore, the differences among the membranes and its impact on a process may be condition dependent, *i.e.*, external humidity gradient.

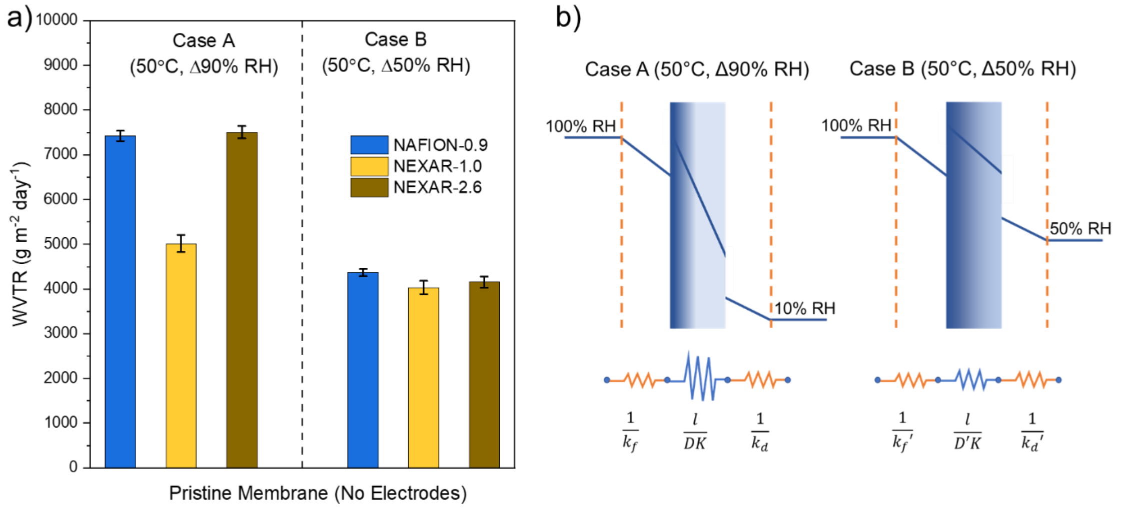

Figure 3.7 (a) WVTR for NAFION-0.9, NEXAR-1.0, and NEXAR-2.6 membranes at 50 °C and (b) an illustration of 1-D water vapor diffusion profile across a membrane (k_f, k_f' mass transfer coefficient of water from the air to the membrane; k_d, k_d' mass transfer coefficient of water from membrane to air; D diffusion coefficient; K partition coefficient, l membrane thickness). Case A (50 °C, 10–100% RH, Δ90% RH) and case B (50 °C, 50–100% RH, Δ50% RH).

3.3.3. MEA WVTR

Figure 3.8 exhibits WVTRs for all membrane electrode assemblies (MEAs; membranes with electrodes) for three separate scenarios: no applied potential (0 V), a concurrent applied potential of 3 V (3 V – concurrent) (see Figure 3.1(a)), and a countercurrent applied potential of 3 V (3 V – countercurrent) (see Figure 3.1(b)). Concurrent refers to the same direction as the water concentration gradient, while countercurrent is opposite of the water gradient. In Figure 3.8(a), for case A at 0 V, the NEXAR-2.6 MEA has a similar WVTR (6625 g m^{-2} day^{-1}) compared to the NAFION-0.9 MEA (5603 g m^{-2} day^{-1}), while 48% higher than the NEXAR-1.0 MEA (3446 g m^{-2} day^{-1}). Again, the differences among WVTR for all MEAs are similar to the trend observed in Figure 3.7(a) (case A), revealing that the membranes with electrodes similar to the membranes without electrodes show a membrane resistance dominated transport mechanism for case A. The absolute WVTRs of the MEAs without an applied potential are slightly lower than that of membranes (without electrodes) in Figure 3.7(a) due to the added resistances of the electrodes on the membranes. A concurrently applied potential (3 V – concurrent) results in higher WVTRs compared to the WVTRs with no applied potential (0 V) by 52%, 78%, and 157% for the NAFION-0.9, NEXAR-2.6, NEXAR-1.0 MEAs, respectively, due to the added voltage-driven water transport through electroosmotic drag (see illustration of the concurrently combined concentration gradient and electroosmotic drag driving forces in Figure 3.1(a)). Contrastingly, a countercurrent applied potential (3 V – countercurrent) results in lower WVTRs compared to the WVTRs with no applied potential (0 V) by 30%, 28%, and 50% for the NAFION-0.9, NEXAR-

2.6, and NEXAR-1.0, respectively, due to two opposing gradients (see illustration of countercurrent opposing concentration gradient and electroosmotic drag driving forces in Figure 3.1(b)).

For case B in Figure 3.8(b), the WVTRs for all MEAs with no applied potential (0 V) were all lower (4074, 3532, and 4939 g m^{-2} day^{-1} for NAFION-0.9, NEXAR-1.0, and NEXAR-2.6 MEAs, respectively) compared to case A in Figure 3.8(a) (5604, 3446, and 6643 g m^{-2} day^{-1}) due to a lower external water vapor concentration gradient. Similar results were observed for membranes (without electrodes) when comparing case A to case B in Figure 3.7(a). Also, similar to the results in case B in Figure 3.7(a), all the WVTRs in Figure 3.8(b) are similar across the MEAs suggesting that the MEAs are similar to the membranes (without electrodes) where at this lower water vapor concentration gradient, the boundary layer resistance is dominant. Therefore, one would predict that an applied potential may not impact the WVTRs of the MEAs. Surprisingly, Figure 3.8(b) shows both significant increases (52%, 157%, and 78% for the NAFION-0.9, NEXAR-1.0, NEXAR-2.6, respectively) and decreases (30%, 50%, and 28% for the NAFION-0.9, NEXAR-1.0, NEXAR-2.6, respectively) to WVTRs for all MEAs when the potential is applied concurrently and countercurrently, respectively. This suggests that the electroosmotic drag is significant enough to increase the membrane resistance to a level that overrides the boundary layer resistance dominance. Interestingly, negative WVTRs were observed for all MEAs with a countercurrent applied potential (-5970, -3763, -5729 g m^{-2} day^{-1} for NAFION-0.9, NEXAR-1.0, and NEXAR-2.6, respectively) demonstrating that the electroosmotic drag is so significant that it is higher than both the boundary layer and concentration gradient resistances in the concurrent direction and it actually reverses the direction of water transport by opposing both of these driving forces (see illustration of countercurrent opposing concentration gradient and electroosmotic drag driving forces in Figure 3.1(b)).

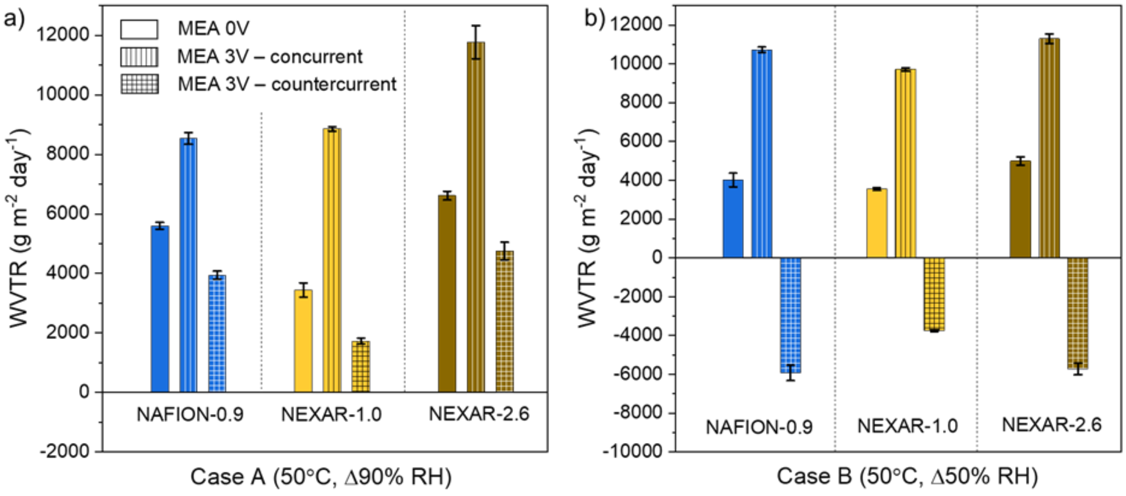

Figure 3.8 WVTRs for NAFION-0.9 MEA, NEXAR-1.0 MEA, and NEXAR-2.6 MEA. (a) Case A (50 °C, 10–100% RH, Δ90% RH) and (b) case B (50 °C, 50–100% RH, Δ50% RH).

3.3.4. Water Removal Energy Efficiency

The energy consumption is determined from voltage multiplied by the integrated current over time (Equation 3.2). The water removal energy efficiency (Equation 3.3) is defined as the ratio of voltage-driven transport per energy consumed (1g water/m^2/J).[112]

$$E\ [J] = V\int_{t1}^{t2} I dt\ [V \cdot A \cdot s] \qquad \text{Equation 3.2}$$

$$\eta\ [g\ m^{-2} J^{-1}] = \frac{\Delta\text{WVTR}\ \ [g\ m^{-2} day^{-1}] \cdot\ t\ [day]}{E[J]} \qquad \text{Equation 3.3}$$

Figure 3.10(a) shows the voltage-driven water transport ΔWVTR for all MEAs. The ΔWVTR was determined by subtracting the measured WVTR from the WVTR at 0 V as the baseline (*i.e.,* only concentration gradient-driven diffusion occurs at WVTR at 0 V). For concurrent scenario, ΔWVTR slightly increases comparing case A and B (by 129%, 14%, and 22% for NAFION-0.9, NEXAR-2.6, NEXAR-1.0 MEAs, respectively); note that the anode side humidity is constant (100% RH in both case A and B, see Figure 3.1(a)). In contrast, for the countercurrent scenario, there are significant increases of ΔWVTR from case A to B (by 502%, 325%, and 475% for NAFION-0.9, NEXAR-2.6, NEXAR-1.0 MEAs, respectively), which can attributed to the anode side (*i.e.,* dominating side) humidity changes from 10% RH (case A) to 50% RH (case B) under countercurrent (see Figure 3.1(b)). The highest ΔWVTRs are achieved by NAFION-0.9 and NEXAR-2.6 MEAs with countercurrent potential in case B (9921 and 10742 g m^{-2} day^{-1} respectively), which are 27% and 32% higher than NEXAR-1.0 MEA (7262 g m^{-2} day^{-1}).

Figure 3.10(b) shows the water removal energy efficiency; and detailed data are listed in Table 3.2. Similar to the trend observed in Figure 3.10(a), the change in water removal efficiencies from case A to B are small (by 34%, 5%, and 41% for NAFION-0.9, NEXAR-2.6, NEXAR-1.0 MEAs, respectively) with concurrent potential applied, but are significant (by 239%, 128%, and 127% for NAFION-0.9, NEXAR-2.6, NEXAR-1.0 MEAs, respectively) with countercurrent potential applied. Comparing all MEAs, even though NEXAR-1.0 MEA shows slightly lower ΔWVTR (*e.g.*, 6160 g m^{-2} day^{-1}, concurrent, case B) than NAFION-0.9 (6714 g m^{-2} day^{-1}) and NEXAR-2.6 (6296 g m^{-2} day^{-1}), NEXAR-1.0 MEA shows higher water removal energy efficiency (0.239 g J^{-1} m^{-2}) than NAFION-0.9 (0.190 g J^{-1} m^{-2}) and NEXAR-2.6 (0.155 g J^{-1} m^{-2}) under the same condition due to less energy consumption. The results suggest NEXAR-1.0 MEA is more energy efficient in voltage-driven water transport. In comparison, although NEXAR-2.6 MEA (*e.g.*, -10765 g m^{-2} day^{-1}, countercurrent, case B) shows slightly higher ΔWVTR to NAFION-0.9 MEA (-9925 g m^{-2} day^{-1}), the energy efficiency of NEXAR-2.6 MEA (0.116 g J^{-1} m^{-2}) is surprisingly lower than NAFION-0.9 MEA (0.193 g J^{-1} m^{-2}) due to its excessive water sorption (see Figure 3.5(a)) and energy consumption, suggesting that if excess water is absorbed by a membrane it could lead to ineffective current consumption.

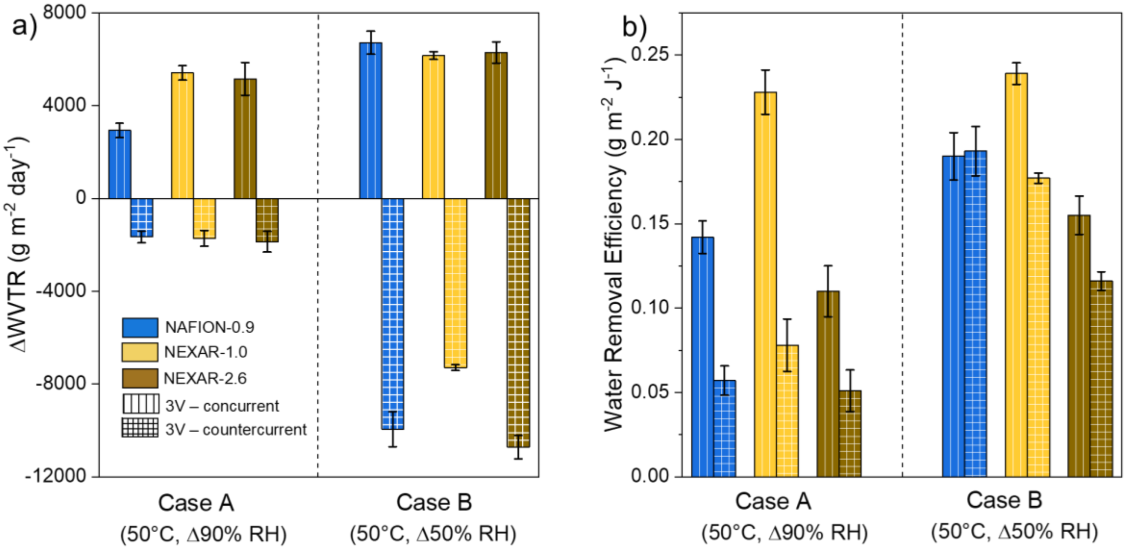

Figure 3.9 (a) ΔWVTR and (b) water removal efficiency comparison for NAFION-0.9, NEXAR-2.6, and NEXAR-1.0 MEAs with 3 V – concurrent (line pattern) and 3 V – countercurrent (cross pattern) in case A and B.

Table 3.2 Water removal energy efficiency

a) Case A: 50 °C, 100% RH–10% RH, Δ 90% RH

[a] Sample	Integrated area (A·s)	Total run time (s)	Energy consumption (A·V·s)	Average current $\langle I \rangle_{t1,\,t2}$ (mA)	ΔWVTR (g·m^{-2}·day^{-1})	Water removal energy efficiency η (g·J^{-1}·m^{-2})
NAFION-0.9 concurrent	1415.37	17753	4246.10	79.7	2932	0.142
NAFION-0.9 countercurrent	2133.50	19100	6400.51	111.7	1653	0.057
NEXAR-1.0 concurrent	1162.41	12720	3487.24	91.38	5412	0.228
NEXAR-1.0 countercurrent	973.66	11420	2920.97	85.26	1716	0.078
NEXAR-2.6 concurrent	2315.30	12790	6945.91	181.0	5157	0.110
NEXAR-2.6 countercurrent	3458.37	24370	10375.11	141.9	1863	0.051

[a] Measured at 3 V for all MEAs.

b) Case B: 50 °C, 100%RH–50%RH, Δ 50% RH

[a] Sample	Integrated area (A·s)	Total run Time (s)	Energy consumption (A·V·s)	Average current $\langle I \rangle_{t1,\,t2}$ (mA)	ΔWVTR (g·m^{-2}·day^{-1})	Water removal energy efficiency η (g·J^{-1}·m^{-2})
NAFION-0.9 concurrent	1443.63	10570	4330.89	136.6	6714	0.190
NAFION-0.9 countercurrent	1832.77	9216	5498.31	198.9	9942	0.193

[a] Sample	Integrated area (A·s)	Total run Time (s)	Energy consumption (A·V·s)	Average current $\langle I \rangle_{t1,\, t2}$ (mA)	ΔWVTR ($g \cdot m^{-2} \cdot day^{-1}$)	Water removal energy efficiency η ($g \cdot J^{-1} \cdot m^{-2}$)
NEXAR-1.0 concurrent	1437.02	14430	4311.07	99.6	6160	0.239
NEXAR-1.0 Counter	1714.28	10760	5142.84	159.3	7292	0.177
NEXAR-2.6 concurrent	1654.67	10590	4964.01	156.3	6296	0.155
NEXAR-2.6 countercurrent	3382.75	9498	10148.25	356.2	10720	0.116

[a] Measured at 3 V for all MEAs.

3.3.5. Electrochemical Characterization

Figure 3.10 shows the current densities as a function of time for all MEAs in case A and B. The current densities for all MEAs rapidly decreased in the initial few seconds due to the anode water reduction induced by the OER ($2H_2O \rightarrow 4e^- + 4H^+ + O_2$), and then stable current densities are observed indicating equilibrated water concentrations.[62] In both Figure 3.10(a) and 3.10(b), regardless of humidities and applied potential directions, NEXAR-2.6 MEAs show higher current densities (*e.g.*, 194.6 mA cm^{-2} in case B, 3 V – countercurrent) than NAFION-0.9 (104.6 mA cm^{-2}) and NEXAR-1.0 MEA (92.5 mA cm^{-2}) at the same condition. Comparing different applied potential directions, it is interesting to notice that countercurrent (dashed lines) generally results in higher current densities than concurrent (solid lines) (*e.g.*, 81.1 and 194.6 mA cm^{-2} for concurrent and countercurrent potentials respectively, for NEXAR-2.6 MEA in case B) at the same condition. This phenomenon is due to the difference in the water regeneration side for concurrent and countercurrent. For countercurrent (see Figure 3.1(b)), water is generated at the high RH side (100% RH), resulting in high water content and strong back-diffusion (*i.e.*, water diffuses from cathode to the anode). As a result, the back-diffused water increased the average water content inside the membrane and results in a higher current density. Contrastingly, for concurrent (see Figure 3.1(a)), water is generated at the low RH side (10% or 50% RH) , so the water drainage through diffusion or convection would be easier. Therefore, the average water content is lower, and the resulting current densities are lower.

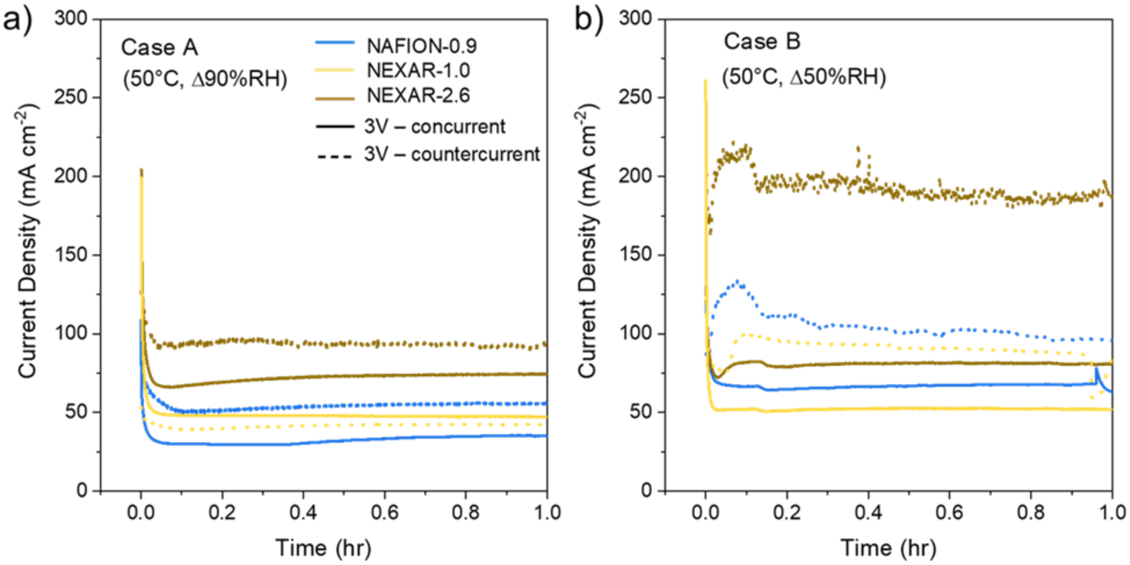

Figure 3.10 Current densities for NAFION-0.9 MEA, NEXAR-1.0 MEA, and NEXAR-2.6 MEA at 3 V – concurrent and 3 V - countercurrent. (a) Case A (50 °C, 10–100% RH, Δ90% RH) and (b) case B (50 °C, 50–100% RH, Δ50% RH).

Figure 3.11 exhibits the polarization curves for all MEAs from 1.5–3 V (with insets from 1.5–1.8 V) at different conditions. At low applied potential (see insets), the concurrent densities (solid symbols, anode facing 100% RH, see Figure 3.1(a)) are higher than countercurrent densities (open symbols, anode facing 10% or 50% RH, see Figure 3.1(b)). This suggests that when the electrolysis reaction rate is low, the current densities are dominated by the initial environmental humidity facing the anode side. However, with increasing potentials and subsequent reaction rates, the countercurrent densities increase drastically (*e.g.,* NEXAR-2.6 MEA in case A, countercurrent density increases from 0 to 113.4 mA cm^{-2}, while concurrent density only increases from 4.8 to 93.9 mA cm^{-2}), which correlates with the trend of current densities in Figure 3.9(b) and suggests the membrane water content distribution is impacted by the electrolysis reaction. In addition, all concurrent polarization curves demonstrate more significant limiting current densities (*i.e.,* voltage increases steeply without current increment) from 2.8 to 3.0 V, suggesting the concurrent scenario is more likely to suffer from mass transport limitations.

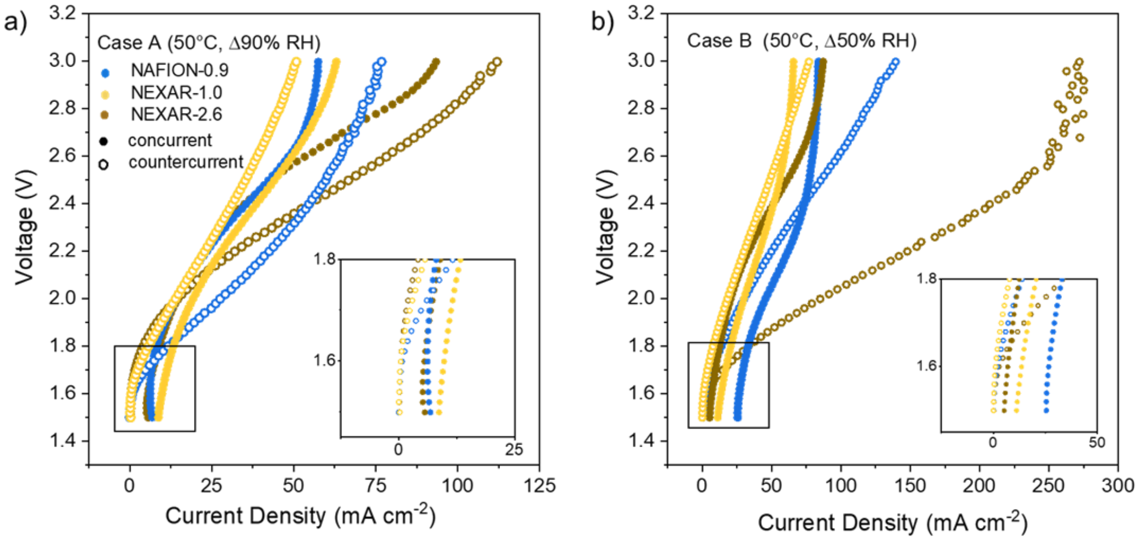

Figure 3.11 Polarization curves for NAFION-0.9, NEXAR-1.0, and NEXAR-2.6 MEAs at concurrent and countercurrent applied potential in (a) case A and (b) case B. Insets show a magnified view of polarization curves at low voltages (1.5–1.8 V).

Figure 3.12(a) shows the Nyquist plots as a function of applied potentials for NAFION-0.9 MEA as an example. The Nyquist plots were regressed to an equivalent circuit model shown in the inset, with two serial RC-circuits representing two processes with distinct time constants in series (*i.e.*, smaller time constant for the charge transfer process evident at high frequency, and larger time constant for the diffusion process evident at low frequency[113]). The membrane bulk resistances R_Ω (high-frequency intercepts) remain *ca.* 2.02 Ω regardless of varying potentials, while charge-transfer resistances R_{ct} (reflected as the diameter of the first semi-circle) change significantly. With no applied potential (0 V), a 45° tail results from the infinite diffusion resistance. As the voltage increases from 1 V to 2 V, charge transfer resistance first decreases from 4.05 Ω to 3.01 Ω due to the enhanced kinetics and then increases to 6.42 Ω at higher voltage (3 V) due to higher mass transfer resistance induced by insufficient reactants supply.

Figure 3.12(b) summarizes R_Ω and R_{ct} for all MEAs. Case A demonstrates significantly higher R_Ω (1.25–5.77 Ω) than case B (0.60–2.07 Ω) for all MEAs due to lower environmental humidity and insufficient membrane hydration. The charge transfer resistance R_{ct} in case A is slightly higher (2.52–6.43 Ω) than in case B (1.08–4.75 Ω) for all MEAs, suggesting that kinetics is also affected by the water reactant supply rate difference. NEXAR-2.6 MEA shows lower R_Ω (0.60–2.14 Ω) at both concurrent and countercurrent conditions compared to NAFION-0.9 (1.00–3.08 Ω) and NEXAR-1.0 MEAs (1.73–5.78 Ω) due to higher IEC and water sorption (see Figure 3.5), although it does not necessarily translate into the highest water removal energy efficiency as discussed previously in Figure 3.9(b).

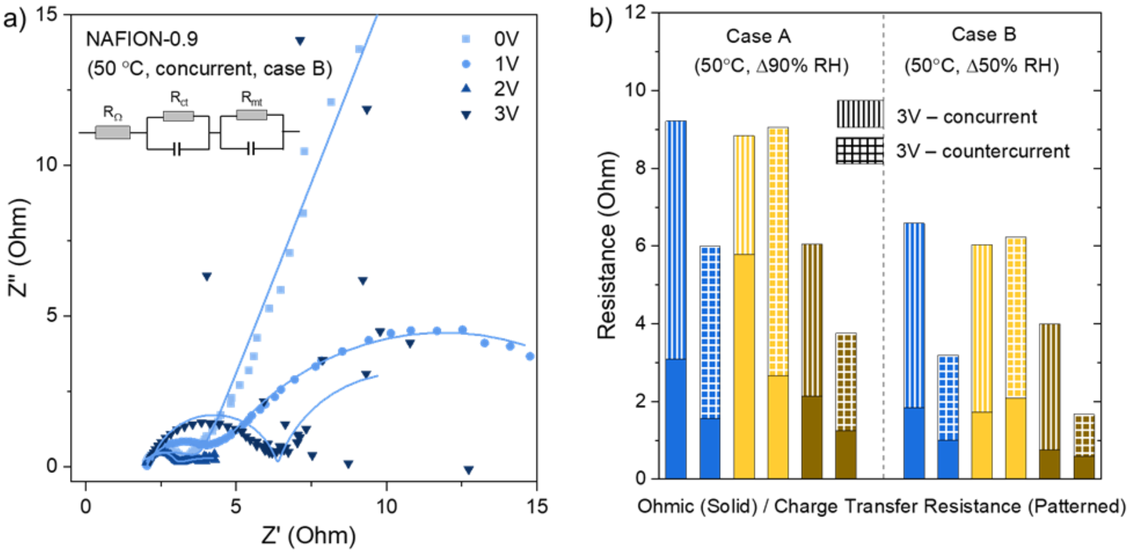

Figure 3.12 (a) Nyquist plots for NAFION-0.9 MEA as a function of applied potential (0 V, 1 V, 2 V, and 3 V applied concurrently in case B), (b) resistances for all MEAs in case A and B at 3 V, 50 °C.

3.3.6. Dynamic Dehumidification

Figure 3.13 shows the dynamic environment (chamber humidities and current densities evolution *vs.* time) with a countercurrently applied potential of 3 V. Initially, similar fast current density drops were also observed similar to Figure 3.9, and then gradually stabilized. The chamber humidities are gradually reduced from an initial rate of 1.29% RH min^{-1} until the concentration gradient-driven and the voltage-driven water transport rates are equal. In less than 1 h, internal chamber humidities are reduced from an initial 60% to 27% and 22% RH for NEXAR-1.0 and NEXAR-2.6 MEA, respectively, while NAFION-0.9 shows a higher final humidity of 34% RH. The stabilized current density for NEXAR-1.0 MEA (21 mA cm^{-2}) is lower than NEXAR-2.6 MEA (34 mA cm^{-2}) and NAFION-0.9 MEA (27 mA cm^{-2}), which is consistent with the steady-state water removal energy efficiency results in Figure 3.10(b); NEXAR-1.0 MEA exhibits higher energy efficiency (0.0545 g J^{-1} m^{-2}) than NAFION-0.9 (0.0266 g J^{-1} m^{-2}) and NEXAR-2.6 MEA (0.0342 g J^{-1} m^{-2}).

Table 3.3 lists the detailed dynamic dehumidification results. The averaged WVTR is calculated according to Equation 4.[62] Compared to the water removal efficiency (0.051–0.228 g J^{-1} m^{-2} in case A, 0.116–0.239 g J^{-1} m^{-2} in case B for all MEAs) shown in Figure 3.10(b), the results of dynamic dehumidification are generally lower (0.0266–0.0545 g J^{-1} m^{-2}) due to a lower initial interior chamber humidity of 60% RH, confirming the membrane hydration influence on dehumidification efficiency. Overall, the results demonstrate that NEXAR-1.0 show comparable dehumidification performance to NAFION-0.9 MEA, while consuming less energy, showing great promise as a less expensive and more efficient alternative for Nafion.

$$\frac{\Delta m_g}{A \cdot \Delta t}[g\ m^{-2} day^{-1}] = \frac{V\ [m^3] \cdot \rho_{g,sat}\ [g\ m^{-3}] \cdot (RH_{start} - RH_{end})[\%]}{100 \cdot A\ [m^2] \cdot \Delta t\ [day]} \tag{4}$$

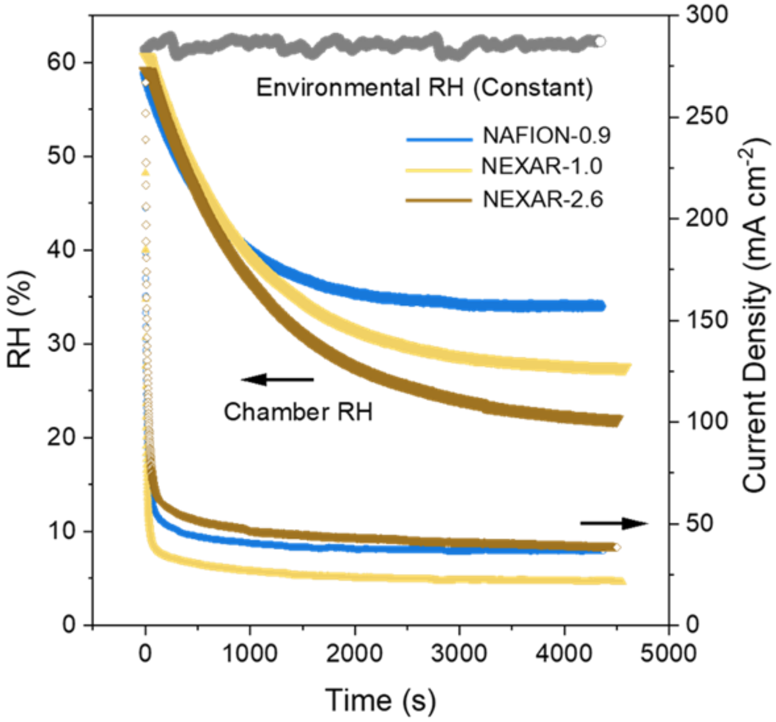

Figure 3.13 Dynamic dehumidification (time-resolved internal chamber RH and current densities) for NAFION-0.9, NEXAR-1.0, and NEXAR-2.6 MEAs, at 50 °C and initial internal chamber 60% RH.

Table 3.3 Dynamic dehumidification for an enclosed chamber

[a] Sample	RH_{start} (%)	RH_{end} (%)	Removed water Δm_g (g)	Averaged WVTR (g m^{-2} day^{-1})	Energy consumption (J)	Water removal energy efficiency (g J^{-1} m^{-2})
NAFION-0.9	58.80	33.97	0.0055	528	1044.5	0.0266
NEXAR-1.0	60.62	27.38	0.0074	710	681.8	0.0545
NEXAR-2.6	59.01	21.89	0.0083	797	1213.0	0.0342

[a] Measured at countercurrently applied 3 V for all MEAs.

3.4. Conclusions

In this study, a hydrocarbon-based sulfonate pentablock terpolymer membrane NEXAR® with different IECs (NEXAR-1.0/NEXAR-2.6, IEC 1.0/2.6 meq g^{-1}) was fabricated into MEAs to evaluate the electrolytic dehumidification performance and was compared to the benchmark Nafion membrane (NAFION-0.9, IEC 0.9 meq g^{-1}). The impact of the material properties (*i.e.*, polymer chemistry, IECs) on the WVTR and water removal efficiency were investigated under different RH conditions and voltage directions. Comparatively, the NEXAR-1.0 MEA showed the highest water removal energy efficiency (0.239 $g \cdot J^{-1} \cdot m^{-2}$) due to a well-balanced trade-off between energy consumption and dehumidification rate. NEXAR-2.6 MEA showed the highest ΔWVTR (10720 $g \cdot m^{-2} \cdot day^{-1}$), but lowest efficiency (0.116 $g \cdot J^{-1} \cdot m^{-2}$), likely due to overly high membrane water sorption and higher water back diffusion. The environmental humidity plays a significant role by influencing the hydration level of the membrane. More specifically, the anode side hydration was found to be a critical factor in controlling the WVTR. Regarding the direction of applied potential, concurrently applied 3 V was observed to be more energy-efficient than countercurrent. Furthermore, a dynamic dehumidification process was demonstrated in an enclosed chamber, and both NEXAR-1.0 and NEXAR-2.6 MEA could reduce interior humidity from the initial 60% RH down below 25% RH within an hour. Overall, the results in this study demonstrate that the sulfonated pentablock terpolymer has great potential to be applied in electrolytic air dehumidification devices as a less expensive and more energy-efficient alternative PEM.

CHAPTER 4.

SULFONATED PENTABLOCK TERPOLYMER ELECTROSPUN NANOFIBERS

4.1. Introduction

The combination of the concepts in the previous two chapters leads to the interest in sulfonated pentablock terpolymer nanofibers, which could potentially be incorporated in fibrous electrodes in PEM fuel cells and PEM electrolytic dehumidifiers to reduce catalyst loading and improve cell efficiency. In Chapter 2, high surface-to-volume ratio nanofibers inside porous PEMFC electrodes (*i.e.*, fabricated by E/E technique) have been demonstrated to effectively improve the proton transport, triple phase boundaries, and fuel cell performance.[114-117] In Chapter 3, a commercially available sulfonated pentablock terpolymer NEXAR® was utilized to fabricate a PEM for an energy-efficient electrolytic air dehumidifier; however, the electrodes were still fabricated *via* traditional air-spraying method involving catalyst ink containing high catalysts loading (*i.e.*, 1.0 mg_{Pt} cm^{-2} for cathode and 1.5 mg_{Ir} cm^{-2} for anode). Therefore, systematic investigation of electrospinning properties of NEXAR® to facilitate future nanofiber-nanoparticle fuel cell or electrolytic dehumidifier electrodes with low catalyst loading is of significant interest.

Electrospinning, as a well-established and widely used approach for nanofiber production due to its simplicity and scalability, serves to increase the efficacy of polyelectrolytes in electrochemical devices due to the large surface area, high contact efficiency, and dimensional stability.[114, 118, 119] For example, Wang *et al.*[82] demonstrated enhancement in catalyst utilization and fuel cell power densities by incorporating electrospun Nafion in nanofibrous form as ionomers. Dong *et al.*[120] also showed that an order of magnitude higher proton conductivity was achieved for a single electrospun Nafion nanofiber compared to a bulk film due to nanoscale confinement. The electrospinability of polymer solutions is strongly influenced by the inherent solution properties, such as viscosity, surface tension, and conductivity.[121, 122] In the electrospinning process, a high DC voltage (*ca.* 5–25 kV) is applied to a polymer solution, forcing the pendant drop at the needle tip to distort into a conical shape known as "Taylor cone." Above a critical voltage, concentrated charges result in high repulsive forces, which overcome the surface tension of the solution, and a charged polymer jet is ejected and accelerated towards the grounded collector in the form of a randomly deposited fibers.[118, 123, 124] It can be anticipated that under a steady electrospinning condition, a delicate balance is governed by the viscoelastic forces, surface tension, and electrostatic forces acting upon the Taylor cone, which are all directly related to the intrinsic polymer solution properties.[125]

Although the approach of electrospinning neutral polymers is well-established, electrospinning of polyelectrolytes was reported to be difficult.[126, 127] The difficulty in electrospinability can be attributed to the significant difference in fundamental properties of the polyelectrolytes compared to neutral polymers due to the electrostatic charges along the polymer backbone.[118] In contrast with the viscosity of neutral polymer, which is dominated by the molecule weight and solid concentration, the viscosity and conductivity of polyelectrolytes are closely related to ion pairs and ion clusters and their interaction with solvents.[128] For instance, the widely used perfluorosulfonic acid (PFSA) polymer (commercially known as Nafion) cannot be electrospun alone because of low mechanical relaxation time[129] and insufficient chain entanglement[118].

Chen *et al.*[130] showed that high solution conductivity of poly(ionic liquids) resulted in an order of magnitude lower fiber diameter compared to the neutral polymers with equivalent concentration. Due to the intrinsic charges of the polymer, factors that can influence ionic group interactions and charges distribution (*e.g.*, the addition of salts and ionic liquids, solvent polarity modification) will impact the solution electrospinability and the resulted fiber morphology significantly. McKee *et al.*[131] found that increasing salt concentration in polyelectrolytes could stabilize the electrospinning jet due to the charge screening effect. Josef *et al.*[127] also showed that adding methanol to dimethylformamide (DMF)-based polyelectrolytes solutions can screen the charges and decrease the degree of counterion disassociation, thus enabling a neutral chain structure favoring fiber formation.

Multiblock polyelectrolytes electrospinning has been rarely reported due to its high complexity.[126] Although the solution behavior and bulk film morphologies of NEXAR®, a commercial sulfonated pentablock terpolymer introduced in Chapter 3, has been widely investigated,[132-138] few studies have explored it in nanofibrous form. NEXAR® contains both hydrophobic (t-BS/HI) and hydrophilic (s-PS) domains, which could be separated during the fiber ejection process and form proton-conductive channels.[139] These channels may lead to rapid proton transport, thus high electrochemical performance. In this study, we aim to correlate the electrospinability and the resulting fiber morphology with the intrinsic solution properties of NEXAR® solutions with different ion exchange capacities (IECs). The effect of solvent polarity was investigated utilizing two binary solvent systems, including toluene (nonpolar) or tetrahydrofuran (THF, intermediate polar) mixed with 1-propanol (strong polar, ranging 0–50 wt% concentration). Both microscopic (*i.e.*, ionic aggregation sizes, solution structure) and macroscopic (*i.e.*, viscosity, conductivity, electrospinability) properties were systematically investigated.

4.2. Experimental Methods

4.2.1. Materials

Toluene (anhydrous, 99.8%), tetrahydrofuran (THF; anhydrous, ≥ 99.9%), and 1-propanol (ACS reagent, ≥ 99.8%) were purchased from Sigma-Aldrich. Ultrapure deionized reverse osmosis (RO) water (resistivity *ca.* 16 MΩ cm) was used as appropriate. Dry compressed air was provided using an industrial air compressor (IRN50H-0F, Ingersoll Rand Industrial Technologies).

The sulfonated pentablock terpolymers NEXAR® were provided by Kraton Corporation (Houston, TX). The chemical structure, molecular weight for each block of NEXAR® polymer are shown in Chapter 3, Figure 3.2. In this study, NEXAR® was received in two different sulfonation levels, corresponding to ion exchange capacities of 1.0 meq g^{-1} (*ca.* 29 mol % sulfonation) and 2.0 meq g^{-1} (*ca.* 52 mol % sulfonation), represented by NEXAR-1.0 and NEXAR-2.0, respectively. All NEXAR® samples were received as films. The polymer solutions were prepared by dissolving NEXAR-1.0 or NEXAR-2.0 in the desired solvent mixture at a fixed 20 wt% solid concentration. Solutions were thoroughly stirred at ambient temperature for at least 12 h to ensure complete dissolution before use. The relative polarity of the solvent mixtures was modified by adjusting the ratio of 1-propanol to the base solvent (toluene or THF).

4.2.2. Electrospinning Apparatus

The electrospinning apparatus in this study (Figure 4.1) consists of a high-voltage power supply (CZE1000R, Spellman High Voltage Electronics Corporation and ES40P-10W/DAM, Gamma High Voltage Research, Inc.), a syringe pump (NE-1000, NewEra Pump Systems), a syringe (Pt. No. CG-3070-03, Chemglass Life Sciences), a syringe needle (i.d. = 0.024 in. (0.603 mm), Hamilton), and a grounded rotating drum collector (cylindrical drum covered with aluminum foil, o.d. = 4.85 cm) connected to a motor (4IK25GN-SW2, Oriental Motor) to rotate the drum at 100 rpm during the electrospinning process. The needle was connected to the high-voltage supply, which can generate positive DC voltages up to 50 kV. The electrospinning distance (*i.e.*, the distance between the tip of the needle and the collector) was kept consistent at *ca.* 9 cm. Positive voltages applied to polymer solutions were 15–20 kV. The solution flow rates were controlled by the syringe pump at 1.0 mL h^{-1}. All electrospinning experiments were performed at room temperature (*ca.* 24 °C) and at humidity below 20% RH (maintained by supplying dry air to the enclosed electrospinning chamber). Steady polymer jets were obtained at *ca.* 15 kV and 9 cm electrospinning distance and a flow rate of 1.0 mL h^{-1}.

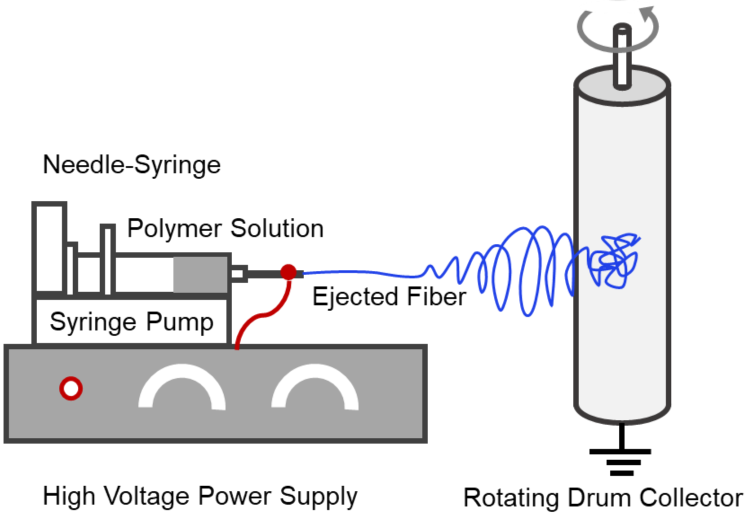

Figure 4.1 Schematic of the electrospinning apparatus.

4.2.3. Characterization

The zero-shear rate viscosity of both NEXAR-1.0 and NEXAR-2.0 were measured in both 1-propanol/toluene and 1-propanol/THF binary solvents (1-propanol ranging from 0 to 50 wt% at a constant 20 wt% solid concentration). The Reynolds number was calculated to validate the assumption of a laminar flow condition (*i.e.*, Couette flow condition; calculated by $Re = \frac{\rho u L}{\mu}$, where L is the distance between the outer surface of the spindle and the inner surface of the cylindrical sample holder).

The conductivity and viscosity of polymer solutions were measured using a conductivity meter (Apera Instruments AI502 EC700) and a viscometer (BROOKFIELD DV-II+), respectively, at ambient temperature (25 °C). The morphologies of the electrospun fibers were observed using a scanning electron microscope (SEM; FEI Quanta 600 FE-SEM, 10 kV). All samples were sputter-coated (Cressington 208 HR) with 6 nm

Platinum/Iridium before SEM analysis. The SEM images were analyzed by ImageJ software to characterize the fiber/bead size distribution.

Dynamic light scattering (DLS) measurements were performed on a nanoparticle size analyzer (Zetasizer Nano ZS, Malvern) at 25 °C. Solutions of 20 wt % NEXAR were diluted with the corresponding solvents to 1 wt%. A solid-state laser (35 mW at $\lambda = 678$ nm) was used as the light source, and the incident beam was vertically polarized with respect to the scattering plane. For each sample, three to five repeated measurements were obtained and the average of the data was reported from cumulants analysis (Zetasizer software, Malvern) to obtain apparent hydrodynamic radius (R_h).

Small-angle X-ray scattering (SAXS) data were collected using a Rigaku SMAX-3000 instrument. A rotating Cu anode operated at 40 kV and 30 mA was used to generate characteristic Cu X-rays with wavelength (λ) of 1.542 Å. The incident X-ray beam was collimated using a focusing optic and three pinholes in a 1.5 m evacuated flight path. Samples were characterized at a sample to-detector distance of 1.5 m using a Gabriel-type 2D multi-wire xenon proportional counter. The data were corrected for background noise and averaged azimuthally to give intensity as a function of momentum transfer magnitude, I(q), where $q = 4\pi (\sin \theta)/\lambda$ and 2θ is the scattering angle. The range of q spanned was 0.007 $Å^{-1}$ to 0.25 $Å^{-1}$.

4.3. Results and Discussion

4.3.1. Electrospun Nanofiber Morphology

Figure 4.2(a–f) shows the SEM images of the electrospun products (*i.e.*, beads and fibers) for NEXAR-1.0 in 1-propanol/toluene binary solvents. At 0 wt% 1-propanol (*i.e.*, pure toluene), only big droplets of 867.7 ± 318.0 µm diameter were observed (Figure 4.2(a)). As 1-propanol concentration increases from 0 wt% to 9 wt%, the big droplets evolved into smaller droplets of 67.8 ± 15.4 µm diameter. At 17 wt% 1-propanol, discrete particles with reduced diameters of 10.3 ± 2.8 µm were observed. When 1-propanol concentration increased to 25 wt%, beaded fibers (*i.e.*, bead diameter of 2.1 ± 0.9 µm, fiber diameter of 150.2 ± 60.0 nm) started to form. At 33 wt% 1-propanol, defect-free nanofibers with 160.4 ± 30.9 nm diameters were formed. However, as 1-propanol concentration further increased to 50 wt%, hindered fiber formation and reduced fiber productivity was observed due to increased solution viscosity.

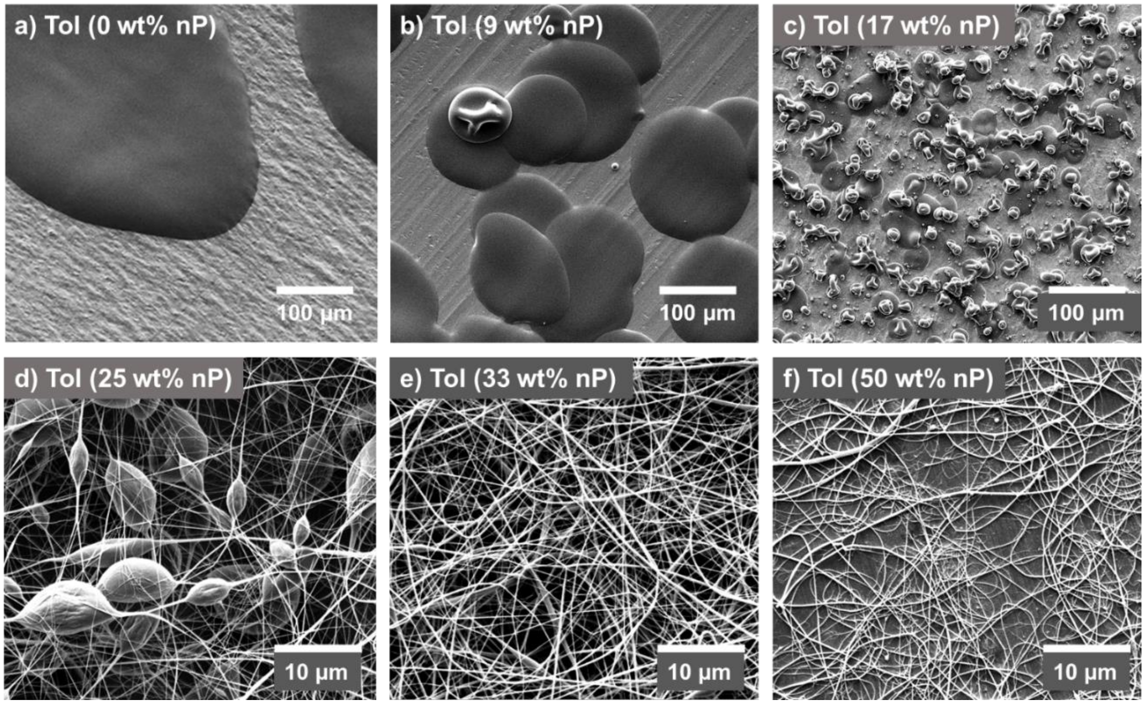

Figure 4.2 (a – f) Electrospinning product of NEXAR-1.0 polymer dissolved in toluene with different ratio of 1-propanol (0 wt% - 50 wt%).

Figure 4.3(a–c) shows the SEM images of the electrospun products (*i.e.*, beads and fibers) for NEXAR-2.0 with 1-propanol/toluene binary solvent mixtures. Note that, NEXAR-2.0 is insoluble in 100 wt% toluene or at low 1-propanol concentrations (< 25 wt%). At 25 wt% 1-propanol, only a few particles with diameters of 20.4 ± 13.6 µm were observed. At 33 wt% 1-propanol, beaded fibers with defects (*i.e.*, bead diameter of 26.6 ± 8.4 µm, fiber diameter of 245.2 ± 58.9 nm) were formed. Further increasing 1-propanol to 50 wt% resulted in thicker fiber bundles together with larger particles diameter of 396.3 ± 124.8 µm. Overall, the results in Figure 4.2 and Figure 4.3 demonstrate that adding 1-propanol in toluene can modify the solution electrospinability for both NEXAR® solutions, even though NEXAR-1.0 and NEXAR-2.0 display different morphologies at the same solvent composition due to IEC variance.

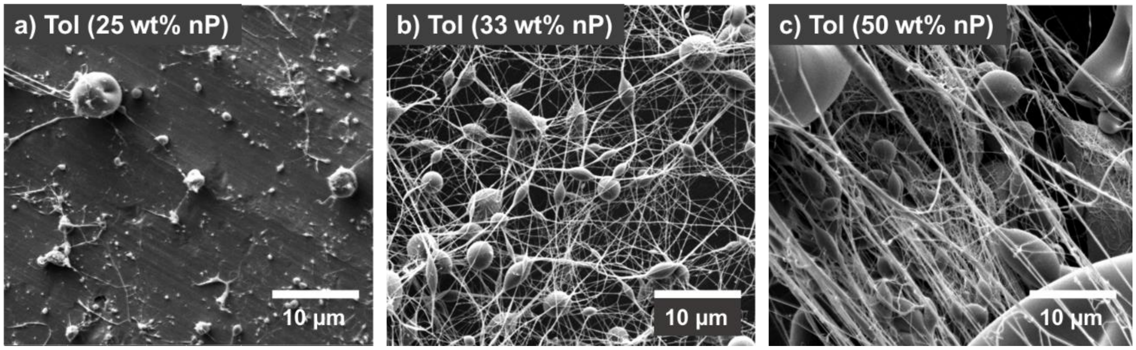

Figure 4.3 Electrospun NEXAR-2.0 in 1-propanol/toluene binary solvent mixtures with various 1-propanol concentrations: (a) 25 wt%, (b) 33 wt%, and (c) 50 wt%.

Changing the base solvent from toluene to THF induces noticeable changes in the electrospinning behavior of both NEXAR polymers. As shown in Figure 4.4(a–d), NEXAR-1.0 forms uniform nanofibers with 447.5 ± 95.0 nm diameter in THF based binary solvent mixture, even with a low 1-propanol concentration of 9 wt%. The uniform and smooth nanofiber morphologies are maintained at higher 1-propanol concentrations of 17 wt% and 25 wt% without significant changes in nanofiber diameter (*i.e.*, 571.2 ± 162.2 nm for 17 wt% and 606.1 ± 120.0 nm for 25 wt%, respectively). At 33 wt%, the nanofiber production rate is reduced, and a slight decrease in fiber diameter (291.5 ± 61.0 nm) can also be observed.

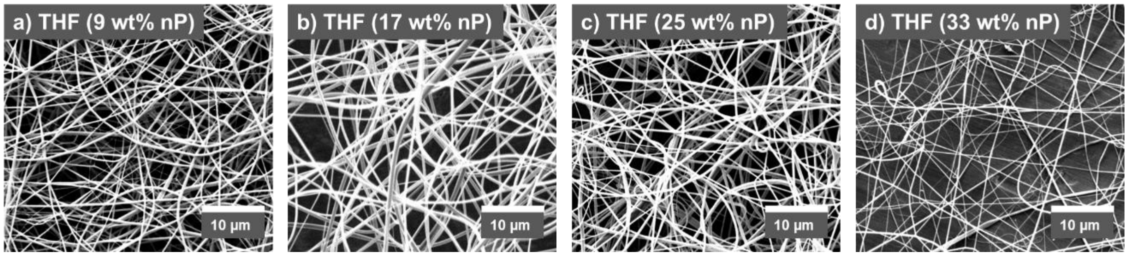

Figure 4.4 Electrospun NEXAR-1.0 in 1-propanol/THF binary solvent mixtures with various 1-propanol concentrations: (a) 9 wt%, (b) 17 wt%, (c) 25 wt%, and (d) 33 wt%.

For NEXAR-2.0, the 9 wt% 1-propanol in THF solution only produced a few fiber strands (Figure 4.5(a)). With 1-propanol concentration increased to 17 wt%, uniform nanofibers with 208.6 ± 81.0 nm diameter formed. Similar nanofiber morphology (fiber diameter of 172.0 ± 46.1 nm) with few defects is maintained at 25 wt% 1-propanol concentration. However, when 1-propanol concentration increased to 33 wt%, the nanofiber production rate significantly decreased, which could be due to the rapid evaporation of THF during the electrospinning process that induced a remarkable increase in the 1-propanol concentration and subsequent solution viscosity. In general, compared to Figure 4.2 and Figure 4.3 with toluene-based binary solvent mixtures, Figure 4.4 and Figure 4.5 show that THF-based binary solvent mixtures can significantly enhance the electrospinability for both NEXAR-1.0 and NEXAR-2.0 solutions.

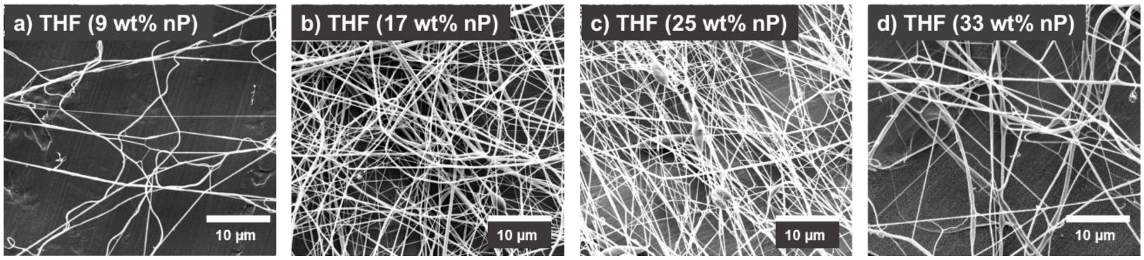

Figure 4.5 Electrospun NEXAR-2.0 in 1-propanol/THF binary solvent mixtures with various 1-propanol concentrations: (a) 9 wt%, (b) 17 wt%, (c) 25 wt%, and (d) 33 wt%.

Figure 4.6 summarizes the average fiber/particle diameter distribution for NEXAR-1.0 and NEXAR-2.0 (SEM images shown from Figure 4.2 to Figure 4.5). In toluene-based solvents (Figure 4.6(a)), the average diameter of electrosprayed NEXAR-1.0 beads (open symbols) decreases exponentially from 10^6 to 10^3 nm when the 1-propanol concentration is increased from 0 wt% to 25 wt%. At the transitional state with a 1-

propanol concentration of *ca.* 25 wt%, electrosprayed beads and electrospun nanofibers coexist. Above 25 wt%, only nanofibers were produced from NEXAR-1.0 solution, compared to a mixture of beads and fibers produced from NEXAR-2.0 solution at the same solvent ratio. However, in THF-based solvents (Figure 4.6(b)), both NEXAR-1.0 and NEXAR-2.0 solutions produce uniform nanofibers with NEXAR-2.0 nanofiber diameters (minimum: 165.7 ± 49.1 nm; maximum: 361.3 ± 91.0 nm) slightly lower than that of NEXAR-1.0 (minimum: 291.5 ± 61.3 nm; maximum: 606.1 ± 120.1 nm). The reduction in fiber diameters for NEXAR-2.0 can be attributed to its higher volume charge densities resulting from higher IEC (*i.e.*, sulfonic acid concentrations), which induces higher electrostatic stretching forces at the Taylor cone during electrospinning.[140] The results in Figure 4.6 demonstrate that electrospun products morphology and dimensions can be strongly influenced by the base solvents (*i.e.*, toluene *vs.* THF).

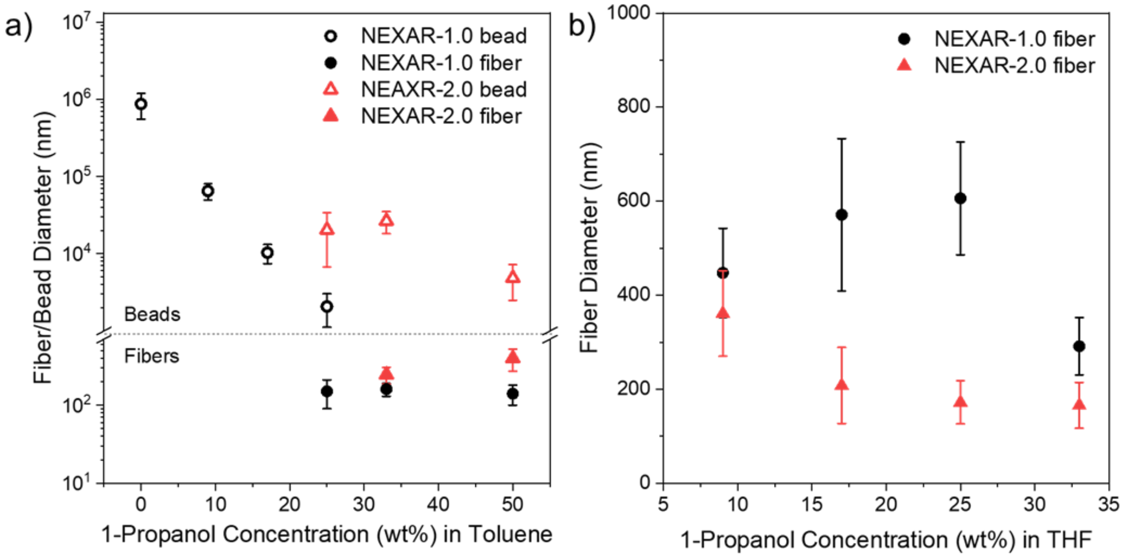

Figure 4.6 Electrospun fiber/bead distribution as a function of 1-propanol concentration for NEXAR-1.0 (black) and NEXAR-2.0 (red) in a) toluene-based and b) THF-based binary solvent mixtures.

4.3.2. Dynamic Light Scattering (DLS)

The DLS measurements were performed to quantitatively investigate dynamic aggregation size distributions in NEXAR® solutions within a broad range from nanometers to microns. Figure 4.7 (a) and (b) are toluene-based solvents for NEXAR-1.0 and NEXAR-2.0, respectively. In Figure 4.7(a), a peak (R_h) of 24.8 nm was observed for NEXAR-1.0 at 5.3 wt% 1-propanol in toluene. With the increase of 1-propanol, the R_h of NEXAR-1.0 gradually reduced to 6.5 nm at 50 wt% 1-propanol (16.9 nm, 13.3 nm, 7.2 nm and 9.0 nm at 9.1 wt%, 16.7 wt%, 25.0 wt%, and 33.3 wt% 1-propanol, respectively). This could be attributed to the increasing amount of 1-propanol that penetrates into the inner sulfonated polystyrene (s-PS) micelle core, which results in a unimer close to a true solution state.[135] Similar decreasing trend in R_h can be observed for NEXAR-2.0 solutions with increasing 1-propanol compositions (Figure 4.7(b)). Note that at 25 wt% 1-propanol (polymer insoluble below 25 wt%), the R_h of NEXAR-2.0 is at 11.8 nm, which is higher than the NEXAR-1.0 counterpart (*i.e.,* 7.2 nm at 25 wt%). This higher R_h of NEXAR-2.0 is a result of higher sulfonation, which reduces its solubility at the lower 1-propanol concentrations.

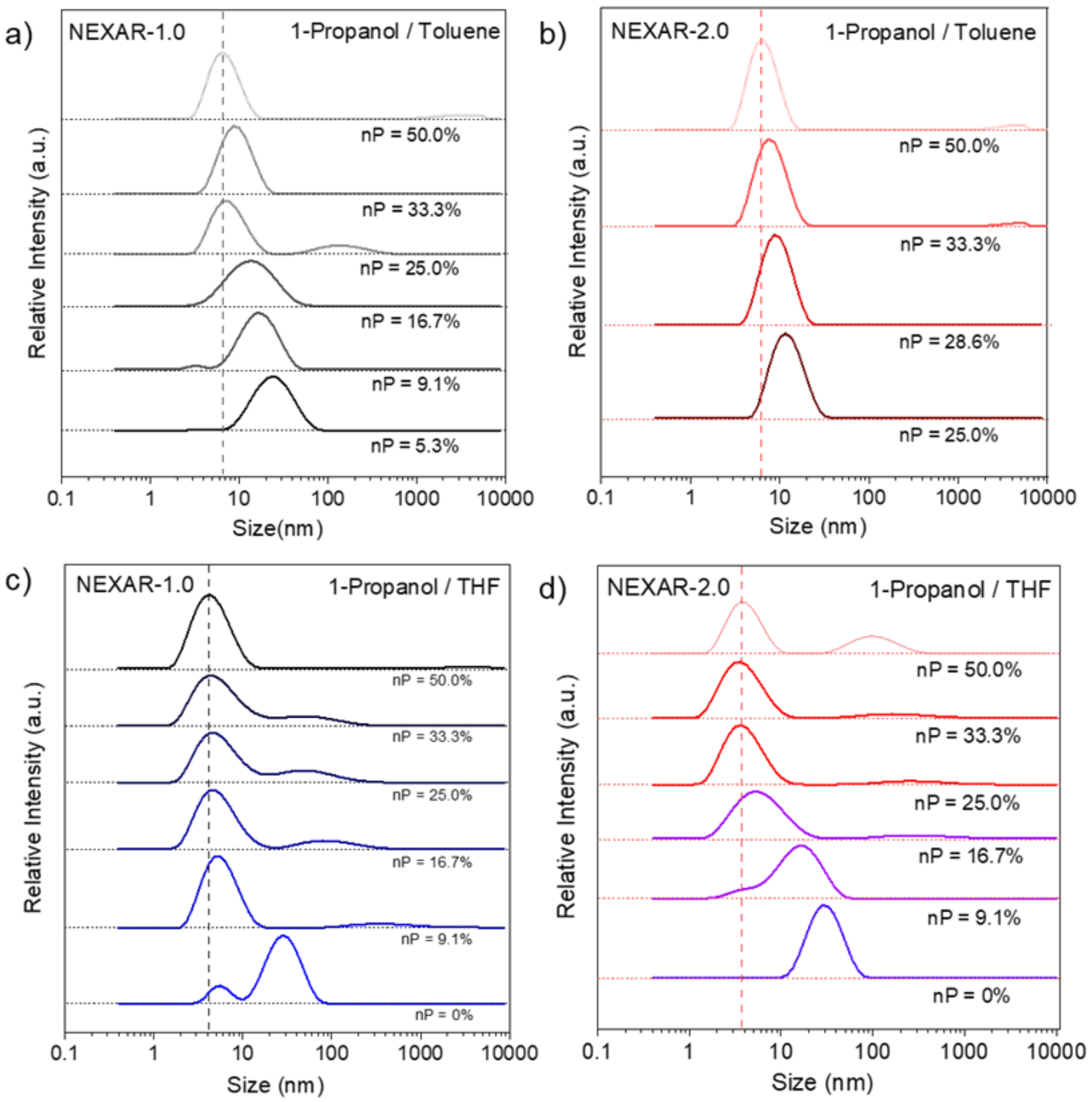

Figure 4.7 Hydrodynamic radius (R_h) size distributions for (a) NEXAR-1.0 in 1-propanol/toluene, (b) NEXAR-2.0 in 1-propanol/toluene, (c) NEXAR-1.0 in 1-propanol/THF, and (d) NEXAR-2.0 in 1-propanol/THF at 1 wt% polymer composition at 25 °C.

Figure 4.7 (c) and (d) show the R_h in THF-based solvents for NEXAR-1.0 and NEXAR-2.0, respectively. In Figure 4.7(c), NEXAR-1.0 exhibits interesting bimodal R_h curve with peaks centered at 5.7 nm and 28.3 nm at 0 wt% of 1-propanol representing both sulfonated core micelles and unimer micelles. With the increase of 1-propanol, the R_h is now prominent for the unimer micelle and gradually decreases from 5.3 nm at 9 wt% to 4.2 nm at 50 wt%, similar to the trend in Figure 4.7 (a). However, the R_h in THF-based solvents are lower than the counterparts in toluene-based solvents across the entire concentration range (24.8 nm at 9 wt% and 6.5 nm 50 wt%, Figure 4.7 (a)), suggesting that the intermediate polar THF plays a significant role in enhancing NEXAR-1.0 solubility. In Figure 4.7 (d), NEXAR-2.0 exhibits a R_h of 29.7 nm in pure THF, and gradually decreases to 3.9 nm at 50 wt% 1-propanol. Again, the R_h of NEXAR-2.0 (3.9 nm at 50 wt%) is slightly lower than its counterpart in 1-propanol/toluene (6.4 nm at 50 wt%, Figure 4.7 (b)), which confirms that THF could effectively reduce the solution aggregation sizes for both NEXAR® solutions.

4.3.3. Small Angle X-Ray Scattering (SAXS)

The solution-state SAXS experiments were performed to provide complementary quantitative micelle shape information in addition to DLS. NEXAR® in 1-propanol/toluene are well documented in literature,[132, 135, 137] therefore Figure 4.8 only shows the scattering profiles of NEXAR® in 1-propanol/THF binary solvent mixtures at various compositions. Figure 4.8(a) shows the scattering profiles for NEXAR-1.0 at various 1-propanol ratios in THF. At 0 wt% of 1-propanol, the SAXS profile shows a broad single primary scattering maximum center at *ca.* 0.015 Å^{-1}, suggesting a highly disordered structure with an aggregate spacing ($L^*\sim2\pi/q^*$) of *ca.* 42 nm. At 9 wt% and 17 wt%, slight shifts of the structure factor q to higher values can be observed, which could be related to the increase of aggregation spacings in solution. At higher 1-propanol concentrations (≥ 25 wt%), the scattering profiles show no scattering peaks representing no structure.

Figure 4.8(b) shows the scattering profiles for NEXAR-2.0 at various 1-propanol ratios in THF. In contrast to NEXAR-1.0 solution, which only shows a single broad peak at 0 wt% 1-propanol, two peaks at q* and 2q* (0.015 and 0.03 Å) were observed (q* is the primary scattering peak), indicating structure and periodicity. With further increasing 1-propanol compositions, the solutions show fast decay of scattering features, indicating the disappearance of phase segregation at high 1-propanol compositions similar to NEXAR-1.0 solution. Overall, the SAXS profiles for both NEXAR® solutions demonstrate that the addition of 1-propanol polar solvent can modulate the solution-state aggregation sizes and distribution and drive the solution towards disordered unimer status and enhance the electrospinability, which coincides with the SEM results (Figure 4.4 and Figure 4.5). The results also confirm that NEXAR-2.0 with a higher IEC tend to form stronger aggregation at low 1-propanol concentration, which agrees favorably with DLS results.

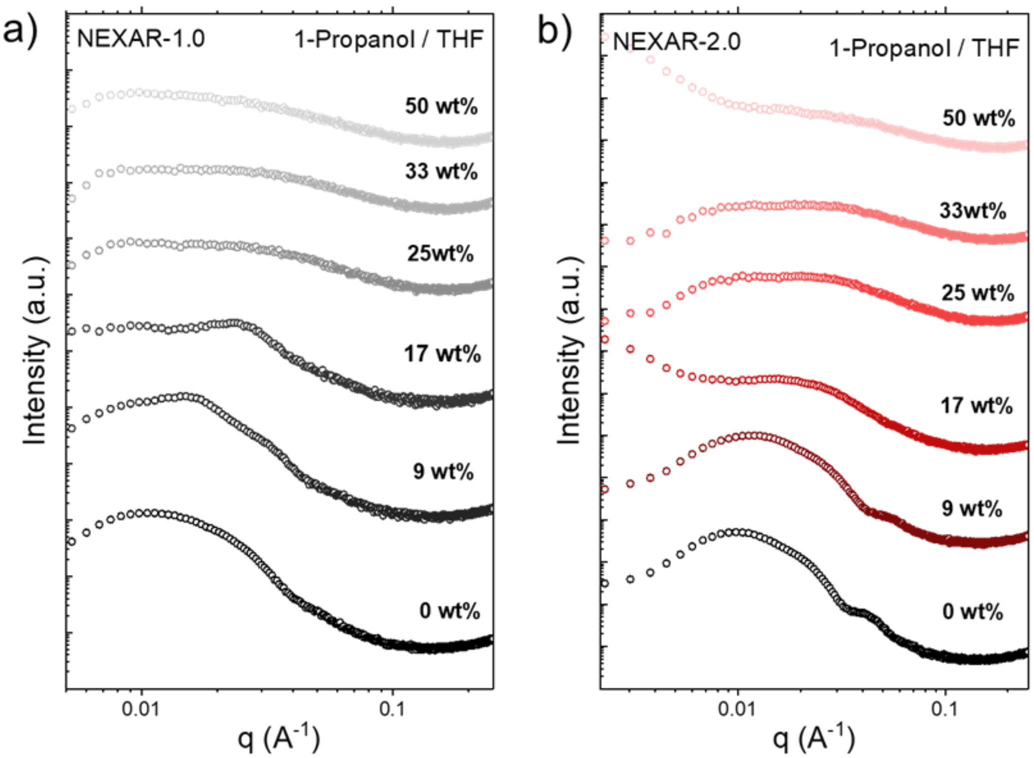

Figure 4.8 Small-angle X-ray scattering (SAXS) profiles of (a) NEXAR-1.0 and (b) NEXAR-2.0 in 1-propanol/THF binary solvent mixtures with various 1-propanol concentrations.

4.3.4. Solubility

Table 4.1 lists selected physical properties (*i.e.*, boiling points T_b, viscosity η, dielectric constant ε, and surface tension γ) of toluene, THF, and 1-propanol. For base solvents, toluene exhibits lower dielectric constant, but higher viscosity than THF, suggesting a tendency to experience less electrostatic drawing force, but more viscoelastic force in the electric field, resulting in a higher possibility of polymer jet breakage and bead formation. As the tuning solvent, 1-propanol has a significantly higher viscosity and dielectric constant, but lower surface tension than both base solvents, which acts as an effective polarity modulator for the solvent blends.

Table 4.1 Physical Properties of Solvents[141]

solvent	T_b (°C)	η^a (cp)	ε^b	γ^c (dyn/cm)
toluene	110.6	0.56	2.38	28.5
THF	66	0.48	7.58	26.4
1-propanol	97	2.26	20.1	23.7

[a] Viscosity
[b] Dielectric constant at 20 °C
[c] Surface tension at 20 °C

To quantify the interaction between the polymer block and solvent, Table 4.2 lists the Hansen solubility parameters (HSPs)[142] (*i.e.*, the energy from dispersion bonds, dipolar intermolecular forces, and hydrogen bonds of δ_D, δ_P, and δ_H, respectively) for the neat solvents and each polymer block (*i.e.*, t-BS, HI, s-PS with 29 mol% and 52 mol% sulfonation) in the NEXAR®. Details of calculation can be found in reference by Griffin *et al.*[137]. Note that the effective HSPs for solvent mixtures were calculated using the tabulated neat values and applying a rule of mixtures.

Table 4.2 Hansen solubility parameters of the neat solvents and constituent polymer blocks.[137]

solvents/polymer blocks	δ_D (MPa$^{1/2}$)	δ_P (MPa$^{1/2}$)	δ_H (MPa$^{1/2}$)
toluene	18.0	1.4	2.0
THF	16.8	5.7	5.7
1-propanol	16.0	6.8	17.4
poly (tert-butyl-styrene) (t-BS)	17.3	1.8	1.7
poly (hydrogenated isoprene) (HI)	16.2	1.1	2.1
sulfonated polystyrene (s-PS) 29 mol%	21.6	15.8	22
sulfonated polystyrene (s-PS) 52 mol%	20.2	9.1	13.1

Figure 4.9 depicts the interaction distance R_a of a specific block (*i.e.*, t-BS, HI, s-PS with sulfonation degree of 29 mol% and 52 mol%) in NEXAR® at specific binary solvent compositions. The interaction distance R_a between two components in a mixture ($R_a = \sqrt{4(\delta_{D1} - \delta_{D2})^2 + (\delta_{P1} - \delta_{P2})^2 + (\delta_{H1} - \delta_{H2})^2}$) empirically quantifies their miscibility according to Hansen's framework[142] (*i.e.*, R_a is negatively proportional to the miscibility), which is calculated based on tabulated parameters in Table 4.2. As shown in Figure 4.9, the t-BS and HI block show overlapping R due to similar solubilities, suggesting that the major difference of solubility for NEXAR-1.0 and NEXAR-2.0 lies in the s-PS block. In Figure 4.9(a), s-PS of 29 mol% show shorter interactive distance R_a than that of 52 mol% in the range of 0–50 wt% 1-propanol composition, indicating higher solubility of NEXAR-1.0 consistent with experimental solubility results. In Figure 4.9(b), the intersection points of both s-PS blocks (29 mol% and 52 mol%) with HI/t-BS are at 3

wt% and 31 wt% 1-propanol in THF respectively, which are both lower than that in 1-propanol/toluene blends (*i.e.*, 32 wt% and 52 wt% respectively), suggesting improved solubility for both polymers in THF than toluene at low to intermediate 1-propanol concentrations (0–50 wt%).

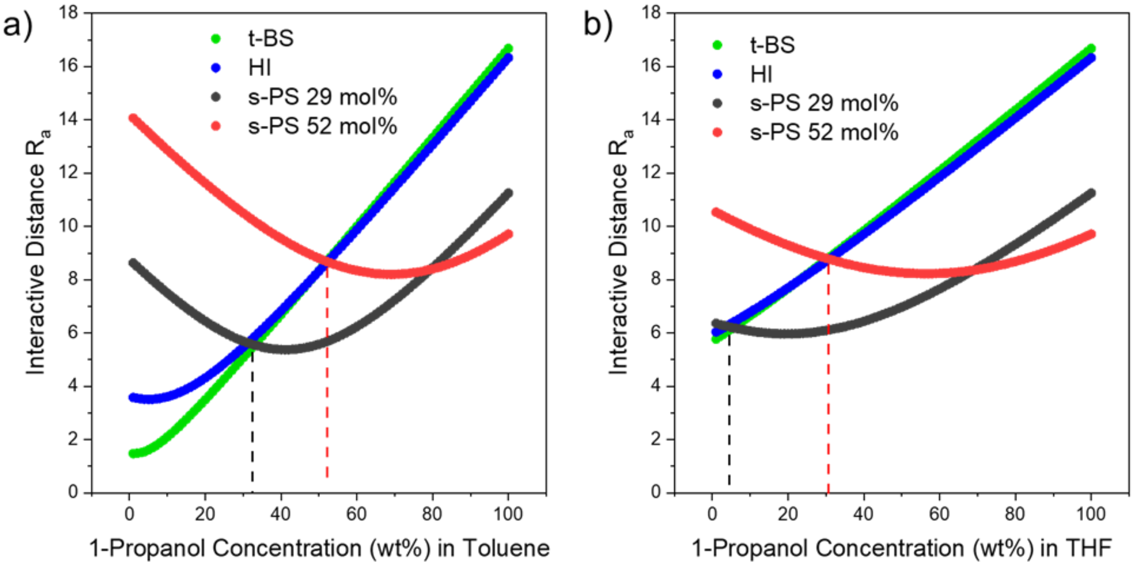

Figure 4.9 Interaction distance R_a calculated for polymer blocks in a) 1-propanol/toluene and b) 1-propanol/THF as a function of 1-propanol composition: t-BS (green), HI (blue), s-PS with 29 mol% sulfonation degree for NEXAR-1.0 (black) and 52 mol% sulfonation degree for NEXAR-2.0 (red). The intersections of s-PS with t-BS/HI are indicated by the dashed lines.

4.3.5. Viscosity

As an important macroscopic property, viscosity can reflect solution micromorphology and greatly influence its electrospinability. High viscosity can cause flow instability and inhibit fiber formation,[118] while low viscosity suggests insufficient chain entanglements and usually results in only droplets rather than fibers. Figure 4.10 (a) shows the solution viscosity for NEXAR-1.0 and NEXAR-2.0 in 1-propanol/toluene binary solvent mixtures as a function of 1-propanol concentration. When NEXAR-1.0 is dissolved in pure toluene, a strong tendency for micellization (*i.e.*, s-PS core and t-BS/HI corona) occurs. As 1-propanol concentration increased from 0 to 10 wt%, 1-propanol starts penetrating the hydrophilic s-PS core, allowing for increased chain interaction, and subsequently increased zero shear rate viscosity (η_0) (*i.e.*, 303 cP for 0 wt% and 585 cP for 10 wt%). However, with a further increase of 1-propanol from 10 to 25 wt%, η_0 shows a slight decrease to 443 cP at 17 wt% followed by a sharp decrease to 79 cP at 25 wt%, suggesting that the solution reaches the critical point where the solvent blends do not have preferential interactions with any block (*i.e.,* isomers) (demonstrated in the intersection point of Figure 4.9(a)). With further increasing 1-propanol composition to 50 wt%, a rapid increase in η_0 was observed (104 cP for 28 wt%, 261 cP for 33 wt%, and 1050 cP for 50 wt%, respectively). The increase in η_0 is attributed to the decreased solubility of nonpolar t-BS/HI blocks. NEXAR-2.0 solution exhibits 30 times higher η_0 (2478 cP) than NEXAR-1.0 (79 cP) at 25 wt% 1-propanol composition (*i.e.,* the threshold that NEXAR-2.0 solution practically measurable using the viscometer), suggesting a much stronger ionic interaction inside the micelle core due to its higher sulfonation level. Similar to NEXAR-1.0, a higher 1-propanol concentration at 33 wt% induced a drastic η_0 reduction to 200 cP, followed by a remarkable η_0 increase to 602 cP at 50 wt% 1-propanol due to higher immiscibility of t-BS/HI block.

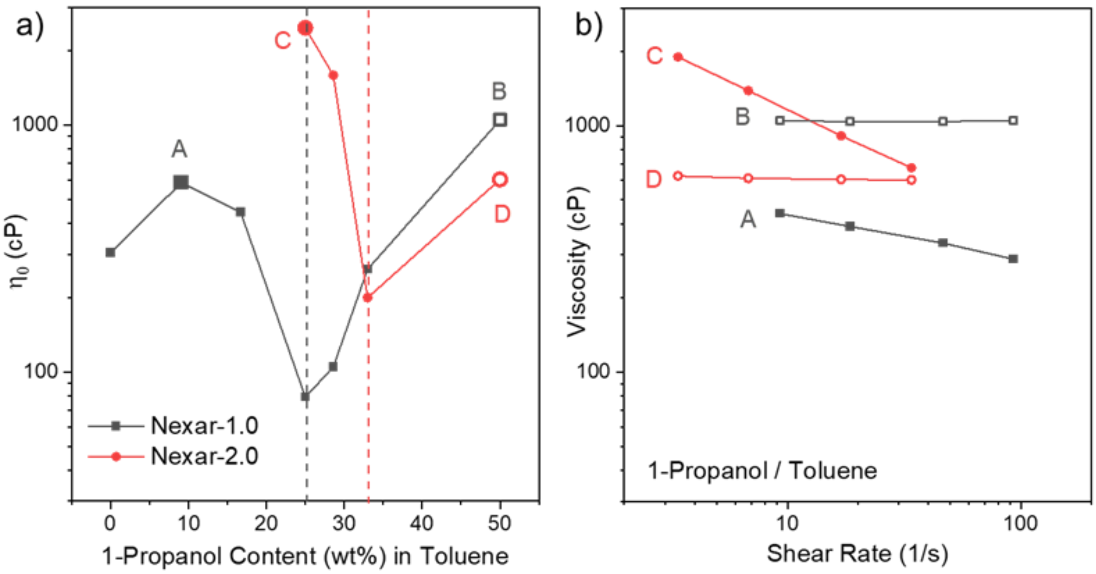

Figure 4.10 (a) Zero shear rate viscosity (η_0) as a function of 1-propanol concentration (wt%) and (b) viscosity (η) as a function of shear rate at composition A (9 wt%) and B (50 wt%) for NEXAR-1.0 (black), and C (25 wt%) and D (50 wt%) for NEXAR-2.0 (red) in 1-propanol/toluene binary solvent mixtures.

Figure 4.10 (b) shows the viscosity as a function of shear rate for NEXAR solutions with low (A, C) and high (B, D) 1-propanol concentrations. For NEXAR-1.0 solution, strong shear-thinning behavior can be observed at 9 wt% 1-propanol (*i.e.*, composition A, η_0 of 585 cP), whereas no shear-thinning was observed at 50 wt% 1-propanol (*i.e.*, composition B, η_0 of 1050 cP). Similarly, Nexar-2.0 solution shows strong shear-thinning behavior at 25 wt% 1-propanol (*i.e.*, composition C, η_0 of 2440 cP) whereas no shear-thinning was observed at 50 wt% (*i.e.*, composition D, η_0 of 603 cP), indicating a breakage of micellar structures.

In addition to toluene (nonpolar solvent), η_0 as a function of 1-propanol content in THF (intermediate polar solvent, uncommon solvent for NEXAR® in literature) was also investigated and shown in Figure 4.11(a). For NEXAR-1.0, η_0 remains relatively constant at low 1-propanol concentration (*i.e.*, 112 cP for 0 wt%, 133 cP for 9 wt%, and 152 cP for 17 wt% 1-propanol, respectively). A drastic increase in η_0 can be observed after 17 wt% 1-propanol (16573 cP for 33 wt%, and 267192 cP for 50 wt%, respectively). This is different from the 1-propanol/toluene binary solvents (Figure 4.10 (a)), where η_0 initially decreased to a critical point and then increased by an order of magnitude. For NEXAR-2.0, the trend in η_0 change is more moderate than the sharp trend in 1-propanol/toluene. The plateau of η_0 from 17 wt% (152 cP) to 33 wt% (270 cP) 1-propanol content indicates that 1-propanol/THF solvent system allows for a transitional conformation in a wider solvent composition range, *i.e.*, more flexible tunability.

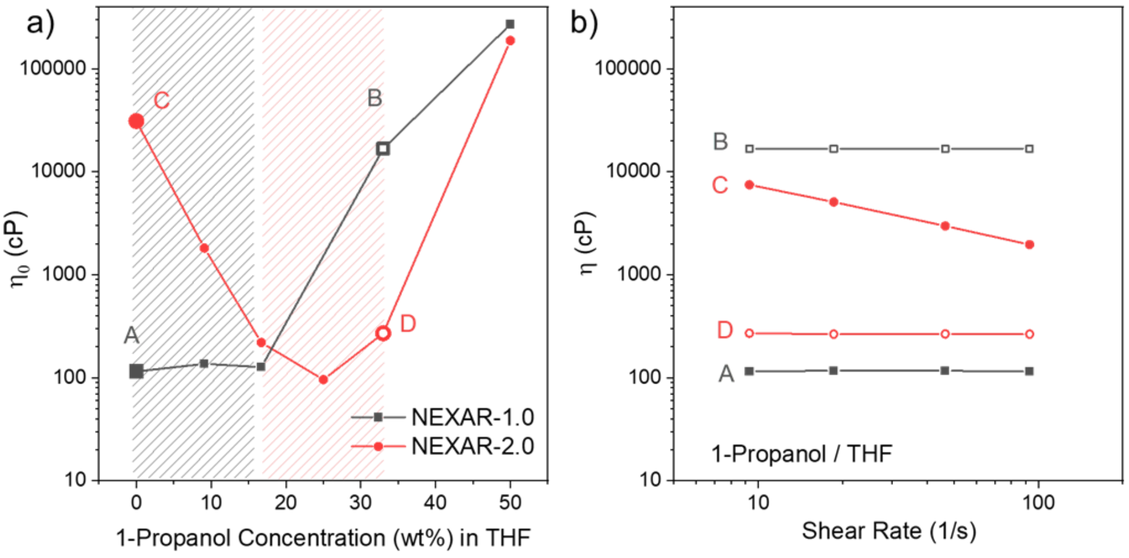

Figure 4.11 (a) Zero shear rate viscosity η_0 as a function of 1-propanol concentration (wt%) and (b) viscosity η as a function of shear-rate at A (0 wt%), B (33 wt%), C (0 wt%), D (33 wt%) for NEXAR-1.0 and NEXAR-2.0 in THF.

In Figure 4.11(b), NEXAR-1.0 at 0 wt% 1-propanol (*i.e.*, composition A, η_0 of 117 cP) does not show shear-thinning behavior, indicating no apparent micellar conformation in pure THF. In contrast, NEXAR-2.0 at 0 wt% 1-propanol (*i.e.*, composition C, η_0 of 30960 cP) still showed shear-thinning in pure THF. Above the minimum η_0 composition (*i.e.*, 17 wt% and 25 wt% 1-propanol for NEXAR-1.0 and NEXAR-2.0, respectively), no shear-thinning can be observed as expected (*i.e.*, η_0 16573 cP for composition B, and η_0 259 cP for composition D).

Similar to solution viscosity, surface tension of the polymer solution is another macroscopic property which also indicates the polymer chain conformation, directly affects the polymer jet formation, since the electrostatic forces in electric field must overcome the surface tension of the solution to form a polymer jet. [118, 143] As an example, at 33 wt% 1-propanol, It can be seen that toluene based binary solutions (*ca.* 27 dyn cm^{-1}) have much higher surface tension than THF based solution system (*ca.* 14 dyn cm^{-1}), which may hinder the proper spinning. The decrease of surface tension is contributing to the increase spinnability.[144]

Table 4.2 Surface Tension of NEXAR Solutions (dyn/cm)

Polymer	Toluene (25wt% 1-propanol)	Toluene (33wt% 1-propanol)	Pure THF	THF (9wt% 1-propanol)	THF (33wt% 1-propanol)
NEXAR-1.0	27.78	26.92	12.99	27.97	14.6
NEXAR-2.0	25.39	27.18	24.98	27.48	11.2

4.3.6. Conductivity

The ionic conductivities of NEXAR solutions were measured as a function of 1-propanol composition in 1-propanol/toluene(Figure 4.12 (a)) and 1-propanol/THF binary solvent mixtures (Figure 4.12(b)). At low 1-propanol concentrations in toluene (0–28 wt%, Figure 4.12(a)), the conductivities of both NEXAR-1.0 and NEXAR-2.0 solutions remain less than 10 µS cm^{-1}. However, in 1-propanol/THF(Figure 4.12(b)), the conductivity increases drastically for NEXAR solutions starting from 0 wt% 1-propanol. From the material standpoint, NEXAR-2.0 exhibits significantly higher conductivity than the NEXAR-1.0 counterparts due to its higher sulfonation level (52 mol% *vs.* 29 mol%). From the solvent standpoint, high conductivities in THF-based solvent can be attributed to the stronger ability of THF to disassociate the protons from the sulfonated groups (evidenced by the higher dielectric constant in Table 4.1). The high conductivity resulting from ion dissociation has both benefits and risks during electrospinning. Sufficient conductivity in a reasonable range can increase the electrostatic driving force and facilitate the Taylor cone formation and fiber initiation. However, when the conductivity reaches beyond a critical value, an overly strong electrostatic force is generated and breaks its balance with the viscoelastic force. As a result, the needle and the conductive collector will be short-circuited and produce no fibers.[127]

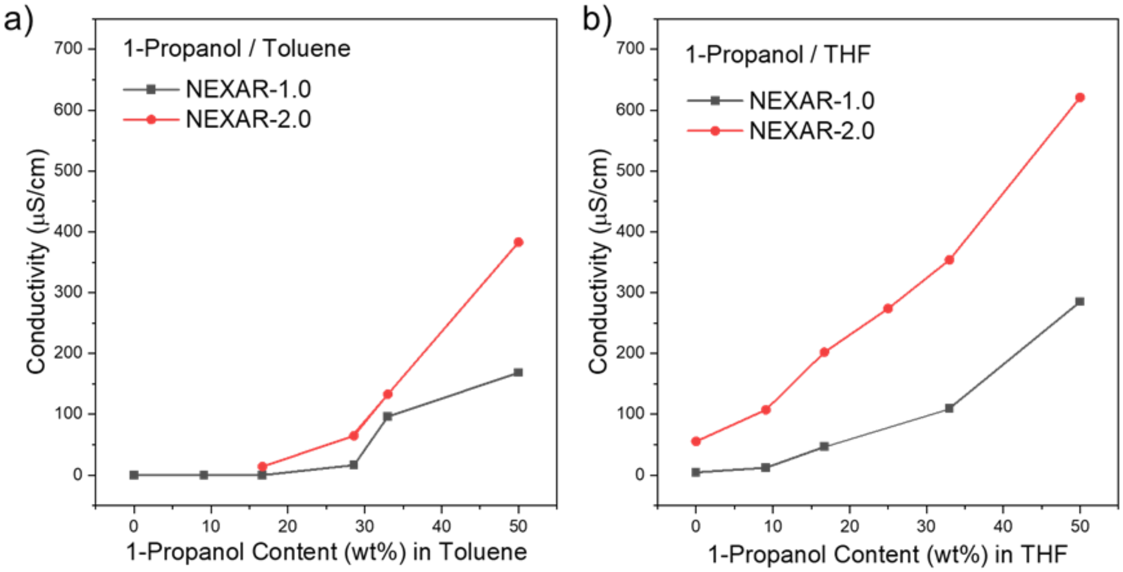

Figure 4.12 Solution conductivity of NEXAR-1.0 (black) and NEXAR-2.0 (red) as a function of 1-propanol concentration from 0–50 wt% in (a) toluene and b) THF.

Figure 4.13 summarized the solution viscosity, conductivity, and resulting electrospinning morphologies for NEXAR-1.0 and NEXAR -2.0 in 1-propanol/toluene and 1-propanol/THF binary solvent mixtures, where the relative magnitude of viscosities and conductivities act as a practical guide for solvents modulation in the multiblock polymer solutions. Generally, due to the monotonic increasing trend of conductivities and non-monotonic parabolic trend of viscosities (except for Figure 4.13 (c)), an optimum 1-propanol concentration exists, where the viscoelastic forces balance with the electrostatic forces. Compared to the 1-propanol/toluene (Figure 4.13 (a) and (b), *ca.* 10^2–10^3 cP and 0–400 µS cm^{-1} for viscosity and conductivity, respectively), both viscosities and conductivities span over a broader range in 1-propanol/THF (Figure 4.13 (c) and (d), *ca.* 10^2–10^6 cP and 0–600 µS cm^{-1} for viscosity and conductivity, respectively), suggesting 1-propanol/THF could offer more flexibility in tuning solution properties for electrospinning.

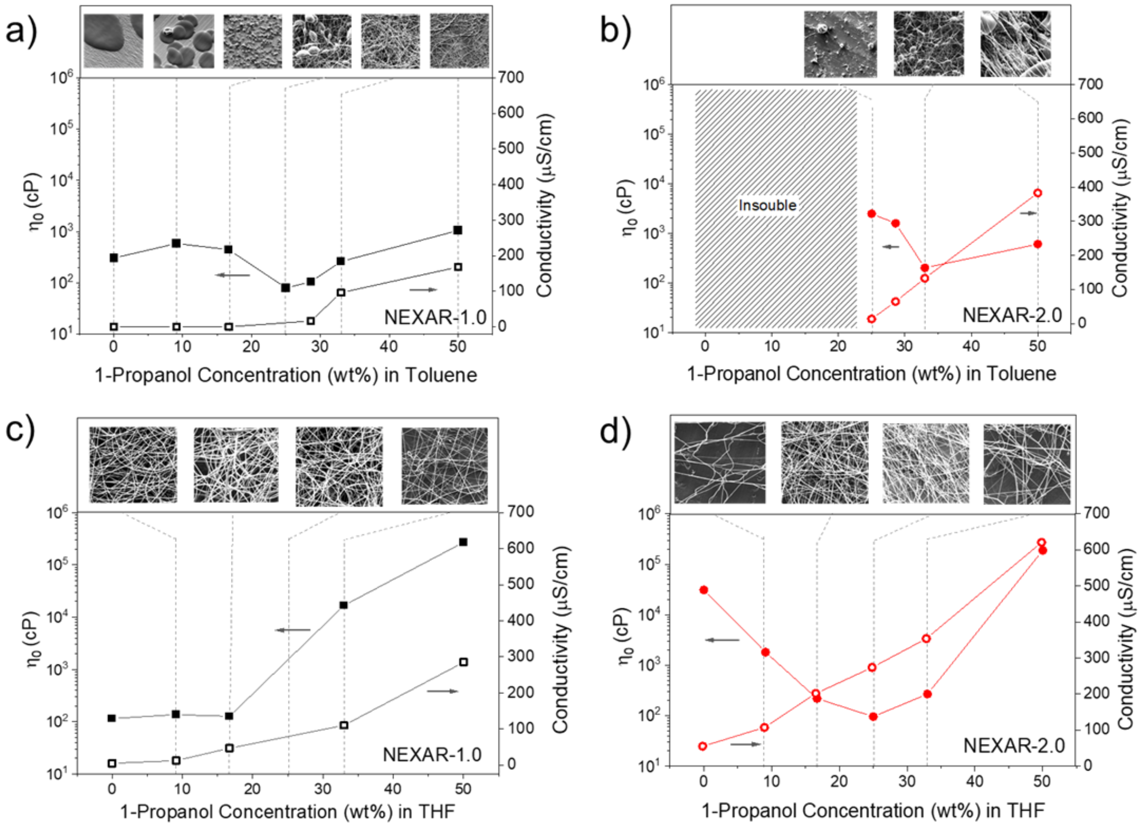

Figure 4.13 Solution viscosity, conductivity and corresponding electrospun products morphologies as a function of 1-propanol concentration (wt%) in (a) toluene for NEXAR-1.0, (b) toluene for NEXAR-2.0, (c) THF for NEXAR-1.0, and (d) THF for NEXAR-2.0.

4.4. Conclusions

In this work, solvent influence on the solution properties and electrospinning of sulfonated pentablock terpolymer NEXAR® was systematically investigated. Polymers with two IECs (1.0 and 2.0 meq g^{-1} for NEXAR-1.0 and NEXAR-2.0, respectively) in two binary solvent mixtures (1-propanol/toluene and /1-propanol/THF) were explored. It was found that 1-propanol concentration (ranging 0–50 wt%) can greatly modify the interaction between the solvents and the different block chemistries. Therefore, the solution microstructures can be modulated, *i.e.*, aggregated micelle sizes, as characterized by DLS and SAXS. Such microstructural properties can be reflected in macro properties, *i.e.*, viscosity, shear-thinning behavior, and conductivity. The combining effect of both micro- and macro-properties can play a significant role in the solution electrospinability, resulting in a series of evolving electrospun morphologies (*i.e.*, beads, beaded fibers, and uniform fibers). In addition, compared with toluene (nonpolar), THF (intermediate-polar) demonstrated stronger electrospinability and broader tunability regarding NEXAR® electrospinning. This phenomenon can be attributed to a more neutral conformation of the multiblock polymer chains in stronger polar solvents. In addition, the IEC of NEXAR® also greatly influence the electrospinning due to varying sulfonation group concentration. Overall, this study provides insights into sulfonated pentablock terpolymer nanofibers electrospinning behavior through systematically modulating the solvent mixture composition, which facilitates future applications of pure electrospun sulfonated pentablock terpolymer nanofibers in electrochemical devices, such as PEM fuel cells.

CHAPTER 5.

LITHIUM ION CONDUCTING POLY(IONIC LIQUIDS) NANOFIBERS

5.1. Introduction

As mentioned in the overview of the introduction, battery electric vehicles (BEVs) are the leading alternative to internal combustion engine vehicles (ICEVs) in addition to fuel cell electric vehicles (FCEVs). Currently, lithium-ion batteries are the leading battery technology in BEVs. Highly conductive and electrochemically stable solid-state polymer electrolytes (SPEs) can reduce the potential hazards caused by volatile and flammable liquid electrolytes, therefore enabling safe, long-lasting lithium-ion batteries. Poly(ionic liquids) (PILs) are excellent SPE candidates, because they combine the unique physicochemical properties of ionic liquids (ILs) (*e.g.*, electrochemical stability). Therefore, Chapter 5 expands the investigation of electrospinning behavior to PILs, which is beyond proton-conductive polymers discussed previously (*i.e.*, Nafion in Chapter 2 and NEXAR® in Chapter 3 and 4). In addition, the impact of lithium (Li) salts doping on the PIL nanofiber formation, and the physicochemical properties of the resulting fibers are characterized and compared to its bulk film counterpart, targeting potential applications in lithium-ion batteries.

PILs are macromolecules consisting of covalently bonded organic anion/cation and mobile counterions, which are usually weakly coordinated, enabling PILs to possess high anhydrous ionic conductivities in a battery environment.[145, 146] Different from the neutral polymer host (*e.g.*, poly(ethylene oxide) (PEO)), PILs typically possess high dielectric constant[147] ($\varepsilon \approx 5$ for PEO and $10 < \varepsilon < 15$ for PILs) and extraordinary electrochemical stability windows (ESW, usually < 4 V for PEO,[148] and up to 5 V for PIL)[149]. Besides its intrinsic advantages, PIL also demonstrates rich versatile in chemistry, and good compatibility with other chemistries to derive binary or ternary mixtures with external dopants such as Li salts[150-152] or ILs[153-155] due to electrostatic interactions.

The utilization of PILs in lithium-ion batteries requires the addition (or doping) of Li salts, *i.e.,* the introduction of a mobile lithium cation in the system.[156] To date, only a few papers have investigated the salt-doped PIL bulk properties[157-159], and even less understanding of such topic under morphological restrictions[160] (*i.e.,* 2D-confined nanofibers *versus* bulk membrane) for PIL nanofibers. The reason for the limited research on salt-doped PIL nanofiber lies in the challenges of fabrication pure or salt-doped PIL nanofibers. One of the earliest studies by Chen *et al.*[130] demonstrated pure PIL electrospinning properties and observed high ionic conductivities of the ionic liquid doped fibers. However, no salt-doping properties was explored in this study. Most of other PIL-based nanofiber studies focus on non-electrochemical topics, such as solution properties[127], carbonized fibers[161-163], pressure sensing fabrics[164], and air filters[165]. Also, note that the PIL fibers in these studies are not pure (*i.e.,* typically mixed with *ca.* 30–60 wt% of carrier polymers such as polyacrylonitrile (PAN)), which makes the elucidation of intrinsic PIL nanofiber properties difficult. To our best knowledge, no systematic research investigating ion transport properties within pure and Li salt-doped PIL nanofibers is available.

Despite the challenges in PIL nanofiber fabrication, the motivation of investigating PIL nanofiber morphological restrictions are well-justified by similar topics in neutral polymer nanofibers, where significant influences of structural confinements on molecular orientation[166], chain spacing[167], and the resulting thermal[168], mechanical[169, 170], and electrochemical[171, 172] properties were observed. For instance, electrospun PEO nanofibers can decrease crystalline regions and increase free Li^+ ratio compared to solution-cast counterparts.[173-176] However, for PIL homopolymer nanofibers, which are usually amorphous, unresolved questions remain: how are the ionic conductivities and other physicochemical properties influenced by the size confinement inside the nanofibers? Would Li salt doping in PIL nanofibers influence the conductivities in a similar fashion compared to its solution-cast film counterpart? It is reasonable to hypothesize that electrospinning can modify chain orientation, backbone–backbone spacing, and segmental motions through the polymer jet drawing process, thus leading to different ion-conducting behavior. Supporting evidence can be found in studies[177, 178], which correlated increasing (three-fold) backbone-to-backbone distance to decreasing (an order of magnitude) T_g-independent ionic conductivity in an amorphous PIL homopolymer.

In order to answer these questions, this study chose poly(VBBIm-BF_4) (VBBIm-BF_4 $\equiv$ vinylbenzyl butylimidazolium tetrafluoroborate) as a model system to explore the neat and Li salt doped electrospun PIL nanofiber properties and compare it with the solution-cast film bulk properties (Figure 5.1). In order to test the hypothesis of size confinement effect in nanofibers, we characterized the macroscopic physicochemical properties, such as glass transition temperature (T_g), degradation temperature (T_d), and ionic conductivities in electrospun PIL nanofibers.

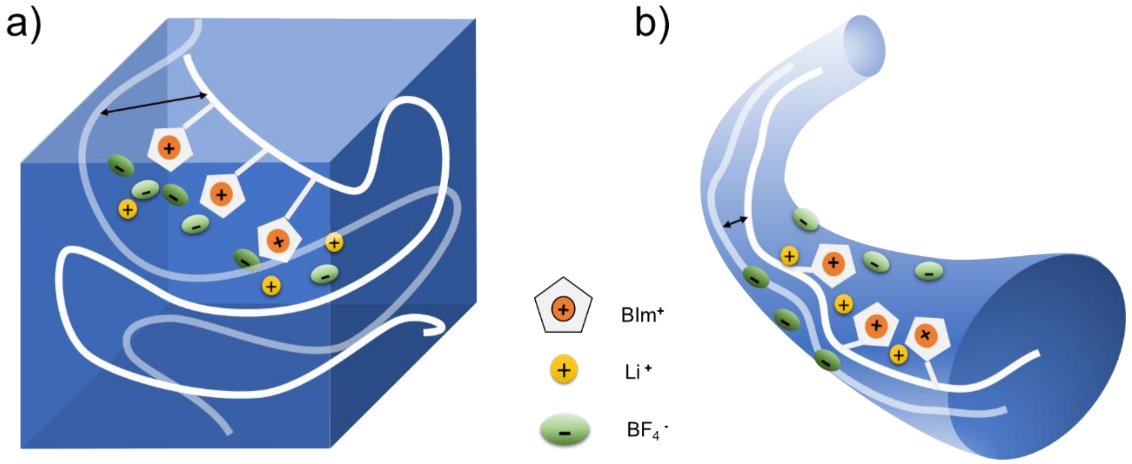

Figure 5.1 Illustration of lithium salt-doped PIL binary system configuration in (a) bulk properties and (b) confined within nanofiber, with the black arrows indicative of the polymer backbone to backbone spacing.

5.2. Experimental Methods

5.2.1. Materials

Poly(vinylbenzyl chloride) (poly(VBC)) (60/40 mixture of 3- and 4-isomers, $M_n \approx 55.0$ kg mol^{-1}, $M_w \approx 100$ kg mol^{-1}, by gel permeation chromatography (GPC)/multiple angle laser light scattering), methanol (anhydrous, 99.8%), acetonitrile (anhydrous, 99.8%), *N*,*N*-dimethylformamide (DMF) (ACS reagent, $\geqslant$99.8%), 1-butylimidazole (98%), acetone (ACS reagent, $\geqslant$99.5%), dimethyl sulfoxide-d_6 (DMSO-d_6) (99.9 at% D; contains 0.03% v/v tetramethylsilane), tetrafluoroborate lithium salt ($LiBF_4$) (98+%) were purchased from Sigma-Aldrich (Milwaukee, WI, USA) and used as received without further purification. Deionized (DI) water with resistivity *ca.* 16 MΩ cm was used as appropriate.

5.2.2. Synthesis of Poly (VBBIm-BF_4)

The synthesis of poly(VBBIm-BF_4) (VBBIm ≡ vinylbenzyl butylimidazolium) was performed according to a procedure in literature[150, 179, 180], by the functionalization of the non-ionic polymer precursor poly(VBC) (step 1 of Figure 5.2) followed by anion exchange (step 2 of Figure 5.2). As an example reaction, 7.0005 g (45.75 mmol) of poly(VBC) was dissolved in 55 mL DMF in a 250 mL flask. 11.36 g (91.48 mmol) of 1-butylimidazole (VBC/1-butylimidazole = 1/2 mol/mol) was added dropwise into the flask. The reaction was performed at 80 °C for 48 h. The resulting polymer was precipitated in acetone, isolated by centrifuge (Eppendorf 5804, at 8500 rcf for 10 min), and subsequently washed in acetone multiple times. The solid polymer was dried under vacuum in an oven at room temperature for at least 24 h, yielding 11.4919 g (41.49 mmol) light yellow solid particles (90.69%). Subsequently, anion exchange was performed to exchange the poly(VBBIm-Cl) from Cl^- to BF_4^- form (step 2 of Figure 5.2). As an example reaction, 11.7002 g (124.5 mmol) of $LiBF_4$ was stirred in 100 mL of DI water and added dropwise into 11.0010 g (39.71 mmol) of poly(VBBIm-Cl) aqueous solution (VBBIm-Cl/$LiBF_4$ = 1/3 mol/mol). The reaction was performed at room temperature for 48 h. The resulting precipitated polymer was separated by centrifuge, followed by extensive washing with DI water for 72 h to remove the residual Cl^- and $LiBF_4$. The anion exchanged polymer, poly(VBBIm-BF_4), was then filtered and dried under vacuum in an oven at room temperature for 24 h. Yield: 12.0120 g (36.62 mmol) of solid particles (92.22%). ^{1}H NMR (400 MHz, DMSO-d_6, 23°C) δ (ppm): 9.30–9.00 (s, 1H, N–C*H*=N), 7.88–7.59 (s, 2H, N–C*H*=C*H*–N), 7.57–6.01 (m, 4H, $\mathrm{C_6}H_4$), 5.41–4.79 (m, 2H, $\mathrm{C_6H_4{-}C}H_2\mathrm{{-}N}$), 4.39–3.86 (s, 2H, $\mathrm{N{-}C}H_2\mathrm{{-}CH_2{-}CH_2{-}CH_3}$), 1.83–1.56 (m, 3H, $\mathrm{CH_2{-}C}H$, $\mathrm{N{-}CH_2{-}C}H_2\mathrm{{-}CH_2{-}CH_3}$), 1.56–0.93 (m, 4H, $\mathrm{C}H_2\mathrm{{-}CH}$, $\mathrm{N{-}CH_2{-}CH_2{-}C}H_2\mathrm{{-}CH_3}$), 0.93–0.58 (s, 3H, $\mathrm{N{-}CH_2{-}CH_2{-}CH_2{-}CH_3}$) (NMR, Figure 5.2). Elemental analysis calculated: C, 58.54; H, 6.40; N, 8.54; Cl, 0.00; F, 23.17. Found: C, 58.48; H, 6.77; N, 8.35; Cl, 0.00; F, 22.83.

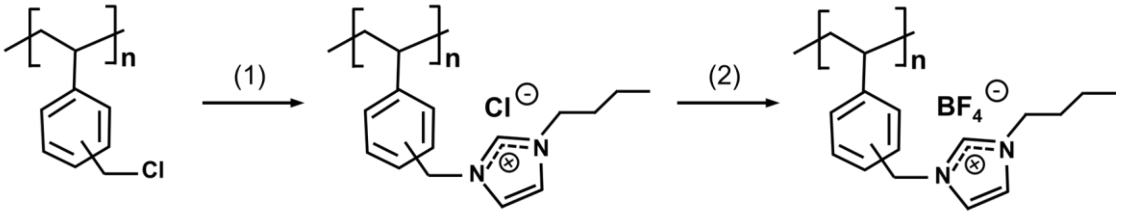

Figure 5.2 Synthesis of poly(VBBIm-BF_4). (1) 1-butylimidazole, DMF, 80 °C, 48 h; (2) $LiBF_4$, H_2O, room temperature, 48 h.

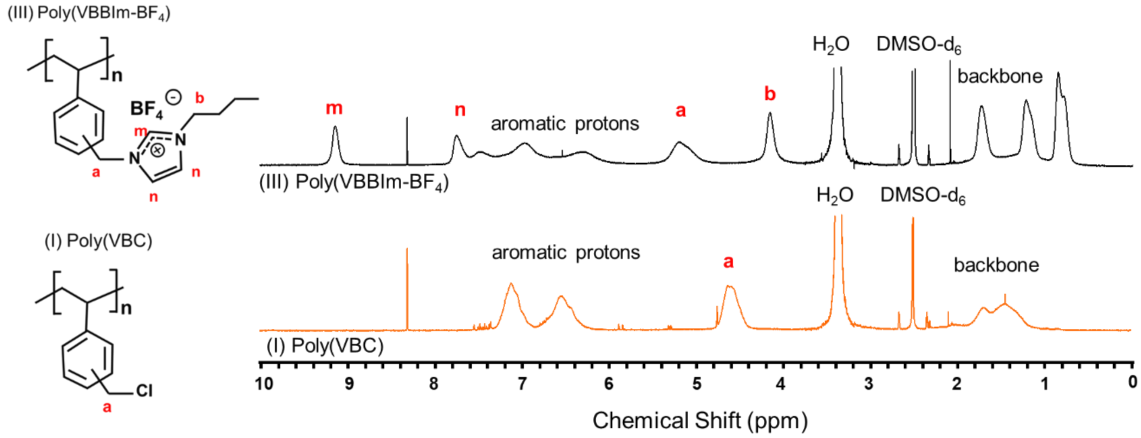

Figure 5.3 ^{1}H NMR spectra and peak assignments of (I) poly(VBC), and (III) poly(VBBIm-BF_4).

5.2.3. Film and Fiber Preparation

For the preparation of neat and salt-doped poly(VBBIm-BF_4) films and electrospun fibers, the homopolymer poly(VBBIm-BF_4) were first dissolved in 3/1 acetonitrile/DMF (w/w) binary solvents at 20 wt% and 30 wt% solid concentration for the use of solution casting and electrospinning, respectively. The lithium salt ($LiBF_4$) was added to the mixture to obtain the desired salt concentration and thoroughly stirred for at least 12 h at ambient temperature to ensure complete dissolution before use. The desired molar ratio was determined by the ratio of lithium ions to poly(VBBIm-BF_4) moieties (r = [Li^+]/[VBBIm-BF_4]).

Due to the brittleness of the poly(VBBIm-BF_4) films, the mixture solutions were cast directly onto the stainless steel spacers (thickness of *ca.* 1020 mm) using an automatic film applicator (Elcometer 4340) with a doctor blade at a gauge height and speed of *ca.* 2000 µm and 60 mm s^{-1}, respectively. The polymer/salt solution-coated spacers were partially covered to allow solvent evaporation for 6 h under ambient conditions and then further dried under vacuum for 24 h.

The electrospinning apparatus used in this study is illustrated and described in Chapter 4 (Figure 4.1). All electrospinning experiments were performed at room temperature (*ca.* 24 °C) and at the humidity below 20% RH, which was maintained by supplying dry air to the enclosed electrospinning chamber. Steady polymer jets were obtained at electrospinning voltage of 25–30 kV, an electrospinning distance of 9 cm, and a flow rate of 0.3–0.6 ml/h. Four stainless steel spacers were attached uniformly to the aluminum foil covered on the rotating drum collector to enable the direct deposition of the electrospun fibers. After electrospinning, the electrospun fibers were dried under vacuum for 24 h and then stored in an argon-filled glovebox before use.

5.2.4. Characterization

Chemical analyses were performed with ^{1}H NMR spectroscopy (Bruker Avance NEO 400 MHz spectrometer) at 23 °C with various NMR solvents. ^{1}H NMR spectrum of poly(VBC), poly(VBBIm-Cl), and poly(VBBIm-BF_4) were collected referenced to DMSO-d_6 at 2.50 ppm. EA experiments were performed by Atlantic Microlab Inc. in Norcross, GA, USA. Infrared spectroscopy was performed at room temperature with a Fourier transform infrared spectrometer (Nicolet 6700 Series; Thermo Electron Corporation) using a single reflection diamond attenuated total reflectance (ATR) accessory (Specac; Quest). All infrared spectra were collected using a liquid-nitrogen-cooled mercury-cadmium-telluride (MCT) detector at 32 scans per spectrum with a resolution of 4 and data spacing of 1.928 cm^{-1}. The spectra were corrected with a background subtraction of the spectrum of the bare ATR crystal.

Differential scanning calorimetry (DSC; Q200, TA Instruments) experiments were performed to determine the glass transition temperatures (T_gs). The measurements were collected under a nitrogen environment (50 mL min^{-1}) using the method of heat/cool/heat at a heating/cooling rate of 10 °C min^{-1} over the temperature range from -140 to 180 °C. The T_g values were determined using the midpoint method on the second heating cycle thermogram. TGA (Q50, TA Instruments) experiments were performed to determine the thermal degradation temperatures (T_ds). The measurements were collected under a nitrogen environment (60 mL min^{-1}) at a heating rate of 10 °C min^{-1} over the temperature range 25–900 °C. The T_d values were determined at 5 wt% loss using TA Universal Analysis software.

Films and fiber mats thicknesses were measured with a digital micrometer (Mitutoyo; ±0.001 mm accuracy) by calculating the thickness differences of the spacers before and after solution-casting or electrospinning deposition. The final film and fiber mat thicknesses for ionic conductivity measurement were *ca.* 80−110 μm. The morphologies of the neat and Li-doped electrospun poly(VBBIm-BF_4) fibers were investigated with SEM (FEI Quanta 600 FE-SEM, 10 kV) using a working distance of 10 mm. Samples were sputter-coated (Cressington 208 HR) with iridium (6 nm thickness) prior to SEM analysis.

Ionic conductivity for both films and fibers were measured with a potentiostat/galvanostat and an impedance analyzer (Gamry 5000E) *via* electrochemical impedance spectroscopy (EIS). Conductivity measurements were performed with symmetric cells with blocking electrodes (stainless steel). A test cell was assembled by combining a spacer-supported sample with another stainless-steel spacer (thickness *ca.* 1.020 cm) and a spring (height *ca.* 0.12 cm) in a CR2032 coin cell. The coin cells were pressed twice using a coin cell crimping machine (MTI Corp., MSK-160D) in a glovebox at room temperature to ensure a proper seal. Impedance scans (Nyquist plots) were measured at the open-circuit potential at 10 mV amplitude over a frequency range from 1

MHz to 0.5 Hz at a temperature range from 50 to 100 °C with 10 °C increments controlled by an environmental chamber (MACCOR, 4200M). Samples were allowed to equilibrate for 1 h at each measurement condition, followed by at least five measurements. The resistance was determined from a high x-intercept of the semicircle regression of the Nyquist plot. Conductivity was calculated using the following equation: $\sigma = L/AR$, where L is the average thickness of film/fiber mat, and A is the area of the stainless-steel spacer ($A = \pi(d/2)^2$, d = 1.55 cm). Note that for porous fibers, conductivity normalization was conducted by replacing A with A' (*i.e.*, the corrected area of fibers only, and the surface porosity was estimated using SEM images by ImageJ software).

5.3. Results and discussion

5.3.1. Chemical Analysis

Functionalization and anion exchange reactions were performed on the non-ionic polymer precursors poly(VBC) following a literature procedure[179, 181] to synthesis the poly(VBBIm-BF_4) (Figure 5.2). Figure 5.3 shows the ^1H NMR spectra of the poly(VBC) precursor and the final PIL homopolymer poly(VBBIm-BF_4), and specific peak assignments are listed in the experimental section. The resulting functionalized polymers, poly(VBBIm-Cl), were found to be hygroscopic and water-soluble. Therefore, water was chosen as the solvent for anion exchange reactions. Peak a shifts from 4.80 to 4.41 ppm in the spectra for poly(VBC) (Figure 5.3 (I)) and from 5.49 to 4.83 ppm in the spectra for poly(VBBIm-BF_4) (Figure 5.3 (III)), indicating the successful functionalization of the neutral polymer precursor. The degree of functionalization was calculated by the integration ratio of CH_2 protons of the butyl chain on the cations (*i.e.*, peak b, 4.41−3.95 ppm) to peak a (5.49 to 4.83 ppm) and the poly(VBBIm-BF_4) was confirmed to be fully functionalized. Furthermore, the efficacy of the anion exchange metathesis was confirmed by EA, where the compositions of the anion exchanged poly(VBBIm-BF_4) closely match the theoretical compositions and the chloride residues were negligibly small, indicating that the anion exchange reactions were successful and highly efficient.

ATR-FTIR spectra (Figure 5.4) further confirmed successful functionalization of PVBC and the following ion exchange. From the PVBC spectrum, the peak at *ca.*1265 cm^{-1}, which is assigned to CH_2Cl wagging vibration[182], disappeared after functionalization. For Poly(VBBIm-Cl), characteristic IR peaks in the ranging 2800–3000 cm^{-1} and 3080–3180 cm^{-1} can be observed, which are originated from the C-H on butyl chain and imidazolium ring, respectively. In addition, the hydrophilic PIL in chloride form exhibit a broad infrared band (O-H stretching band at 3380 cm^{-1}) corresponding to the absorbed water. After ion exchange to the Cl^- to BF_4^- form, the water band is negligible due to the hydrophobicity of the anion. Instead, the characteristic band of BF_4^- at 1046 and 1011 cm^{-1} appeared, which is consistent with literature.[183, 184]

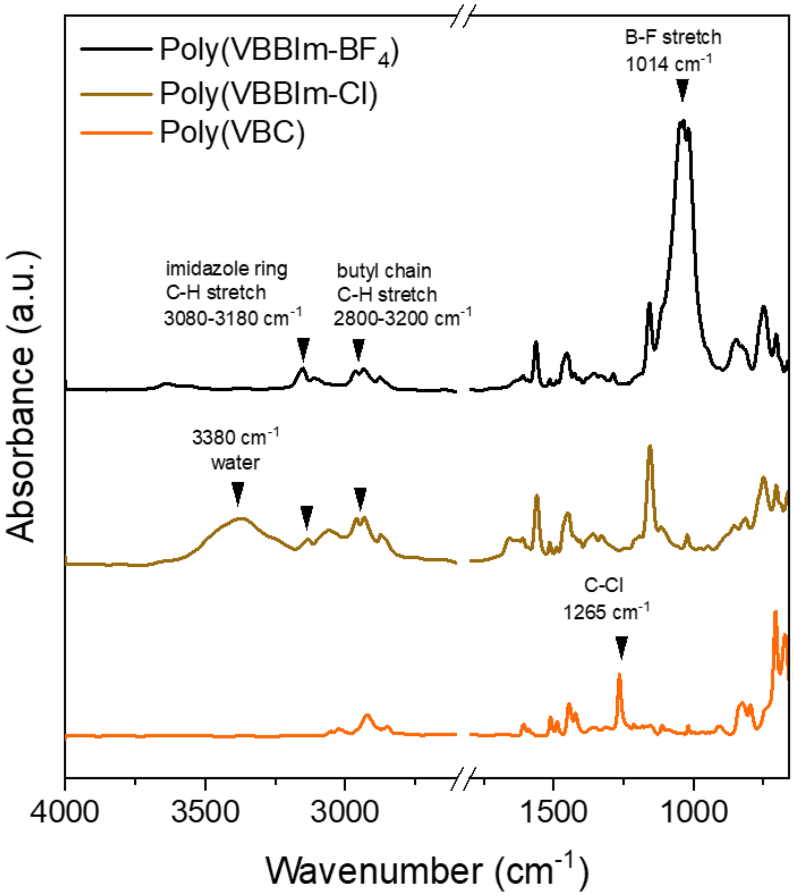

Figure 5.4 ATR-FTIR spectra of poly(VBC), poly(VBBIm-Cl), and poly(VBBIm-BF$_4$).

5.3.2. Electrospun Nanofiber Morphology

Figure 5.5 shows the SEM images of poly(VBBIm-BF$_4$) with varying LiBF$_4$ ratio (r = [Li$^+$]/[BIm$^-$] (mol/mol) = 0, 0.1, 0.2, 0.3, 0.4). To ensure a smooth polymer jet formation and avoid spinneret blockage, 25 wt% of DMF was added as a cosolvent to reduce the volatility of acetonitrile while maintaining similar solubility and dielectric constant.[130] Electrospinning of the neat poly(VBBIm-BF$_4$) (Figure 5.5 (a)) produced uniform nanofibers with a diameter of 281.2 ± 129.9 nm without defects. The increase of

Li salt ratio from 0 to 0.1 (Figure 5.5 (b); 586.2 ± 262.4 nm) and to 0.2 (Figure 5.5 (c); 768.1 ± 303.3 nm) result in slightly higher fiber diameters, while the fiber appearance remained similar. As the Li salt ratio further increased to 0.3, dry-state fiber sizes (Figure 5.4 (d); 567.6 ± 219.9 nm) and morphology do not show significant changes. Interestingly, interconnected branched structures formed after being conditioned at room temperature and humidity (24 ± 2 °C, 45 ± 5 % RH), which increased the standard deviation of the fiber diameter (Figure 5.5 (e); 766.1 ± 434.8 nm). It might be due to the hygroscopic nature of the Li salt. For the 0.4 salt ratio under dry conditions, ribbon-like structures formed (Figure 5.5 (g); 1014.0 ± 468.3 nm). Similarly to 0.3 salt ratio, no individual nanofibers can be identified due to excessive water absorption (Figure 5.5 (h)) after being conditioned (humidified) at room temperature and humidity. It is well-documented in literature[185-187] that the addition of Li salt in neutral polymer solutions could decrease the fiber diameter due to increased electrostatic forces that caused elongation and stretching behavior. However, in polyelectrolytes, the addition of salt would screen the charges, reduce the electrostatic charge repulsion, and shift the polyelectrolyte solution behavior towards uncharged neutral polymer solution.[131] Besides, water-swollen effects also contribute to the fiber diameter increment. Another interesting feature we observed is that salt crystals formed after high salt ration fibers are humidified. For fibers with 0.3 (Figure 5.5 (d)) and 0.4 (Figure 5.5 (g)) salt ratio under dry conditions, no salt crystals were found on the fiber surface. However, after being humidified at room condition, Li salt crystals are clearly visible on the polymer surface under high magnification (Figure 5.5 (i) and Figure 5.5 (f)). Similar salt crystal formation phenomena have been recored in other studies[131, 188] without showing an exact reason. We attribute the reason for salt crystals formed on the fiber surface to the moisture in the air, since it is reasonable rendering the hydrophilic nature of $LiBF_4$ salt, which will preferentially dissolve in water rather than the PIL matrix.[189]

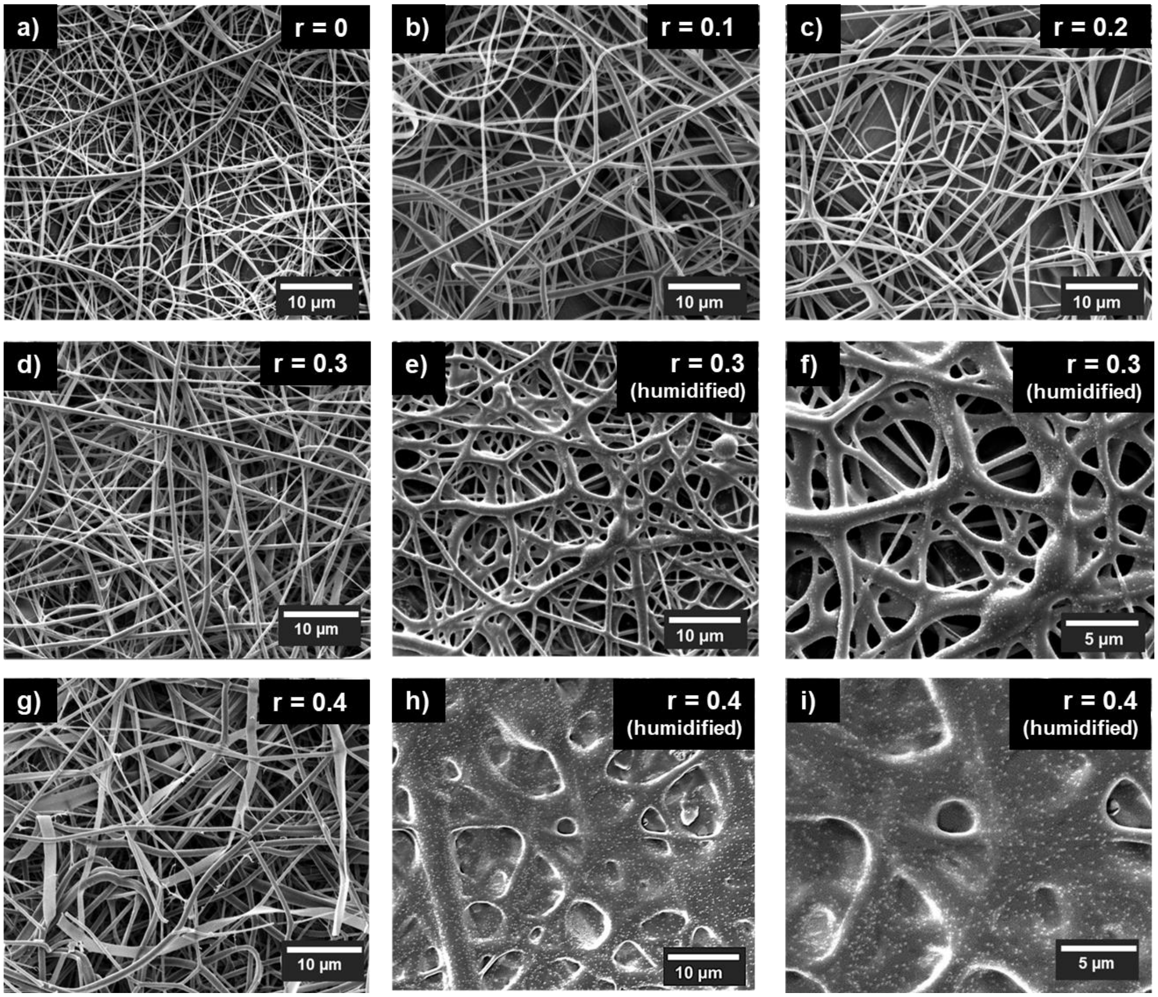

Figure 5.5 SEM images of electrospun poly(VBBIm-BF_4) fibers with various $LiBF_4$ ratios r = $[Li^+]/[BIm^-]$ (mol/mol): (a) 0, (b) 0.1, (c) 0.2, (d) 0.3, (e–f) humidified 0.3, (g) 0.4, (h–i) humidified 0.4. Magnification: (a), (b), (c), (d), (e), (g), (h) 5000X, (f), (i) 10000 X.

5.3.3. Thermal Analysis

The DSC thermograms for film and fibers of the neat poly(VBBIm-BF_4) (r = 0) and polymers doped with different lithium salt concentrations (r = 0.1–0.4) are shown in Figure 5.6, and the glass transition temperatures (T_g) are listed in Table 5.1. In Figure 5.5 (a), the neat PIL film exhibits a single T_g at 87 °C. As the Li salt ratio increases from 0.1 to 0.4, the T_g decreases from 71 to 38 °C, which is more significant than Chen *et al.*[150] observed in a similar PIL diblock copolymer. For the fibers, the neat PIL fiber also exhibits a single T_g at 87 °C, which is the same as the film counterpart. Contrastingly, as the salt ratio increased to 0.1 and 0.2, the T_g remained constant at 87 °C, and only slightly decreased to 75 °C at 0.3 and 0.4, which are significantly higher than the film counterpart at the same salt ratio. Numerous studies[150, 184] have shown that the T_g is strongly influenced by ion-ion dissociation and the free volume. In a PIL/salt binary system, ion dynamics are more complicated influenced by the interaction between poly(VBBIm-BF_4) and the additional $BF4^-$ anion in Li salt.[190, 191] To understand the question of why the size confinement within nanofiber structure could dampen the dependence of T_g on the salt ratio, we can reasonably hypothesize that the ion-ion association states are drastically different for PIL film and PIL nanofiber. The Li salt might get trapped or “frozen” so that the $BF4^-$ anions are not interacting with poly($VBBIm^+$) enough to change its segmental motion and lower the T_g.

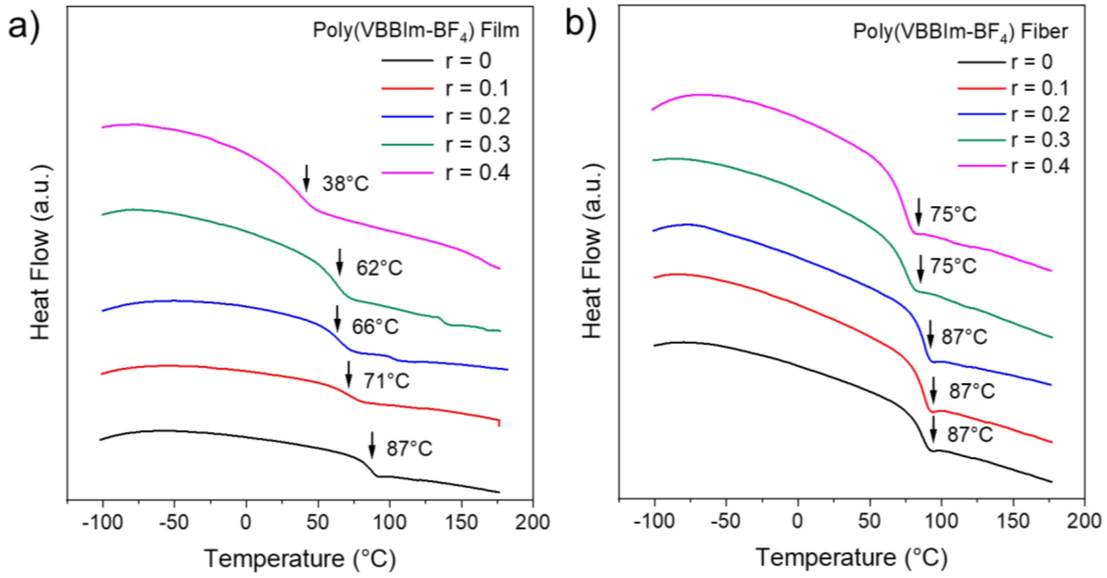

Figure 5.6 DSC thermograms for (a) solution-casted films and (b) electrospun fibers of poly(VBBIm-BF_4) with various salt ratio r = [Li^+]/[BIm^-] (mol/mol) = 0, 0.1, 0.2, 0.3, and 0.4.

The TGA thermograms of poly(VBBIm-BF_4) films and fibers are shown in Figure 5.7, and the thermal decomposition temperatures (T_d) are listed in Table 5.1. Less than 1% weight loss for all samples below 100 °C indicates trivial inside moisture content. For solution-casted films (Figure 5.7 (a)), we observe the onset of decomposition (the temperature at which 5% weight loss is observed) at 216–305 °C, which should be attributed to the decomposition of $LiBF_4$ salt. As the concentration of the salt increases, the initial decomposition temperature of the electrolyte decreases accordingly. The second decomposition event occurring at 360–375 °C can be attributed to the degradation of pendant groups with weakly coordinating BF_4^- on the polymer backbone.[192, 193] The third decomposition event temperature is relatively constant (442–448 °C), which should be attributed to the degradation of the poly(styrene) backbone.[193] In sharp contrast to these results, the onset of decomposition for the fibers occurs at 303–312 °C, which are significantly higher than the film counterparts (216–305 °C), specifically at high salt ratios (*i.e.,* 0.3 and 0.4). This phenomenon might be due to the different dissociation degrees of $LiBF_4$ salt in film and fibers, which influenced its degradation temperature in turn. Both the second (360–376 °C) and third (436–445 °C) decomposition events of the poly(VBBIm-BF_4) occurred in a similar range for film and fiber samples due to the same pendant group and backbone chemistry. The enhancement of onset decomposition temperature could be traced back to the ordered polymer chains alignment during the whipping and stretching and occurs under a strong electric field (*ca.* 3×10^3 V cm^{-1}) in electrospinning. Similar thermal stability improvement and analysis have also been demonstrated in other neutral homopolymers (*e.g.,* semi-crystalline polycaprolactone, amorphous poly(methyl methacrylate)) studies by Macossary *et al.*,[194] Dhakate *et al.*,[195] and Sheng *et al.*.[196]

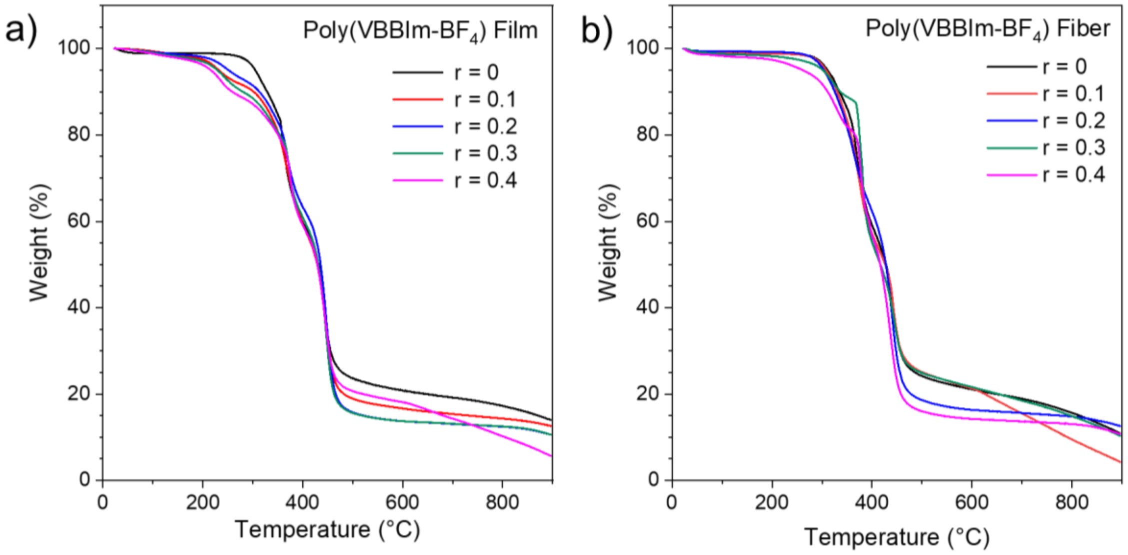

Figure 5.7 TGA thermograms for (a) solution-casted films and (b) electrospun fibers of poly(VBBIm-BF$_4$) with various salt ratio r = [Li$^+$]/[BIm$^-$] (mol/mol) = 0, 0.1, 0.2, 0.3, and 0.4.

Table 5.1 Thermal decomposition temperature (T_d) and glass transition temperature (T_g) of Poly(VBBIm-BF$_4$) with different salt ratios.

Salt ratio in poly(VBBIm-BF$_4$)[a]	T_d (°C)[b]		T_g (°C)[c]	
	Film	Fiber	Film	Fiber
r = 0.0	305, 360, 442	312, 369, 443	87	87
r = 0.1	232, 365, 448	311, 372, 442	71	87
r = 0.2	251, 368, 448	307, 363, 440	66	87
r = 0.3	229, 371, 447	304, 380, 445	62	75
r = 0.4	216, 375, 447	303, 376, 436	38	75

[a] r = [Li$^+$]/[BIm$^-$] (mol/mol)

[b] Determined from the average values observed on the second heating cycle by DSC.

[c] Onset degradation temperature (*i.e.,* 5% weight loss) and the peak temperatures for the highest weight loss rate for each observed decomposition event by TGA.

5.3.4. Conductivity

Figure 5.8 shows the temperature-dependent (50−100 °C) ionic conductivity under anhydrous conditions for poly(VBBIm-BF_4) homopolymer casted-films (Figure 5.8 (a)) and their analogous fibers (Figure 5.8 (b), normalized by surface porosity *ca.* 47.5%) with different salt concentration from r = 0–0.4. For solution-casted films, conductivity increases with increasing salt ratio, with the highest increment appearing when r increases from 0.2 to 0.3. In literature, nonmonotonic trend as a function of r (ranging 0.1–0.8, maximum conductivity at r = 0.5) for PIL homopolymer films was reported by Chen *et al.*[150], where the reduction at higher salt concentration was attributed to the formation of Li salt clusters. Here we did not observe an obvious decreasing trend of conductivity at high salt ratio, likely due to the limited salt concentration ranges (0.1–0.4). Interestingly, the fibers still demonstrate an increase from r = 0.3 to 0.4, which suggests that the nanofiber might reduce the Li clusters that hinder the continuing increases of conductivity. In comparison, the conductivity for the electrospun fibers (Figure 5.8 (b)) at higher salt ratio generally show similar conductivities to the film counterparts (*e.g.,* 2.9×10^{-5} S cm^{-1} *versus* 1.7×10^{-5} S cm^{-1} at r = 0.4, 100 °C). At low salt concentration and lower temperatures, electrospun fibers showed lower conductivities than the film counterpart (*e.g.,* 2.4×10^{-9} S cm^{-1} *versus* 2.2×10^{-10} S cm^{-1} at r = 0.1, 50 °C).

In PIL homopolymer electrolytes, the ion transport mechanisms are governed by polymer chain segmental dynamics, ion hopping, ion-pair dissociation−association process, and backbone to backbone distance.[197] In electrospun fibers, however, the dependence of conductivity on T_g are reduced, which could be realized through forced ion dissociation by the strong electrostatic forces or the reduction of backbone to backbone distance (*i.e.*, alignment chain conformation). Therefore, electrospinning PILs would be a promising way to fabricate robust (high T_g) but highly-conductive porous SPEs. One may argue the conductivity we achieved in the current poly(VBBIm-BF_4)/$LiBF_4$ system are low; there are various approaches to tackle the problems (*e.g.*, add ILs as a plasticizer), which would be interesting to explore in the future, but is beyond the scope of this study. For example, Chen *et al.*[130] showed a conductivity of 7.12×10^{-7} S cm^{-1} for methacrylate-based PIL electrospun fibers at 10% RH and 30 °C. By doping with ILs, they improved conductivities by four orders of magnitude (3.15–17.4×10^{-3} S cm^{-1}). Therefore, desirable conductivity could be facilitated by future investigation of IL-doped PIL nanofiber.

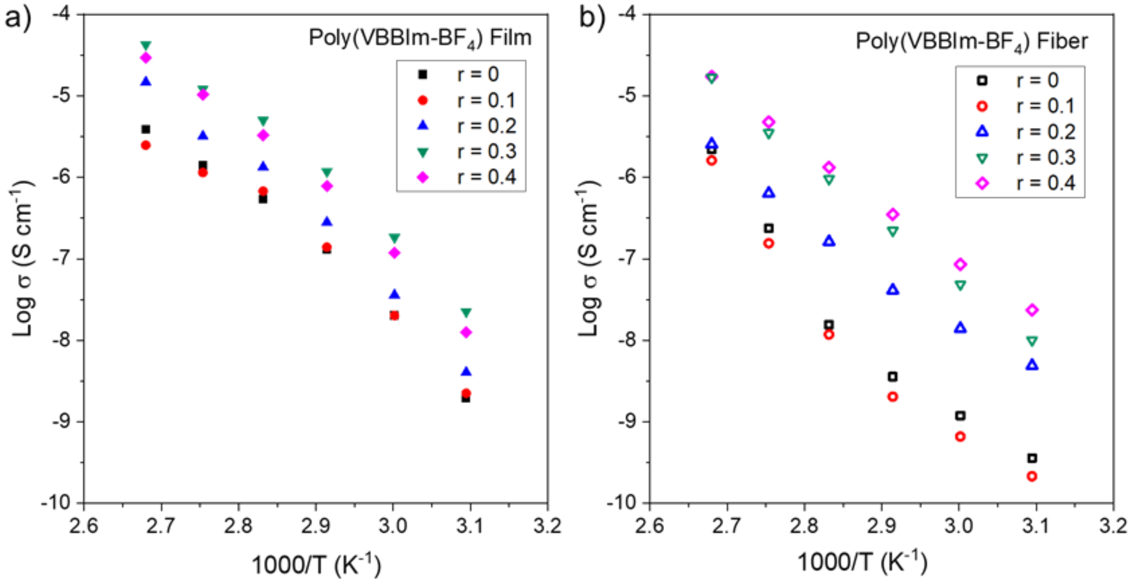

Figure 5.8 Ionic conductivity as a function of temperature for (a) solution-casted films and (b) electrospun fibers of poly(VBBIm-BF_4) with various salt ratio r = $[Li^+]/[BIm^-]$ (mol/mol) = 0, 0.1, 0.2, 0.3, and 0.4. (Note that ionic conductivities are normalized in (b) by fibers surface porosity)

5.4. Conclusions

In this study, Li salt-doped electrospun fibers and solution-casted films were successfully fabricated for a styrene-based PIL homopolymer (*i.e.*, poly(VBBIm-BF_4)) in order to investigate the influence of nanofiber confinement on the thermal and ion-conducting properties. The electrospun fiber morphology, glass transition temperature, thermal stability, and ionic conductivities were evaluated as a function of Li salt ratio and compared between PIL films and fibers. The results show that the T_g remained relatively constant in the fibers regardless of the Li salt ratio, in contrast with the depressed T_g at high salt ratio in solution-casted films. Surprisingly, the ionic conductivities of the fibers were comparable with the solution-cast solid film (*ca.* 2.9×10^{-5} S cm^{-1} at r = 0.4, 100 °C) analogs despite the high T_g (75 °C at r = 0.4). This result suggests that the commonly observed tradeoff between the conductivity and mechanical properties may be decoupled in the nanofiber system. Future investigations of PIL electrospun fibers in Li symmetric cells to explore the electrochemical stability will be of great interest for rendering these materials as potential separator candidates in all-solid-state Li^+ batteries.

CHAPTER 6.

CONCLUSIONS AND FUTURE OUTLOOK

6.1. Summary

Engineering of polyelectrolytes in electrodes and membranes is required to obtain high performance, high energy efficiency, and low-cost commercial PEMFCs and PEM-based electrolytic dehumidifiers. Traditional proton-conducting polyelectrolytes (*e.g.*, Nafion) suffer from high production and recycling cost, and only exhibit limited IECs. Alternative PEM materials and nanofabrication methods that alleviate the transport resistances inside electrodes and membranes are of great research interest, however, remain less explored. In this work, nanofiber-nanoparticle electrodes with patterned overarching structures were developed for PEMFCs. Proton-conducting hydrocarbon polyelectrolytes with higher IECs were explored in PEM-based dehumidifiers, with thermal and ion transport properties systematically explored, revealing promising electrochemical performances.

3D hexagonal patterned nanofiber-nanoparticle PEMFC electrodes (i.*e.*, pattern diameters of 40, 80, 160, and 360 μm) with ultra-low Pt loadings (*ca.* 0.06 $\text{mg}_{\text{Pt}}\ \text{cm}^{-2}$) were systematically developed *via* template-assisted E/E technique to investigate the patterning effect on the fuel cell performance and Pt utilization. The results were examined in comparison with the randomly assembled conventional E/E electrodes. An optimal of 80 μm pattern diameter was identified to present Pt utilization of 8.26 kW $\text{g}_{\text{Pt}}^{-1}$, showing 42% increase relevant to the analogous random electrodes, which proved our hypothesis that the reorganization of the proton-conducting nanofibers and catalyst particles could influence TPBs and Pt utilization.

In order to evaluate alternative hydrocarbon membranes in replacing the benchmark Nafion and lower the PEM cost, NEXAR® (a commercial sulfonated pentablock terpolymer) with different IECs (1.0 and 2.6 meq g^{-1}) were investigated in a PEM-based electrolytic dehumidifier. Similar functions (*i.e.,* proton-conducting media and separator) of the PEM in fuel cell and reverse fuel cell validate the switch of research system. These NEXAR membranes demonstrated higher WVTR and water removal efficiency than the commercial perfluorinated membrane (Nafion, 0.9 meq g^{-1}) at 50 °C. Surprisingly, NEXAR-1.0 exhibited higher water removal efficiency relative to NEXAR-2.6, despite its lower IEC. The counter-intuitive result was attributed to the excessive water uptake of NEXAR-2.6, resulting in inefficient current consumption. Moreover, operational factors including voltage application directions and external humidity gradients were also analyzed to enhance dehumidification performance practically.

The results of the above studies led to the investigation of electrospinning fabrication of pure NEXAR nanofibers (IECs of 1.0 and 2.0 meq g^{-1}) without carrier polymers, which is challenging (*e.g.,* impossible to produce 100% pure electrospun Nafion nanofibers) due to the electrostatic charges along the polymer backbone, as well as the amphiphilic nature of NEXAR polymer. The relationships among electrospinability and intrinsic solution properties were elucidated through modulating the solution polarity in two binary solvent mixtures (*i.e.,* toluene (nonpolar)/1-propanol (strong polar); THF (medium polar)/1-propanol (strong polar)). Comparatively, the THF/1-propanol binary solvent mixture resulted in enhanced electrospinability and broader tunability for NEXAR nanofiber formation, as evidenced by SEM, DLS, SAXS, and viscosity/conductivity characterization. In addition, the IEC of NEXAR® also greatly influence the electrospinning morphology due to sulfonation group concentration. These results provide insights into amphiphilic polyelectrolytes electrospinning, which prepares for potential applications as nanofiber membranes or electrodes in PEMFCs or PEM dehumidifiers.

Lithium-doped poly(ionic liquids) (PILs) homopolymer nanofibers were developed *via* electrospinning to advance the development of a high surface area, light-weight polyelectrolyte in electrochemical devices (*e.g.*, Li^+ batteries). Poly(vinylbenzyl chloride) (poly(VBC)) was used as a precursor for PIL synthesis that was further functionalized with 1-butylimidazole (BIm) and ion-exchanged to tetrafluoroborate (BF_4) to incorporate conductive cations. It was hypothesized that the physiochemical and ion conduction properties will be affected by the chain confinement in the nanofibers. In comparison with Li^+ doped solution-cast film analogs, the fibers showed higher thermal stability (higher T_d), and comparable ionic conductivity despite the significantly higher T_g at high salt ratio, suggesting that the salt-doped PIL nanofiber can be applied as the mechanically strong SPEs in solid-state Li^+ batteries.

6.2. Future Directions

The findings of this dissertation can be extended into multiple interesting avenues for the development of fuel cells and reverse fuel cells with nanostructured membrane and electrodes. For the patterned electrodes of PEMFCs, exploration of alternative pattern features (*e.g.,* shapes, sizes, connections) would be beneficial for the pursuit of further Pt utilization improvement. For PEM-based electrolytic dehumidifier, incorporation of proton-conductive nanofiber to lower the catalyst loading remains an unexplored area of research. In addition, nanofiber engineering, such as core-shell structure nanofiber (*i.e.,* high mechanical strength core) and phase-segregated PIL diblock copolymer nanofiber (*i.e.,* a second mechanical strong block) could offer more insights into fabrication of highly proton-conductive and mechanically robust nanofibrous membranes for fuel cell and reverse fuel cell dehumidifiers.

6.2.1. Alternative Pattern Features for PEMFC Electrodes

In Chapter 2, hexagonal patterned electrodes with micron-scale feature sizes were implemented in the PEMFC; however, alternative pattern shapes and sizes are remain unexplored. For the design of future template-assisted E/E fabricated electrode pattern structure, there are several key points to consider to reduce the transport resistances, referring to the design concepts in flow fields pattern[198] and hydrophobic additives distribution pattern[199]: (1) the geometrical length scale of the pattern and its relationship with the water management in the electrode; (2) the shape of the pattern (*e.g.,* angled or round feature, serpentine or straight channel); (3) the connectivity of the channel and land area, *i.e.,* whether the continuous phase of the pattern should be catalyst-rich or catalyst-thin. Examples of different electrode pattern designs (*e.g.,* connectivity, shapes, feature sizes) are illustrated in Figure 6.1. From the standpoint of fabrication, the edge angle of the pattern feature should also be taken into account, since it could influence the residual charge distribution and influence the controlling ability of the templates on nanofiber and nanoparticle deposition.[200-202]

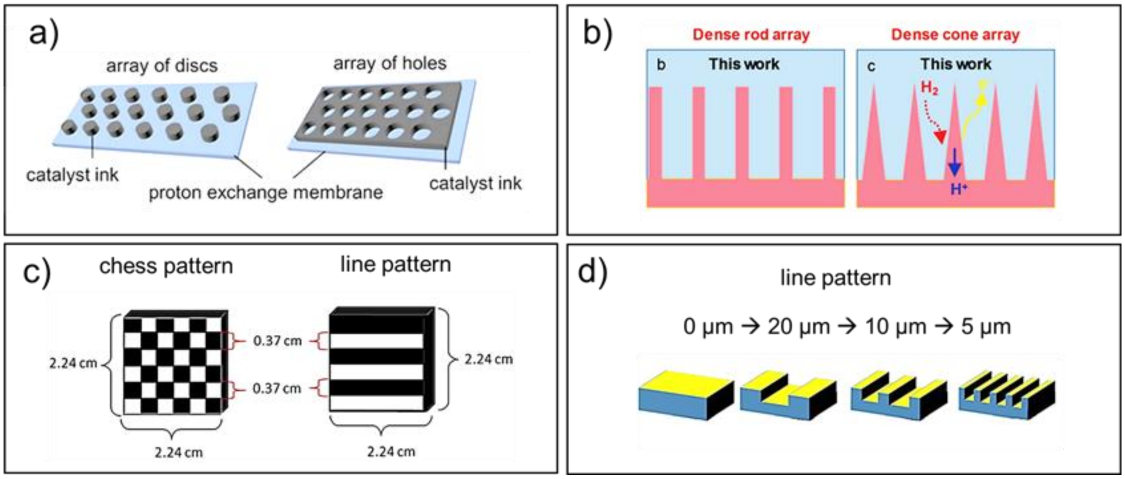

Figure 6.1 Illustration of various electrode pattern designs adapted from literature: (a) array of discs and holes[49], (b) array of dense rods and cones[51], (c) chess and line pattern[23], and (d) different line pattern width[43].

6.2.2. Nanofibrous Electrodes for PEM Dehumidifiers

As an emerging dehumidification technology, the PEM-based electrolytic dehumidifier investigated in Chapter 3 still suffers from extremely high noble metal catalyst loading[203, 204], *i.e.*, 1.0–3.0 mg cm^{-2} (*ca.* two orders of magnitude higher than the counterpart of 0.05 mg$_{Pt}$ cm^{-2} in PEMFC).[78] Examples of reducing catalyst loading *via* nanofiber electrodes has been demonstrated in water electrolysis. Hegge *et al.*[205] showed the efficient and stable PEM water electrolysis with electrospun whisker-shaped iridium oxide (IrO_x) nanofiber (poly(vinyl alcohol) (PVA) as the carrier polymer) interlayers. Wang *et al.*[206] showed electrospun Pt-IrO_2 nanofiber (polyvinyl pyrrolidone (PVP) as the carrier polymer) successfully reduced the catalysts loading and H_2 crossover. However, no such reports in PEM dehumification. Chapter 4 systematically investigated the electrospinning properties of the NEXAR®, which has paved the way for this research direction. Therefore, referring to the ultra-low Pt loading electrode fabrication technique demonstrated in Chapter 1, it would be of great interest to incorporate the sulfonated pentablock terpolymer as building blocks for nanofiber-nanoparticle electrodes to reduce the transport resistance and thus the catalyst loading inside a PEM-based dehumidifier.

6.2.3. Core-Shell Proton-Conductive Nanofiber *via* Coaxial Electrospinning

Pure electrospun proton-conductive nanofiber can exhibit an order of magnitude higher conductivity than bulk film, as demonstrated by Dong *et al.*[120]. However, it still suffers from insufficient mechanical strength. Therefore, nanofibers with core-shell structure, *i.e.,* mechanically strong core and ion conductive shell (Figure 6.1 (a)), would be of great interest to be applied in electrochemical devices. For instance, Yuan *et al.*[207] demonstrated coaxial electrospun sulfonated poly (ether ether ketone) (SPEEK) PEM for conductivity-strength balance with a low degree of sulfonation (DS) core and high DS shell design. However, explorations in such concept with alternative chemistry remain scarce. In addition, the fine-tuning of shell thickness could further promote proton conductivity due to the nanosize effect.[120] Preliminary experiments have been performed to explore the influence of different core carriers (*i.e.*, polyacrylonitrile, mineral oil, polystyrene, and poly(styrene-*b*-ethylene-*b*-styrene)) on the compound Taylor cone formation, as shown in Figure 6.1(b). The interaction between the shell and core solution properties (*e.g.*, conductivity, viscosity) could provide fundamental insights into the physics of compound droplet formation.[208] Preliminary transmission electron microscopy (TEM) images characterized both the through-plane (Figure 6.1(c)) and the in-plane (Figure 6.1(d)) cross-sectional area of the core-shell nanofiber samples, which were embedded in epoxy and then microtomed to < 100 nm thickness. The RuO_4 dyed Nafion shell exhibits darker color, whereas the PAN core was could not be crosslinked by the RuO_4 and appears lighter color.

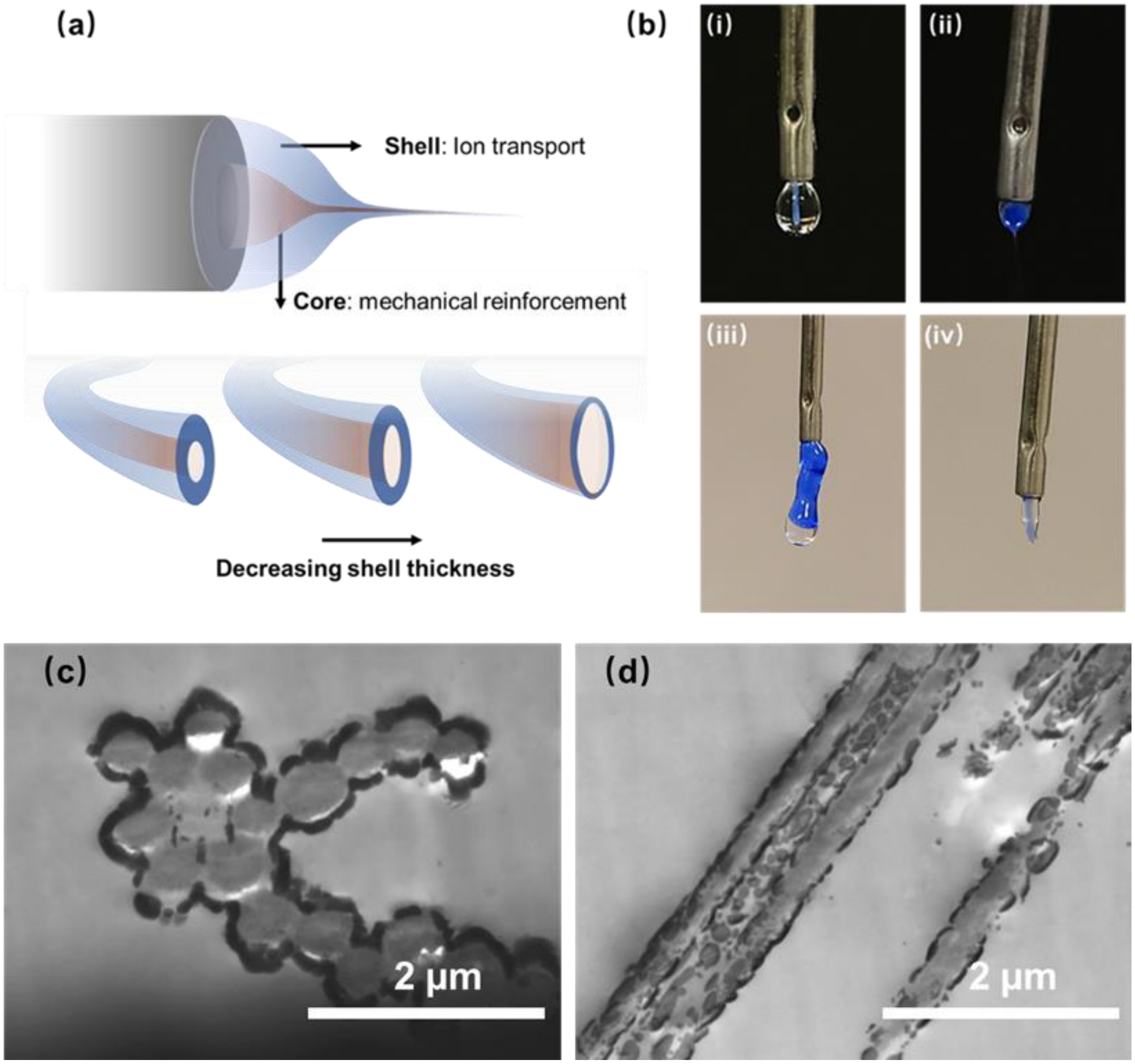

Figure 6.2 (a) schematic of the core-shell mechanically reinforced nanofiber produced *via* coaxial electrospinning, and (b) core-shell compound Taylor cones (*i.e.*, with shell solution of 20 wt% Nafion in DMF/acetone (5/1 w/w), which is dyed with ultramarine oil paint, and various core solution of (i) polyacrylonitrile(PAN) in 10 wt% DMF, (ii) mineral oil, (iii) polystyrene in 20 wt% THF and (iv) poly(styrene-b-ethylene-b-styrene) in 20 wt% toluene), TEM images of core-shell nanofiber for (c) through-plane, and (d) in-plane fiber cross-sectional structure.

6.2.4. Electrospun PIL Diblock Copolymer Nanofibers

In chapter 5, physicochemical properties were compared between nanofibers and solution-casted films for a PIL homopolymer. Current literature[150, 209] shows the Li transport properties in PIL diblock copolymer films under various salt concentrations. However, the microphase-separation morphologies in 2D-confined electrospun nanofiber have only been well-documented for neutral diblock copolymers, such as poly(styrene-*b*-butyl-*b*-styrene) (PSBS) and poly(styrene-*b*-isoprene) (PSI), as shown in Figure 6.2. The intersection of both directions, *i.e.,* Li transport properties and its relationship with the microphase-separation morphology in a 2D-confined cylindrical PIL diblock nanofibers has not been reported yet. The Li conductivity could be correlated with the strength of confinement[160] (D/L_0, where D is the size of the confining space, *i.e.,* the diameter of nanofiber, and L_0 is the periodicity of the PIL diblock copolymer), and may reveal new insights into the conductivity-morphology relationship.

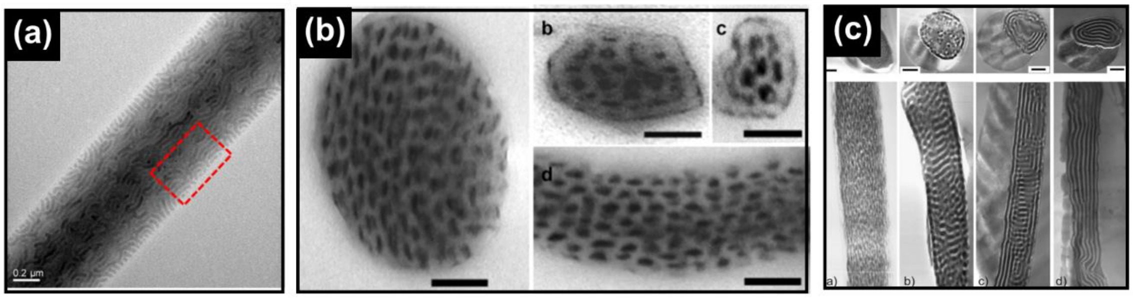

Figure 6.3 Transmission electron microscopy (TEM) images of microphase separated block copolymer nanofiber morphology adapted from literatures. (a) Electrospun PSBS fibers after annealing at 70 °C for 24 h ,[210] (b) PSI fibers after annealing at 140 °C for 10 days,[211] and (c) PSI fibers at various annealing temperatures and times.[212]

REFERENCES

1. Pérez-Lombard, L.; Ortiz, J.; Pout, C., A review on buildings energy consumption information. *Energy and Buildings* **2008,** *40* (3), 394-398.

2. IEA, U., Global energy review 2020. **2020**.

3. Thomas, C. S., Transportation options in a carbon-constrained world: Hybrids, plug-in hybrids, biofuels, fuel cell electric vehicles, and battery electric vehicles. *International Journal of hydrogen energy* **2009,** *34* (23), 9279-9296.

4. SATO, S.; Jiang, Y. J.; Russell, R. L.; Miller, J. W.; Karavalakis, G.; Durbin, T. D.; Johnson, K. C., Experimental Driving Performance Evaluation of a Battery-Powered Medium and Heavy Duty All-Electric Vehicles. *Social Science Research Network* **2021**.

5. Kurtz, J. M.; Sprik, S.; Saur, G.; Onorato, S., On-road fuel cell electric vehicles evaluation: overview. **2019**.

6. Rudolf, T.; Schürmann, T.; Schwab, S.; Hohmann, S., Toward Holistic Energy Management Strategies for Fuel Cell Hybrid Electric Vehicles in Heavy-Duty Applications. *Proceedings of the IEEE* **2021,** *109* (6), 1094-1114.

7. Wang, Y.; Ruiz Diaz, D. F.; Chen, K. S.; Wang, Z.; Adroher, X. C., Materials, technological status, and fundamentals of PEM fuel cells – A review. *Materials Today* **2020,** *32*, 178-203.

8. Mattison, L.; Korn, D., Dehumidifiers: A Major Consumer of Residential Electricity. *Summer Study for Energy Efficiency in Buildings* **2012**, 9-204.

9. Liu, H.; Yang, H.; Qi, R., A review of electrically driven dehumidification technology for air-conditioning systems. *Applied Energy* **2020,** *279*, 115863.

10. Zhang, L. Z., Energy performance of independent air dehumidification systems with energy recovery measures. *Energy* **2006,** *31* (8), 1228-1242.

11. Ortiz-Rivera, E. I.; Reyes-Hernandez, A. L.; Febo, R. A. In *Understanding the history of fuel cells*, 2007 IEEE conference on the history of electric power, IEEE: 2007; pp 117-122.

12. Wilson, M. S.; Gottesfeld, S., Thin-film catalyst layers for polymer electrolyte fuel cell electrodes. *Journal of applied electrochemistry* **1992,** *22* (1), 1-7.

13. Mehta, V.; Cooper, J. S., Review and analysis of PEM fuel cell design and manufacturing. *Journal of Power Sources* **2003,** *114* (1), 32-53.

14. Dhanda, A.; Pitsch, H.; O'Hayre, R., Diffusion Impedance Element Model for the Triple Phase Boundary. *Journal of The Electrochemical Society* **2011,** *158* (8).

15. Blom, D. A.; Dunlap, J. R.; Nolan, T. A.; Allard, L. F., Preparation of Cross-Sectional Samples of Proton Exchange Membrane Fuel Cells by Ultramicrotomy for TEM. *Journal of The Electrochemical Society* **2003,** *150* (4).

16. Majlan, E. H.; Rohendi, D.; Daud, W. R. W.; Husaini, T.; Haque, M. A., Electrode for proton exchange membrane fuel cells: A review. *Renewable and Sustainable Energy Reviews* **2018,** *89*, 117-134.

17. Debe, M. K., Electrocatalyst approaches and challenges for automotive fuel cells. *Nature* **2012,** *486* (7401), 43-51.

18. Wang, Y.; Chen, K. S.; Mishler, J.; Cho, S. C.; Adroher, X. C., A review of polymer electrolyte membrane fuel cells: Technology, applications, and needs on fundamental research. *Applied energy* **2011,** *88* (4), 981-1007.

19. Gottesfeld, S.; Zawodzinski, T. A., Polymer electrolyte fuel cells. *Advances in electrochemical science and engineering* **1997,** *5*, 195-302.

20. Antolini, E.; Giorgi, L.; Pozio, A.; Passalacqua, E., Influence of Nafion loading in the catalyst layer of gas-diffusion electrodes for PEFC. *Journal of Power Sources* **1999,** *77* (2), 136-142.

21. Xie, J.; Xu, F.; Wood III, D. L.; More, K. L.; Zawodzinski, T. A.; Smith, W. H., Influence of ionomer content on the structure and performance of PEFC membrane electrode assemblies. *Electrochimica Acta* **2010,** *55* (24), 7404-7412.

22. González Rodríguez, L.; Campana Prada, R.; Sanchez-Molina, M.; Rodríguez Victoria, T. A., Study of the influence of Nafion/C composition on electrochemical performance of PEM single cells with ultra-low platinum load. *International Journal of Hydrogen Energy* **2021,** *46* (33), 17550-17561.

23. Therdthianwong, A.; Saenwiset, P.; Therdthianwong, S., Cathode catalyst layer design for proton exchange membrane fuel cells. *Fuel* **2012,** *91* (1), 192-199.

24. Öztürk, A.; Fıçıcılar, B.; Eroğlu, İ.; Bayrakçeken Yurtcan, A., Facilitation of water management in low Pt loaded PEM fuel cell by creating hydrophobic microporous layer with PTFE, FEP and PDMS polymers: Effect of polymer and carbon amounts. *International Journal of Hydrogen Energy* **2017,** *42* (33), 21226-21249.

25. Avcioglu, G. S.; Ficicilar, B.; Eroglu, I., Effect of PTFE nanoparticles in catalyst layer with high Pt loading on PEM fuel cell performance. *International Journal of Hydrogen Energy* **2016,** *41* (23), 10010-10020.

26. Ngo, T. T.; Yu, T. L.; Lin, H.-L., Influence of the composition of isopropyl alcohol/water mixture solvents in catalyst ink solutions on proton exchange membrane fuel cell performance. *Journal of Power Sources* **2013,** *225*, 293-303.

27. Sharma, R.; Andersen, S. M., Zoom in catalyst/ionomer interface in polymer electrolyte membrane fuel cell electrodes: Impact of catalyst/ionomer dispersion media/solvent. *ACS applied materials & interfaces* **2018,** *10* (44), 38125-38133.

28. Jung, C.-Y.; Kim, W.-J.; Yi, S.-C., Optimization of catalyst ink composition for the preparation of a membrane electrode assembly in a proton exchange membrane fuel cell using the decal transfer. *International Journal of Hydrogen Energy* **2012,** *37* (23), 18446-18454.

29. Wang, M.; Park, J. H.; Kabir, S.; Neyerlin, K. C.; Kariuki, N. N.; Lv, H.; Stamenkovic, V. R.; Myers, D. J.; Ulsh, M.; Mauger, S. A., Impact of Catalyst Ink Dispersing Methodology on Fuel Cell Performance Using in-Situ X-ray Scattering. *ACS Applied Energy Materials* **2019,** *2* (9), 6417-6427.

30. Stähler, M.; Stähler, A.; Scheepers, F.; Carmo, M.; Stolten, D., A completely slot die coated membrane electrode assembly. *International Journal of Hydrogen Energy* **2019,** *44* (14), 7053-7058.

31. Breitwieser, M.; Klingele, M.; Vierrath, S.; Zengerle, R.; Thiele, S., Tailoring the Membrane - Electrode Interface in PEM Fuel Cells: A Review and Perspective on Novel Engineering Approaches. *Advanced Energy Materials* **2018,** *8* (4), 1701257.

32. Chen, M.; Zhao, C.; Sun, F.; Fan, J.; Li, H.; Wang, H., Research progress of catalyst layer and interlayer interface structures in membrane electrode assembly (MEA) for proton exchange membrane fuel cell (PEMFC) system. *eTransportation* **2020,** *5*, 100075.

33. Bae, W. G.; Kim, H. N.; Kim, D.; Park, S. H.; Jeong, H. E.; Suh, K. Y., 25th anniversary article: scalable multiscale patterned structures inspired by nature: the role of hierarchy. *Advanced Materials* **2014,** *26* (5), 675-700.

34. Towne, S.; Viswanathan, V.; Holbery, J.; Rieke, P., Fabrication of polymer electrolyte membrane fuel cell MEAs utilizing inkjet print technology. *Journal of Power Sources* **2007,** *171* (2), 575-584.

35. Taylor, A. D.; Kim, E. Y.; Humes, V. P.; Kizuka, J.; Thompson, L. T., Inkjet printing of carbon supported platinum 3-D catalyst layers for use in fuel cells. *Journal of Power Sources* **2007,** *171* (1), 101-106.

36. Shukla, S.; Domican, K.; Secanell, M., Effect of electrode patterning on pem fuel cell performance using ink-jet printing method. *ECS Transactions* **2014,** *64* (3), 341-352.

37. Bae, I.; Kim, B.; Kim, D.-Y.; Kim, H.; Oh, K.-H., In-plane 2-D patterning of microporous layer by inkjet printing for water management of polymer electrolyte fuel cell. *Renewable Energy* **2020,** *146,* 960-967.

38. Kim, J.; Yamagata, Y.; Kim, B.; Higuchi, T., Direct and dry micro-patterning of nano-particles by electrospray deposition through a micro-stencil mask. *Journal of Micromechanics and Microengineering* **2009,** *19* (2), 025021.

39. Yan, W.-C.; Xie, J.; Wang, C.-H., Electrical Field Guided Electrospray Deposition for Production of Gradient Particle Patterns. *ACS Applied Materials & Interfaces* **2018,** *10* (22), 18499-18506.

40. Shah, K.; Shin, W.; Besser, R., Novel microfabrication approaches for directly patterning PEM fuel cell membranes. *Journal of power sources* **2003,** *123* (2), 172-181.

41. Bae, J. W.; Cho, Y.-H.; Sung, Y.-E.; Shin, K.; Jho, J. Y., Performance enhancement of polymer electrolyte membrane fuel cell by employing line-patterned Nafion membrane. *Journal of Industrial and Engineering Chemistry* **2012,** *18* (3), 876-879.

42. Aizawa, M.; Gyoten, H.; Salah, A.; Liu, X., Pillar Structured Membranes for Suppressing Cathodic Concentration Overvoltage in PEMFCs at Elevated Temperature/Low Relative Humidity. *Journal of The Electrochemical Society* **2010,** *157* (12), B1844.

43. Koh, J. K.; Jeon, Y.; Cho, Y. I.; Kim, J. H.; Shul, Y.-G., A facile preparation method of surface patterned polymer electrolyte membranes for fuel cell applications. *Journal of Materials Chemistry A* **2014,** *2* (23), 8652-8659.

44. Omosebi, A.; Besser, R. S., Electron beam patterned Nafion membranes for DMFC applications. *Journal of Power Sources* **2013,** *228,* 151-158.

45. Zhou, Z.; Dominey, R. N.; Rolland, J. P.; Maynor, B. W.; Pandya, A. A.; DeSimone, J. M., Molded, High Surface Area Polymer Electrolyte Membranes from Cured Liquid Precursors. *Journal of the American Chemical Society* **2006,** *128* (39), 12963-12972.

46. Rolland, J. P.; Hagberg, E. C.; Denison, G. M.; Carter, K. R.; De Simone, J. M., High-Resolution Soft Lithography: Enabling Materials for Nanotechnologies. *Angewandte Chemie International Edition* **2004,** *43* (43), 5796-5799.

47. Chen, M.; Wang, M.; Yang, Z.; Ding, X.; Li, Q.; Wang, X., A novel catalyst layer structure based surface-patterned Nafion® membrane for high-performance direct methanol fuel cell. *Electrochimica Acta* **2018,** *263,* 201-208.

48. Yildirim, M. H.; te Braake, J.; Aran, H. C.; Stamatialis, D. F.; Wessling, M., Micro-patterned Nafion membranes for direct methanol fuel cell applications. *Journal of Membrane Science* **2010,** *349* (1), 231-236.

49. Paul, M. T.; Kim, D.; Saha, M. S.; Stumper, J.; Gates, B. D., Patterning Catalyst Layers with Microscale Features by Soft Lithography Techniques for Proton Exchange Membrane Fuel Cells. *ACS Applied Energy Materials* **2020**.

50. Kim, O.-H.; Cho, Y.-H.; Kang, S. H.; Park, H.-Y.; Kim, M.; Lim, J. W.; Chung, D. Y.; Lee, M. J.; Choe, H.; Sung, Y.-E., Ordered macroporous platinum electrode and enhanced mass transfer in fuel cells using inverse opal structure. *Nature communications* **2013,** *4* (1), 1-9.

51. Ning, F.; Bai, C.; Qin, J.; Song, Y.; Zhang, T.; Chen, J.; Wei, J.; Lu, G.; Wang, H.; Li, Y., Great improvement in the performance and lifetime of a fuel cell using a highly dense, well-ordered, and cone-shaped Nafion array. *Journal of Materials Chemistry A* **2020**.

52. Energy, U. D. o., DOE Technical Targets for Polymer Electrolyte Membrane Fuel Cell Components. **2019**.

53. Joseph, D.; Büsselmann, J.; Harms, C.; Henkensmeier, D.; Larsen, M. J.; Dyck, A.; Jang, J. H.; Kim, H.-J.; Nam, S. W., Porous Nafion membranes. *Journal of Membrane Science* **2016,** *520*, 723-730.

54. Ahlneck, C.; Zografi, G., The molecular basis of moisture effects on the physical and chemical stability of drugs in the solid state. *International journal of pharmaceutics* **1990,** *62* (2-3), 87-95.

55. Macleod, K. J., Relative Humidity: Its Importance, Measurement, and Control in Museums. **1975**.

56. Carcia, P. F.; McLean, R. S., Flexible organic electronic device with improved resistance to oxygen and moisture degradation. Google Patents: 2004.

57. Cai, C.; Rao, Y.; Zhou, J.; Zhang, L.; Chen, W.; Wan, Z.; Tan, J.; Pan, M., Carbon corrosion: A novel termination mechanism of the water electrolysis plateau during voltage reversal. *Journal of Power Sources* **2020,** *473*, 228542.

58. Spurgeon, J. M.; Lewis, N. S., Proton exchange membrane electrolysis sustained by water vapor. *Energy & Environmental Science* **2011,** *4* (8), 2993-2998.

59. Antoine, O.; Bultel, Y.; Durand, R., Oxygen reduction reaction kinetics and mechanism on platinum nanoparticles inside Nafion®. *Journal of Electroanalytical Chemistry* **2001,** *499* (1), 85-94.

60. Dai, W.; Wang, H.; Yuan, X.-Z.; Martin, J. J.; Yang, D.; Qiao, J.; Ma, J., A review on water balance in the membrane electrode assembly of proton exchange membrane fuel cells. *International Journal of hydrogen energy* **2009,** *34* (23), 9461-9478.

61. Pivovar, B. S., An overview of electro-osmosis in fuel cell polymer electrolytes. *Polymer* **2006,** *47* (11), 4194-4202.

62. Sakuma, S.; Yamauchi, S.; Takai, O., Water transfer simulation of an electrolytic dehumidifier. *Journal of applied electrochemistry* **2009,** *39* (6), 815-825.

63. Sakuma, S.; Yamauchi, S.; Takai, O., Estimation of dehumidifying performance of solid polymer electrolytic dehumidifier for practical application. *Journal of Applied Electrochemistry* **2010,** *40* (12), 2153-2160.

64. Qi, R.; Li, D.; Zhang, L.-Z.; Huang, Y., Experimental study on electrolytic dehumidifier with polymer electrolyte membrane for air-conditioning systems. *Energy Procedia* **2017,** *142*, 1908-1913.

65. Zhang, L.-Z.; Li, H.; Qi, R., Heat and mass transfer in PEM-based electrolytic air dehumidification element with an optimized anode-side electrochemical model. *International Journal of Heat and Mass Transfer* **2019,** *135*, 1152-1166.

66. Li, H.; Qi, R.; Zhang, L.-z., Analysis and optimization of material physical characteristics for electrolytic air dehumidifier with a PEM. *Applied Thermal Engineering* **2020,** *169*, 114929.

67. Sakuma, S.; Yamauchi, S.; Takai, O., V–I characteristics of solid polymer electrolytic (SPE) dehumidifier. *Journal of Applied Electrochemistry* **2011,** *41* (7), 839-848.

68. Li, D.; Qi, R.; Zhang, L.-Z., Electrochemical impedance spectroscopy analysis of V–I characteristics and a fast prediction model for PEM-based electrolytic air dehumidification. *International Journal of Hydrogen Energy* **2019,** *44* (36), 19533-19546.

69. Greenway, S. D.; Fox, E. B.; Ekechukwu, A. A., Proton exchange membrane (PEM) electrolyzer operation under anode liquid and cathode vapor feed configurations. *International Journal of Hydrogen Energy* **2009,** *34* (16), 6603-6608.

70. Li, D.; Qi, R.; Li, T.; Zhang, L.-Z., Durability analysis and degradation mechanism for an electrolytic air dehumidifier based on PEM. *International Journal of Hydrogen Energy* **2020,** *45* (7), 3971-3985.

71. Iwahara, H.; Matsumoto, H.; Takeuchi, K., Electrochemical dehumidification using proton conducting ceramics. *Solid State Ionics* **2000,** *136-137*, 133-138.

72. Iwahara, H.; Esaka, T.; Uchida, H.; Maeda, N., Proton conduction in sintered oxides and its application to steam electrolysis for hydrogen production. *Solid State Ionics* **1981,** *3*, 359-363.

73. Iwahara, H.; Esaka, T.; Uchida, H.; Yamauchi, T.; Ogaki, K., High temperature type protonic conductor based on SrCeO3 and its application to the extraction of hydrogen gas. *Solid State Ionics* **1986,** *18*, 1003-1007.

74. Sawada, S.; Yamaki, T.; Maeno, T.; Asano, M.; Suzuki, A.; Terai, T.; Maekawa, Y., Solid polymer electrolyte water electrolysis systems for hydrogen production based on our newly developed membranes, Part I: Analysis of voltage–current characteristics. *Progress in Nuclear Energy* **2008,** *50* (2), 443-448.

75. Li, D.; Qi, R.; Zhang, L.-Z., Performance improvement of electrolytic air dehumidification systems with high-water-uptake polymer electrolyte membranes. *Journal of Applied Polymer Science* **2019,** *136* (26), 47676.

76. Ito, H.; Maeda, T.; Nakano, A.; Takenaka, H., Properties of Nafion membranes under PEM water electrolysis conditions. *International Journal of Hydrogen Energy* **2011,** *36* (17), 10527-10540.

77. Qi, R.; Li, D.; Li, H.; Wang, H.; Zhang, L.-Z., Heat and mass transfer in a polymeric electrolyte membrane-based electrochemical air dehumidification system: Model development and performance analysis. *International Journal of Heat and Mass Transfer* **2018,** *126*, 888-898.

78. Carmo, M.; Fritz, D. L.; Mergel, J.; Stolten, D., A comprehensive review on PEM water electrolysis. *International journal of hydrogen energy* **2013,** *38* (12), 4901-4934.

79. Qi, R.; Li, D.; Zhang, L., Experimental investigation on membrane-based electrolytic dehumidification for air-conditioning systems. *Procedia Engineering* **2017,** *205*, 3194-3198.

80. Filice, S.; Urzì, G.; Milazzo, R.; Privitera, S.; Lombardo, S.; Compagnini, G.; Scalese, S., Applicability of a New Sulfonated Pentablock Copolymer Membrane and Modified Gas Diffusion Layers for Low-Cost Water Splitting Processes. *Energies* **2019,** *12* (11), 2064.

81. Qi, R.; Li, D.; Zhang, L.-Z., Performance investigation on polymeric electrolyte membrane-based electrochemical air dehumidification system. *Applied Energy* **2017,** *208*, 1174-1183.

82. Wang, X.; Richey, F. W.; Wujcik, K. H.; Elabd, Y. A., Ultra-low platinum loadings in polymer electrolyte membrane fuel cell electrodes fabricated via simultaneous electrospinning/electrospraying method. *Journal of Power Sources* **2014,** *264*, 42-48.

83. Wittmer, C. R.; Hébraud, A.; Nedjari, S.; Schlatter, G., Well-organized 3D nanofibrous composite constructs using cooperative effects between electrospinning and electrospraying. *Polymer* **2014,** *55* (22), 5781-5787.

84. Hwang, M.; Elabd, Y. A., Impact of ionomer resistance in nanofiber-nanoparticle electrodes for ultra-low platinum fuel cells. *International Journal of Hydrogen Energy* **2019,** *44* (12), 6245-6256.

85. Bett, J.; Kinoshita, K.; Routsis, K.; Stonehart, P., A comparison of gas-phase and electrochemical measurements for chemisorbed carbon monoxide and hydrogen on platinum crystallites. *Journal of Catalysis* **1973,** *29* (1), 160-168.

86. Springer, T.; Zawodzinski, T.; Wilson, M.; Gottesfeld, S., Characterization of polymer electrolyte fuel cells using AC impedance spectroscopy. *Journal of the Electrochemical Society* **1996,** *143* (2), 587.

87. Cooper, C. D.; Burk, J. J.; Taylor, C. P.; Buratto, S. K., Ultra-low Pt loading catalyst layers prepared by pulse electrochemical deposition for PEM fuel cells. *Journal of Applied Electrochemistry* **2017,** *47* (6), 699-709.

88. Klose, C.; Saatkamp, T.; Münchinger, A.; Bohn, L.; Titvinidze, G.; Breitwieser, M.; Kreuer, K. D.; Vierrath, S., All‐Hydrocarbon MEA for PEM Water Electrolysis Combining Low Hydrogen Crossover and High Efficiency. *Advanced Energy Materials* **2020,** *10* (14).

89. Linkous, C.; Anderson, H.; Kopitzke, R.; Nelson, G., Development of new proton exchange membrane electrolytes for water electrolysis at higher temperatures. *International Journal of Hydrogen Energy* **1998,** *23* (7), 525-529.

90. Albert, A.; Barnett, A. O.; Thomassen, M. S.; Schmidt, T. J.; Gubler, L., Radiation-grafted polymer electrolyte membranes for water electrolysis cells: evaluation of key membrane properties. *ACS applied materials & interfaces* **2015,** *7* (40), 22203-22212.

91. Wei, G.; Xu, L.; Huang, C.; Wang, Y., SPE water electrolysis with SPEEK/PES blend membrane. *International Journal of Hydrogen Energy* **2010,** *35* (15), 7778-7783.

92. Filice, S.; D'Angelo, D.; Scarangella, A.; Iannazzo, D.; Compagnini, G.; Scalese, S., Highly effective and reusable sulfonated pentablock copolymer nanocomposites for water purification applications. *RSC advances* **2017,** *7* (72), 45521-45534.

93. D’Angelo, D.; Filice, S.; Scarangella, A.; Iannazzo, D.; Compagnini, G.; Scalese, S., Bi2O3/Nexar® polymer nanocomposite membranes for azo dyes removal by UV–vis or visible light irradiation. *Catalysis Today* **2019,** *321,* 158-163.

94. Fan, Y.; Zhang, M.; Moore, R. B.; Cornelius, C. J., Structure, physical properties, and molecule transport of gas, liquid, and ions within a pentablock copolymer. *Journal of Membrane Science* **2014,** *464*, 179-187.

95. Willis, C. L.; Handlin Jr, D. L.; Trenor, S. R.; Mather, B. D., Sulfonated block copolymers, method for making same, and various uses for such block copolymers. Google Patents: 2010.

96. Rinaldo, S. G.; Monroe, C. W.; Romero, T.; Mérida, W.; Eikerling, M., Vaporization-exchange model for dynamic water sorption in Nafion: Transient solution. *Electrochemistry Communications* **2011,** *13* (1), 5-7.

97. Sone, Y.; Ekdunge, P.; Simonsson, D., Proton conductivity of Nafion 117 as measured by a four ‐ electrode AC impedance method. *Journal of the Electrochemical Society* **1996,** *143* (4), 1254.

98. Zheng, Y.; Ash, U.; Pandey, R. P.; Ozioko, A. G.; Ponce-González, J.; Handl, M.; Weissbach, T.; Varcoe, J. R.; Holdcroft, S.; Liberatore, M. W.; Hiesgen, R.; Dekel, D. R., Water Uptake Study of Anion Exchange Membranes. *Macromolecules* **2018,** *51* (9), 3264-3278.

99. Zawodzinski, T. A.; Derouin, C.; Radzinski, S.; Sherman, R. J.; Smith, V. T.; Springer, T. E.; Gottesfeld, S., Water Uptake by and Transport Through Nafion® 117 Membranes. *Journal of The Electrochemical Society* **1993,** *140* (4), 1041-1047.

100. Daly, K. B.; Benziger, J. B.; Debenedetti, P. G.; Panagiotopoulos, A. Z., Molecular dynamics simulations of water sorption in a perfluorosulfonic acid membrane. *J Phys Chem B* **2013,** *117* (41), 12649-60.

101. Di Vona, M. L.; Licoccia, S.; Knauth, P., Organic–inorganic hybrid membranes based on sulfonated polyaryl–ether–ketones: Correlation between water uptake and electrical conductivity. *Solid State Ionics* **2008,** *179* (21-26), 1161-1165.

102. Yeager, H. L.; Steck, A., Cation and Water Diffusion in Nafion Ion Exchange Membranes: Influence of Polymer Structure. *Journal of The Electrochemical Society* **1981,** *128* (9), 1880-1884.

103. Akhtar, F. H.; Abdulhamid, M. A.; Vovusha, H.; Ng, K. C.; Schwingenschlögl, U.; Szekely, G., Defining sulfonation limits of poly(ether-ether-ketone) for energy-efficient dehumidification. *Journal of Materials Chemistry A* **2021,** *9* (33), 17740-17748.

104. Pinto, B. P.; de Santa Maria, L. C.; Sena, M. E., Sulfonated poly(ether imide): A versatile route to prepare functionalized polymers by homogenous sulfonation. *Materials Letters* **2007,** *61* (11), 2540-2543.

105. Guo, Q.; N. Pintauro, P.; Tang, H.; O'Connor, S., Sulfonated and crosslinked polyphosphazene-based proton-exchange membranes. *Journal of Membrane Science* **1999,** *154* (2), 175-181.

106. Kim, Y. S.; Pivovar, B. S., Moving beyond mass-based parameters for conductivity analysis of sulfonated polymers. *Annual review of chemical and biomolecular engineering* **2010,** *1*, 123-148.

107. Elabd, Y. A.; Hickner, M. A., Block Copolymers for Fuel Cells. *Macromolecules* **2011,** *44* (1), 1-11.

108. Sun, R.; Elabd, Y. A., Synthesis and High Alkaline Chemical Stability of Polyionic Liquids with Methylpyrrolidinium, Methylpiperidinium, Methylazepanium, Methylazocanium, and Methylazonanium Cations. *ACS Macro Letters* **2019**, 540-545.

109. Wu, X.; Wang, X.; He, G.; Benziger, J., Differences in water sorption and proton conductivity between Nafion and SPEEK. *Journal of Polymer Science Part B: Polymer Physics* **2011,** *49* (20), 1437-1445.

110. Fan, J.; Zhou, W.; Wang, Q.; Chu, Z.; Yang, L.; Yang, L.; Sun, J.; Zhao, L.; Xu, J.; Liang, Y.; Chen, Z., Structure dependence of water vapor permeation in polymer nanocomposite membranes investigated by positron annihilation lifetime spectroscopy. *Journal of Membrane Science* **2018,** *549*, 581-587.

111. Ge, S.; Li, X.; Yi, B.; Hsing, I.-M., Absorption, desorption, and transport of water in polymer electrolyte membranes for fuel cells. *Journal of the Electrochemical Society* **2005,** *152* (6), A1149.

112. Lamy, C.; Millet, P., A critical review on the definitions used to calculate the energy efficiency coefficients of water electrolysis cells working under near ambient temperature conditions. *Journal of Power Sources* **2020,** *447*, 227350.

113. Millet, P.; Mbemba, N.; Grigoriev, S.; Fateev, V.; Aukauloo, A.; Etiévant, C., Electrochemical performances of PEM water electrolysis cells and perspectives. *International Journal of Hydrogen Energy* **2011,** *36* (6), 4134-4142.

114. Snyder, J. D.; Elabd, Y. A., Nafion® nanofibers and their effect on polymer electrolyte membrane fuel cell performance. *Journal of Power Sources* **2009,** *186* (2), 385-392.

115. Tamura, T.; Kawakami, H., Aligned electrospun nanofiber composite membranes for fuel cell electrolytes. *Nano letters* **2010,** *10* (4), 1324-1328.

116. Pan, C.; Wu, H.; Wang, C.; Wang, B.; Zhang, L.; Cheng, Z.; Hu, P.; Pan, W.; Zhou, Z.; Yang, X., Nanowire‐Based High‐Performance “Micro Fuel Cells”: One Nanowire, One Fuel Cell. *Advanced Materials* **2008,** *20* (9), 1644-1648.

117. Choi, J.; Lee, K. M.; Wycisk, R.; Pintauro, P. N.; Mather, P. T., Nanofiber network ion-exchange membranes. *Macromolecules* **2008,** *41* (13), 4569-4572.

118. Chen, H.; Snyder, J. D.; Elabd, Y. A., Electrospinning and solution properties of Nafion and poly (acrylic acid). *Macromolecules* **2008,** *41* (1), 128-135.

119. Xue, J.; Wu, T.; Dai, Y.; Xia, Y., Electrospinning and Electrospun Nanofibers: Methods, Materials, and Applications. *Chemical Reviews* **2019,** *119* (8), 5298-5415.

120. Dong, B.; Gwee, L.; Salas-de La Cruz, D.; Winey, K. I.; Elabd, Y. A., Super proton conductive high-purity Nafion nanofibers. *Nano letters* **2010,** *10* (9), 3785-3790.

121. Angammana, C. J.; Jayaram, S. H., Analysis of the Effects of Solution Conductivity on Electrospinning Process and Fiber Morphology. *IEEE Transactions on Industry Applications* **2011,** *47* (3), 1109-1117.

122. Pattamaprom, C.; Hongrojjanawiwat, W.; Koombhongse, P.; Supaphol, P.; Jarusuwannapoo, T.; Rangkupan, R., The influence of solvent properties and functionality on the electrospinnability of polystyrene nanofibers. *Macromolecular Materials and Engineering* **2006,** *291* (7), 840-847.

123. Reneker, D. H.; Yarin, A. L., Electrospinning jets and polymer nanofibers. *Polymer* **2008,** *49* (10), 2387-2425.

124. Reneker, D. H.; Yarin, A. L.; Zussman, E.; Xu, H., Electrospinning of Nanofibers from Polymer Solutions and Melts. In *Advances in Applied Mechanics*, Aref, H.; van der Giessen, E., Eds. Elsevier: 2007; Vol. 41, pp 43-346.

125. Fong, H.; Chun, I.; Reneker, D. H., Beaded nanofibers formed during electrospinning. *Polymer* **1999,** *40* (16), 4585-4592.

126. Boas, M.; Gradys, A.; Vasilyev, G.; Burman, M.; Zussman, E., Electrospinning polyelectrolyte complexes: pH-responsive fibers. *Soft Matter* **2015,** *11* (9), 1739-1747.

127. Josef, E.; Guterman, R., Designing Solutions for Electrospinning of Poly(ionic liquid)s. *Macromolecules* **2019,** *52* (14), 5223-5230.

128. Tarokh, A.; Karan, K.; Ponnurangam, S., Atomistic MD Study of Nafion Dispersions: Role of Solvent and Counterion in the Aggregate Structure, Ionic Clustering, and Acid Dissociation. *Macromolecules* **2020,** *53* (1), 288-301.

129. Zhao, J.; Xu, A.; Yuan, W. Z.; Gao, J.; Tang, J.; Wang, L.; Ai, F.; Zhang, Y., Evaluation of electrospun nanofiber formation of perfluorosulfonic acid and poly (N-vinylpyrrolidone) through solution rheology. *Journal of Materials Science* **2011,** *46* (23), 7501-7510.

130. Chen, H.; Elabd, Y. A., Polymerized Ionic Liquids: Solution Properties and Electrospinning. *Macromolecules* **2009,** *42* (9), 3368-3373.

131. McKee, M. G.; Hunley, M. T.; Layman, J. M.; Long, T. E., Solution rheological behavior and electrospinning of cationic polyelectrolytes. *Macromolecules* **2006,** *39* (2), 575-583.

132. Mineart, K. P.; Ryan, J. J.; Appavou, M. S.; Lee, B.; Gradzielski, M.; Spontak, R. J., Self-Assembly of a Midblock-Sulfonated Pentablock Copolymer in Mixed Organic Solvents: A Combined SAXS and SANS Analysis. *Langmuir* **2019,** *35* (4), 1032-1039.

133. Choi, J.-H.; Willis, C. L.; Winey, K. I., Structure–property relationship in sulfonated pentablock copolymers. *Journal of Membrane Science* **2012,** *394-395*, 169-174.

134. Choi, J.-H.; Kota, A.; Winey, K. I., Micellar morphology in sulfonated pentablock copolymer solutions. *Industrial & engineering chemistry research* **2010,** *49* (23), 12093-12097.

135. Truong, P. V.; Black, R. L.; Coote, J. P.; Lee, B.; Ardebili, H.; Stein, G. E., Systematic Approaches To Tailor the Morphologies and Transport Properties of Solution-Cast Sulfonated Pentablock Copolymers. *ACS Applied Polymer Materials* **2018,** *1* (1), 8-17.

136. Mineart, K. P.; Lee, B.; Spontak, R. J., A Solvent-Vapor Approach toward the Control of Block Ionomer Morphologies. *Macromolecules* **2016,** *49* (8), 3126-3137.

137. Griffin, P. J.; Salmon, G. B.; Ford, J.; Winey, K. I., Predicting the solution morphology of a sulfonated pentablock copolymer in binary solvent mixtures. *Journal of Polymer Science Part B: Polymer Physics* **2016,** *54* (2), 254-262.

138. Mineart, K. P.; Jiang, X.; Jinnai, H.; Takahara, A.; Spontak, R. J., Morphological investigation of midblock-sulfonated block ionomers prepared from solvents differing in polarity. *Macromol Rapid Commun* **2015,** *36* (5), 432-8.

139. Tamura, T.; Kawakami, H., Aligned electrospun nanofiber composite membranes for fuel cell electrolytes. *Nano Lett* **2010,** *10* (4), 1324-8.

140. Theron, S.; Zussman, E.; Yarin, A., Experimental investigation of the governing parameters in the electrospinning of polymer solutions. *Polymer* **2004,** *45* (6), 2017-2030.

141. Smallwood, I. M., Handbook of organic solvent properties. *International Journal of Adhesion and Adhesives* **1997,** *2* (17), 177.

142. Hansen, C. M., *Hansen solubility parameters: a user's handbook*. CRC press: 2007.

143. Antoniou, E.; Themistou, E.; Sarkar, B.; Tsianou, M.; Alexandridis, P., Structure and dynamics of dextran in binary mixtures of a good and a bad solvent. *Colloid and Polymer Science* **2010,** *288* (12-13), 1301-1312.

144. Nie, H.; He, A.; Zheng, J.; Xu, S.; Li, J.; Han, C. C., Effects of chain conformation and entanglement on the electrospinning of pure alginate. *Biomacromolecules* **2008,** *9* (5), 1362-1365.

145. Mecerreyes, D., Polymeric ionic liquids: Broadening the properties and applications of polyelectrolytes. *Progress in Polymer Science* **2011,** *36* (12), 1629-1648.

146. Yuan, J.; Mecerreyes, D.; Antonietti, M., Poly(ionic liquid)s: An update. *Progress in Polymer Science* **2013,** *38* (7), 1009-1036.

147. Choi, U. H.; Mittal, A.; Price, T. L.; Gibson, H. W.; Runt, J.; Colby, R. H., Polymerized Ionic Liquids with Enhanced Static Dielectric Constants. *Macromolecules* **2013,** *46* (3), 1175-1186.

148. Yang, X.; Jiang, M.; Gao, X.; Bao, D.; Sun, Q.; Holmes, N.; Duan, H.; Mukherjee, S.; Adair, K.; Zhao, C., Determining the limiting factor of the electrochemical stability window for PEO-based solid polymer electrolytes: main chain or terminal–OH group? *Energy & Environmental Science* **2020,** *13* (5), 1318-1325.

149. Mindemark, J.; Lacey, M. J.; Bowden, T.; Brandell, D., Beyond PEO—Alternative host materials for Li + -conducting solid polymer electrolytes. *Progress in Polymer Science* **2018,** *81*, 114-143.

150. Chen, T.-L.; Lathrop, P. M.; Sun, R.; Elabd, Y. A., Lithium-Ion Transport in Poly(ionic liquid) Diblock Copolymer Electrolytes: Impact of Salt Concentration and Cation and Anion Chemistry. *Macromolecules* **2021**.

151. Wang, X.; Chen, F.; Girard, G. M.; Zhu, H.; MacFarlane, D. R.; Mecerreyes, D.; Armand, M.; Howlett, P. C.; Forsyth, M., Poly (ionic liquid) s-in-salt electrolytes with co-coordination-assisted lithium-ion transport for safe batteries. *Joule* **2019,** *3* (11), 2687-2702.

152. Mendes, T. C.; Goujon, N.; Malic, N.; Postma, A.; Chiefari, J.; Zhu, H.; Howlett, P. C.; Forsyth, M., Polymerized Ionic Liquid Block Copolymer Electrolytes for

All-Solid-State Lithium-Metal Batteries. *Journal of The Electrochemical Society* **2020,** *167* (7), 070525.

153. Chen, T.-L.; Sun, R.; Willis, C.; Krutzer, B.; Morgan, B. F.; Beyer, F. L.; Han, K. S.; Murugesan, V.; Elabd, Y. A., Impact of ionic liquid on lithium ion battery with a solid poly(ionic liquid) pentablock terpolymer as electrolyte and separator. *Polymer* **2020,** *209*, 122975.

154. Chen, T.-L.; Sun, R.; Willis, C.; Morgan, B. F.; Beyer, F. L.; Elabd, Y. A., Lithium ion conducting polymerized ionic liquid pentablock terpolymers as solid-state electrolytes. *Polymer* **2019,** *161*, 128-138.

155. Mogurampelly, S.; Ganesan, V., Ion Transport in Polymerized Ionic Liquid–Ionic Liquid Blends. *Macromolecules* **2018,** *51* (23), 9471-9483.

156. Delhorbe, V.; Bresser, D.; Mendil-Jakani, H.; Rannou, P.; Bernard, L.; Gutel, T.; Lyonnard, S.; Picard, L., Unveiling the Ion Conduction Mechanism in Imidazolium-Based Poly(ionic liquids): A Comprehensive Investigation of the Structure-to-Transport Interplay. *Macromolecules* **2017,** *50* (11), 4309-4321.

157. Li, M.; Yang, L.; Fang, S.; Dong, S., Novel polymeric ionic liquid membranes as solid polymer electrolytes with high ionic conductivity at moderate temperature. *Journal of Membrane Science* **2011,** *366* (1-2), 245-250.

158. Wang, A.; Xu, H.; Liu, X.; Gao, R.; Wang, S.; Zhou, Q.; Chen, J.; Liu, X.; Zhang, L., The synthesis of a hyperbranched star polymeric ionic liquid and its application in a polymer electrolyte. *Polymer Chemistry* **2017,** *8* (20), 3177-3185.

159. Wang, A.; Liu, X.; Wang, S.; Chen, J.; Xu, H.; Xing, Q.; Zhang, L., Polymeric ionic liquid enhanced all-solid-state electrolyte membrane for high-performance lithium-ion batteries. *Electrochimica Acta* **2018,** *276*, 184-193.

160. Shin, J. J.; Kim, E. J.; Ku, K. H.; Lee, Y. J.; Hawker, C. J.; Kim, B. J., 100th Anniversary of Macromolecular Science Viewpoint: Block Copolymer Particles: Tuning Shape, Interfaces, and Morphology. *ACS Macro Letters* **2020,** *9* (3), 306-317.

161. Einert, M.; Wessel, C.; Badaczewski, F.; Leichtweiß, T.; Eufinger, C.; Janek, J.; Yuan, J.; Antonietti, M.; Smarsly, B. M., Nitrogen-Doped Carbon Electrodes: Influence of Microstructure and Nitrogen Configuration on the Electrical Conductivity of Carbonized Polyacrylonitrile and Poly(ionic liquid) Blends. *Macromolecular Chemistry and Physics* **2015,** *216* (19), 1930-1944.

162. Yuan, J.; Márquez, A. G.; Reinacher, J.; Giordano, C.; Janek, J.; Antonietti, M., Nitrogen-doped carbon fibers and membranes by carbonization of electrospun poly(ionic liquid)s. *Polymer Chemistry* **2011,** *2* (8).

163. Li, H.; Ha, T. A.; Jiang, S.; Pozo-Gonzalo, C.; Wang, X.; Fang, J.; Howlett, P. C.; Wang, X., N, F and S doped carbon nanofibers generated from electrospun polymerized ionic liquids for metal-free bifunctional oxygen electrocatalysis. *Electrochimica Acta* **2021,** *377*, 138089.

164. Wang, Z.; Si, Y.; Zhao, C.; Yu, D.; Wang, W.; Sun, G., Flexible and Washable Poly(Ionic Liquid) Nanofibrous Membrane with Moisture Proof Pressure Sensing for Real-Life Wearable Electronics. *ACS Appl Mater Interfaces* **2019,** *11* (30), 27200-27209.

165. Zhu, M.; Cao, Q.; Liu, B.; Guo, H.; Wang, X.; Han, Y.; Sun, G.; Li, Y.; Zhou, J., A novel cellulose acetate/poly (ionic liquid) composite air filter. *Cellulose* **2020,** *27* (7), 3889-3902.

166. Yang, H.; Jiang, S.; Fang, H.; Hu, X.; Duan, G.; Hou, H., Molecular orientation in aligned electrospun polyimide nanofibers by polarized FT-IR spectroscopy. *Spectrochim Acta A Mol Biomol Spectrosc* **2018,** *200*, 339-344.

167. Kotresh, T. M.; Ramani, R.; Jana, N.; Minu, S.; Shekar, R. I.; Ramachandran, R., Supermolecular Structure, Free Volume, and Glass Transition of Needleless Electrospun Polymer Nanofibers. *ACS Applied Polymer Materials* **2021,** *3* (8), 3989-4007.

168. Wang, W.; Barber, A. H., Measurement of size - dependent glass transition temperature in electrospun polymer fibers using AFM nanomechanical testing. *Journal of Polymer Science Part B: Polymer Physics* **2012,** *50* (8), 546-551.

169. Wong, S.-C.; Baji, A.; Leng, S., Effect of fiber diameter on tensile properties of electrospun poly(ε-caprolactone). *Polymer* **2008,** *49* (21), 4713-4722.

170. Richard-Lacroix, M.; Pellerin, C., Molecular Orientation in Electrospun Fibers: From Mats to Single Fibers. *Macromolecules* **2013,** *46* (24), 9473-9493.

171. Zhou, Y.-c.; Bao, R.-Y.; Liu, Z.; Yang, M.-B.; Yang, W., Electrospun Modified Polyketone-Based Anion Exchange Membranes with High Ionic Conductivity and Robust Mechanical Properties. *ACS Applied Energy Materials* **2021,** *4* (5), 5187-5200.

172. Zhang, Y.; Rutledge, G. C., Electrical Conductivity of Electrospun Polyaniline and Polyaniline-Blend Fibers and Mats. *Macromolecules* **2012,** *45* (10), 4238-4246.

173. Banitaba, S. N.; Semnani, D.; Karimi, M.; Heydari-Soureshjani, E.; Rezaei, B.; Ensafi, A. A., A comparative analysis on the morphology and electrochemical performances of solution-casted and electrospun PEO-based electrolytes: The effect of fiber diameter and surface density. *Electrochimica Acta* **2021,** *368*.

174. Banitaba, S. N.; Semnani, D.; Fakhrali, A.; Ebadi, S. V.; Heydari-Soureshjani, E.; Rezaei, B.; Ensafi, A. A., Electrospun PEO nanofibrous membrane enable by LiCl,

LiClO4, and LiTFSI salts: a versatile solvent-free electrolyte for lithium-ion battery application. *Ionics* **2020,** *26* (7), 3249-3260.

175. Banitaba, S. N.; Semnani, D.; Heydari-Soureshjani, E.; Rezaei, B.; Ensafi, A. A., The effect of concentration and ratio of ethylene carbonate and propylene carbonate plasticizers on characteristics of the electrospun PEO-based electrolytes applicable in lithium-ion batteries. *Solid State Ionics* **2020,** *347*.

176. Banitaba, S. N.; Semnani, D.; Rezaei, B.; Ensafi, A. A., Morphology and electrochemical and mechanical properties of polyethylene ‐ oxide ‐ based nanofibrous electrolytes applicable in lithium ion batteries. *Polymer International* **2019,** *68* (4), 746-754.

177. la Cruz, D. S.-d.; Green, M. D.; Ye, Y.; Elabd, Y. A.; Long, T. E.; Winey, K. I., Correlating backbone-to-backbone distance to ionic conductivity in amorphous polymerized ionic liquids. *Journal of Polymer Science Part B: Polymer Physics* **2012,** *50* (5), 338-346.

178. Allen, M. H.; Wang, S.; Hemp, S. T.; Chen, Y.; Madsen, L. A.; Winey, K. I.; Long, T. E., Hydroxyalkyl-Containing Imidazolium Homopolymers: Correlation of Structure with Conductivity. *Macromolecules* **2013,** *46* (8), 3037-3045.

179. Sun, R.; Meek, K. M.; Ho, H. C.; Elabd, Y. A., Nitrogen ‐ doped carbons derived from poly(ionic liquid)s with various backbones and cations. *Polymer International* **2019,** *68* (9), 1599-1609.

180. Sun, R.; Elabd, Y. A., Synthesis and High Alkaline Chemical Stability of Polyionic Liquids with Methylpyrrolidinium, Methylpiperidinium, Methylazepanium, Methylazocanium, and Methylazonanium Cations. *ACS Macro Letters* **2019,** *8* (5), 540-545.

181. Meek, K. M.; Nykaza, J. R.; Elabd, Y. A., Alkaline Chemical Stability and Ion Transport in Polymerized Ionic Liquids with Various Backbones and Cations. *Macromolecules* **2016,** *49* (9), 3382-3394.

182. Nhung, L. T. T.; Kim, I. Y.; Yoon, Y. S., Quaternized Chitosan-Based Anion Exchange Membrane Composited with Quaternized Poly(vinylbenzyl chloride)/Polysulfone Blend. *Polymers (Basel)* **2020,** *12* (11).

183. Holomb, R.; Martinelli, A.; Albinsson, I.; Lassègues, J. C.; Johansson, P.; Jacobsson, P., Ionic liquid structure: the conformational isomerism in 1-butyl-3-methyl-imidazolium tetrafluoroborate ([bmim][BF4
]). *Journal of Raman Spectroscopy* **2008,** *39* (7), 793-805.

184. Ye, Y.; Elabd, Y. A., Anion exchanged polymerized ionic liquids: High free volume single ion conductors. *Polymer* **2011,** *52* (5), 1309-1317.

185. Janakiraman, S.; Surendran, A.; Ghosh, S.; Anandhan, S.; Venimadhav, A., A new strategy of PVDF based Li-salt polymer electrolyte through electrospinning for lithium battery application. *Materials Research Express* **2018,** *6* (3), 035303.

186. Topuz, F.; Abdulhamid, M. A.; Holtzl, T.; Szekely, G., Nanofiber engineering of microporous polyimides through electrospinning: Influence of electrospinning parameters and salt addition. *Materials & Design* **2021,** *198*, 109280.

187. Yalcinkaya, F.; Yalcinkaya, B.; Jirsak, O., Influence of salts on electrospinning of aqueous and nonaqueous polymer solutions. *Journal of Nanomaterials* **2015,** *2015*.

188. Li, R.; Tomasula, P.; De Sousa, A. M. M.; Liu, S.-C.; Tunick, M.; Liu, K.; Liu, L., Electrospinning Pullulan Fibers from Salt Solutions. *Polymers* **2017,** *9* (1), 32.

189. Zhang, H.; Wu, Z.; Francis, L. F., Formation of salt crystal whiskers on porous nanoparticle coatings. *Langmuir* **2010,** *26* (4), 2847-56.

190. Gouverneur, M.; Jeremias, S.; Schönhoff, M., 7Li nuclear magnetic resonance studies of dynamics in a ternary gel polymer electrolyte based on polymeric ionic liquids. *Electrochimica Acta* **2015,** *175*, 35-41.

191. Wang, X.; Chen, F.; Girard, G. M. A.; Zhu, H.; MacFarlane, D. R.; Mecerreyes, D.; Armand, M.; Howlett, P. C.; Forsyth, M., Poly(Ionic Liquid)s-in-Salt Electrolytes with Co-coordination-Assisted Lithium-Ion Transport for Safe Batteries. *Joule* **2019,** *3* (11), 2687-2702.

192. Isik, M.; Gracia, R.; Kollnus, L. C.; Tomé, L. C.; Marrucho, I. M.; Mecerreyes, D., Cholinium-Based Poly(ionic liquid)s: Synthesis, Characterization, and Application as Biocompatible Ion Gels and Cellulose Coatings. *ACS Macro Letters* **2013,** *2* (11), 975-979.

193. Weber, R. L.; Ye, Y.; Banik, S. M.; Elabd, Y. A.; Hickner, M. A.; Mahanthappa, M. K., Thermal and ion transport properties of hydrophilic and hydrophobic polymerized styrenic imidazolium ionic liquids. *Journal of Polymer Science Part B: Polymer Physics* **2011,** *49* (18), 1287-1296.

194. Macossay, J.; Marruffo, A.; Rincon, R.; Eubanks, T.; Kuang, A., Effect of needle diameter on nanofiber diameter and thermal properties of electrospun poly(methyl methacrylate). *Polymers for Advanced Technologies* **2007,** *18* (3), 180-183.

195. S.R. Dhakate, B. S., M. Uppal, R.B. Mathur, Effect Of Processing Parameters On Morphology And Thermal Properties Of Electrospun Polycarbonate Nanofibers. *Advanced Materials Letters* **2010,** *1* (3), 200-204.

196. Sheng, L.; Jiang, R.; Zhu, Y.; Ji, Y., Electrospun Cellulose Nanocrystals/Polycaprolactone Nanocomposite Fiber Mats. *Journal of Macromolecular Science, Part B* **2014,** *53* (5), 820-828.

197. Mogurampelly, S.; Keith, J. R.; Ganesan, V., Mechanisms underlying ion transport in polymerized ionic liquids. *Journal of the American Chemical Society* **2017,** *139* (28), 9511-9514.

198. Owejan, J. P.; Gagliardo, J. J.; Sergi, J. M.; Kandlikar, S. G.; Trabold, T. A., Water management studies in PEM fuel cells, Part I: Fuel cell design and in situ water distributions. *International Journal of Hydrogen Energy* **2009,** *34* (8), 3436-3444.

199. Molaeimanesh, G. R.; Akbari, M. H., Impact of PTFE distribution on the removal of liquid water from a PEMFC electrode by lattice Boltzmann method. *International Journal of Hydrogen Energy* **2014,** *39* (16), 8401-8409.

200. Zheng, G.; Li, W.; Wang, X.; Wu, D.; Sun, D.; Lin, L., Precision deposition of a nanofibre by near-field electrospinning. *Journal of Physics D: Applied Physics* **2010,** *43* (41), 415501.

201. Wu, Y.; Dong, Z.; Wilson, S.; Clark, R. L., Template-assisted assembly of electrospun fibers. *Polymer* **2010,** *51* (14), 3244-3248.

202. Vaquette, C.; Cooper-White, J. J., Increasing electrospun scaffold pore size with tailored collectors for improved cell penetration. *Acta Biomater* **2011,** *7* (6), 2544-57.

203. Ayers, K. E.; Renner, J. N.; Danilovic, N.; Wang, J. X.; Zhang, Y.; Maric, R.; Yu, H., Pathways to ultra-low platinum group metal catalyst loading in proton exchange membrane electrolyzers. *Catalysis Today* **2016,** *262*, 121-132.

204. Yu, H.; Bonville, L.; Jankovic, J.; Maric, R., Microscopic insights on the degradation of a PEM water electrolyzer with ultra-low catalyst loading. *Applied Catalysis B: Environmental* **2020,** *260*, 118194.

205. Hegge, F.; Lombeck, F.; Cruz Ortiz, E.; Bohn, L.; von Holst, M.; Kroschel, M.; Hübner, J.; Breitwieser, M.; Strasser, P.; Vierrath, S., Efficient and Stable Low Iridium Loaded Anodes for PEM Water Electrolysis Made Possible by Nanofiber Interlayers. *ACS Applied Energy Materials* **2020,** *3* (9), 8276-8284.

206. Wang, Z. M.; Liu, P.; Cao, Y. P.; Ye, F.; Xu, C.; Du, X. Z., Characterization and electrocatalytic properties of electrospun Pt-IrO2 nanofiber catalysts for oxygen evolution reaction. *International Journal of Energy Research* **2021,** *45* (4), 5841-5851.

207. Yuan, Q.; Fu, Z.; Wang, Y.; Chen, W.; Wu, X.; Gong, X.; Zhen, D.; Jian, X.; He, G., Coaxial electrospun sulfonated poly (ether ether ketone) proton exchange membrane for conductivity-strength balance. *Journal of Membrane Science* **2020,** *595*, 117516.

208. Li, M.; Zheng, Y.; Xin, B.; Xu, Y., Coaxial Electrospinning: Jet Motion, Core–Shell Fiber Morphology, and Structure as a Function of Material Parameters. *Industrial & Engineering Chemistry Research* **2020,** *59* (13), 6301-6308.

209. Nykaza, J. R.; Savage, A. M.; Pan, Q.; Wang, S.; Beyer, F. L.; Tang, M. H.; Li, C. Y.; Elabd, Y. A., Polymerized ionic liquid diblock copolymer as solid-state electrolyte and separator in lithium-ion battery. *Polymer* **2016,** *101*, 311-318.

210. Fan, L.; Xu, Y.; Zhou, X.; Chen, F.; Fu, Q., Effect of salt concentration in spinning solution on fiber diameter and mechanical property of electrospun styrene-butadiene-styrene tri-block copolymer membrane. *Polymer* **2018,** *153*, 61-69.

211. Ma, M.; Krikorian, V.; Yu, J. H.; Thomas, E. L.; Rutledge, G. C., Electrospun Polymer Nanofibers with Internal Periodic Structure Obtained by Microphase Separation of Cylindrically Confined Block Copolymers. *Nano Letters* **2006,** *6* (12), 2969-2972.

212. Kalra, V.; Mendez, S.; Lee, J. H.; Nguyen, H.; Marquez, M.; Joo, Y. L., Confined Assembly in Coaxially Electrospun Block Copolymer Fibers. *Advanced Materials* **2006,** *18* (24), 3299-3303.